ORNL/Sub/90-SF521/03

FINAL REPORT

MOISTURE-INDUCED EMBRITTLEMENT OF IRON ALUMINIDES

April 1, 1995

Report Prepared by
A. Castagna and N.S. Stoloff
Rensselaer Polytechnic Institute
Materials Engineering Department
Troy, NY 12180-3590
under
Subcontract No. 19X-SF521C

for

OAK RIDGE NATIONAL LABORATORY
Oak Ridge, Tennessee 37831
managed by
MARTIN MARIETTA ENERGY SYSTEMS, INC.
for the
U.S. Department of Energy
under Contract No. DE-AC05-840R21400

DISCLAIMER

ABSTRACT

Iron-aluminum alloys of 24 at.%Al and higher have been shown to be susceptible to hydrogen embrittlement by exposure to both gaseous hydrogen and water vapor. This study examines the effect of hydrogen embrittlement by gaseous hydrogen and moisture-bearing air on the tensile properties and fatigue crack growth resistance of two ordered Fe-Al intermetallic alloys (28 and 36at.% aluminum) and one disordered Fe-Al alloy (16 at.% Al). The susceptibility to embrittlement is found to vary with both aluminum content and ordered state.

The tensile ductility of the disordered low aluminum alloy is found to be not affected by moisture-bearing air, and the fatigue crack growth resistance is affected only slightly by moisture. However, the higher aluminum alloys are severely embrittled by moisture-bearing air. The oxidation of aluminum with the concurrent release of hydrogen has been shown previously to be responsible for embrittlement of Fe_3Al alloys. It is likely that the smaller amount of aluminum available for the oxidation reaction in the 16at.% alloy precludes such embrittling reactions. In contrast, gaseous hydrogen is found to be embrittling to all alloys studied in both cyclic and monotonic tests. Fractography is used to show that hydrogen preferentially attacks cleavage planes in these alloys.

The inherent fatigue crack growth resistance, as measured in an inert environment, of the low aluminum disordered alloy is found to be much lower than that for the high aluminum ordered alloys.

Fatigue crack growth rate in an embrittling environment can be expressed as a superposition of a purely mechanical fatigue component and a corrosion-fatigue component. Fatigue crack growth tests in inert and embrittling environments are used to isolate the corrosion-fatigue component of the crack growth rate in an Fe-28at.%Al alloy.

By varying the frequency it is shown that the corrosion-fatigue component displays a frequency dependence. At lower frequencies more time is available for penetration of hydrogen ahead of the crack tip. Hydrogen transport in the iron-aluminum alloys is found to occur primarily by a dislocation-assisted transport mechanism, which allows for penetration depths of 10-100 times the distance that can be achieved by bulk diffusion. An expression is developed for the corrosion-fatigue component of crack growth rate which incorporates both the stress intensity range and the frequency dependence.

"Research sponsored by the U.S. Department of Energy, Fossil Energy Advanced Research and Technology Development Materials Program, DOE/FE AA 15 10 10 0, Work Breakdown Structure Element RPI-2"

1 INTRODUCTION

Iron aluminides, both ordered intermetallics and disordered alloys, are currently being studied for use in applications where low cost, relatively low weight, moderate strength at temperatures up to 500°C, and excellent corrosion resistance are desired. Binary iron aluminides do not possess high ductility at room temperature in air, typically 4-8%. Like many other intermetallics and steels, iron aluminides have been shown to be embrittled by gaseous hydrogen and water vapor, which lowers the room temperature ductility (1, 2, 3). The predominant embrittling mechanism in Fe_3Al involves a chemical reaction with water vapor in the air and aluminum at the surface of the material. This reaction releases monatomic hydrogen at the surface of the material and is shown in this work to be a potent mechanism of embrittlement.

However, iron aluminides have demonstrated ductility of 12% - 16% when tested in vacuum or gaseous oxygen environments. This indicates that Fe_3Al is an inherently ductile material and an environmental interaction causes the low ductility in air. Fe_3Al has been shown to deform by [110] <111> slip which provides for at least 5 slip systems and exhibits only moderate yield and tensile strength, which are properties associated with inherently ductile materials. With the ductile nature of iron aluminides in mind, the mechanisms of embrittlement in iron aluminides are currently being investigated, as well as methods of preventing embrittlement such as alloying or coating.

The purpose of this research is to examine the effects of environmental embrittlement on the mechanical properties of an Fe_3Al base intermetallic compound and a disordered iron aluminum alloy. In particular, fatigue crack growth resistance and tensile behavior will be examined in various environments, and the resulting data will be used to gain insight on the role of hydrogen in embrittlement of the iron-aluminum alloys.

2 BACKGROUND

The objective of this research is to study hydrogen embrittlement in intermetallic Fe_3Al alloys. This section will focus on aspects of environmental embrittlement and hydrogen embrittlement, characteristics of ordered intermetallic compounds in general and a review of the properties of iron aluminides and pertinent literature regarding this alloy system.

2.1 Environmental Embrittlement

Embrittlement is loss of ductility or fracture toughness in a material due to either a reaction with the external environment surrounding the material, or a reaction with an internal contaminant which is not an intentional component of the material. Several types of external embrittlement, which are termed environmental embrittlement, are oxidation, sulfidation, liquid-metal embrittlement and hydrogen embrittlement. Internal embrittlement is often due to segregation of impurities such as sulfur, carbon or trapped hydrogen to grain boundaries, or the formation of brittle phases such as Laves or other topologically close packed phases.

Embrittlement can be manifested by a loss of ductility during tensile loading, shortened fatigue life during high cycle or low cycle fatigue, increased crack growth rates during FCG testing, or reduced K_C in fracture toughness testing. Materials in a brittle state also are generally more difficult to work with than more ductile materials. There can be problems in fabricability, poor resistance to overloads, and difficulty in early damage detection. Figs. 2.1a-c show experimental data illustrating the effects of environment on the mechanical properties of several materials. Fig. 2.1a shows the tensile stress-strain curves for ordered and disordered Ni_3Fe, and the loss of ductility and decreased UTS when

hydrogen is cathodically charged into the specimen (4). Fig. 2.1b shows the decrease in high cycle fatigue life in an Al-Zn-Mg alloy when fatigued in humid nitrogen, which acts as a source of hydrogen due to chemical decomposition of water vapor (5). Fig. 2.1c shows the effect of hydrogen gas on the fatigue crack growth resistance of an ordered and disordered FeCo-V alloy (6).

A material must show some degree of ductility or toughness for an embrittlement phenomenon to be observed. A material which is inherently brittle due to an insufficient number of slip planes, weak grain boundaries, or weak cleavage planes may not show evidence of embrittlement even though the requisite mechanical and chemical conditions for embrittlement are present. The same, or very similar, material can be made to show the effects of embrittlement by varying the alloy composition or processing parameters to increase the inherent ductility.

A variety of materials have been observed to be embrittled by hydrogen. Hydrogen embrittlement was first recognized in structural steels, and numerous studies have shown many such steels to be susceptible.

Many intermetallic compounds are susceptible to hydrogen embrittlement, particularly those with crystal structures of high symmetry such as the $L1_2$, B2, and DO_{19}. Embrittled $L1_2$ alloys include Co_3Ti (7, 8, 9), nickel aluminides (10, 11, 12, 13), $Ni_3(Al, Mn)$ (14), $(FeNi)_3V$ (6, 15), and Ni_3Fe (4). The embrittled B2 alloys include Fe_3Al (1, 16) and FeCo-2V (6). Other intermetallics embrittled by hydrogen are DO_3 ordered Fe_3Al (17, 18, 19), and $L1_0$ ordered TiAl (20).

Superalloys such as the Ni-base PWA 1480 (21) and IN718 (22), and the Fe-base IN903 (23) and A286 (22) have been shown to be embrittled by hydrogen. Aluminum alloys are extremely susceptible to hydrogen embrittlement, especially in moisture-bearing environments (5, 24, 25, 26). Pure elements such as nickel (27, 28) can be embrittled as well.

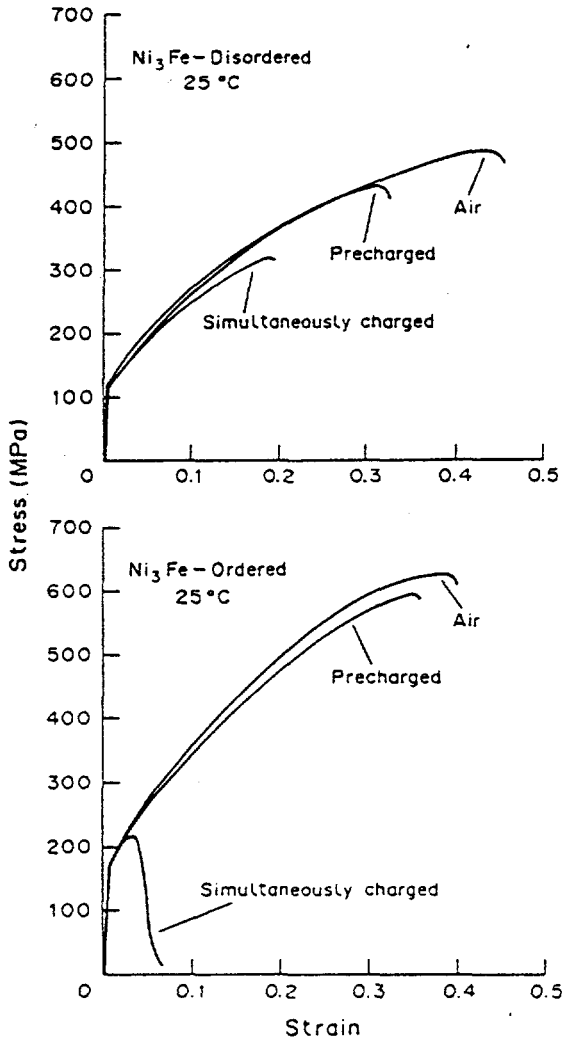

Fig. 2.1 Effect of environment on mechanical properties of various alloys. (a) Effect of hydrogen on the tensile behavior of Ni_3Fe (4).

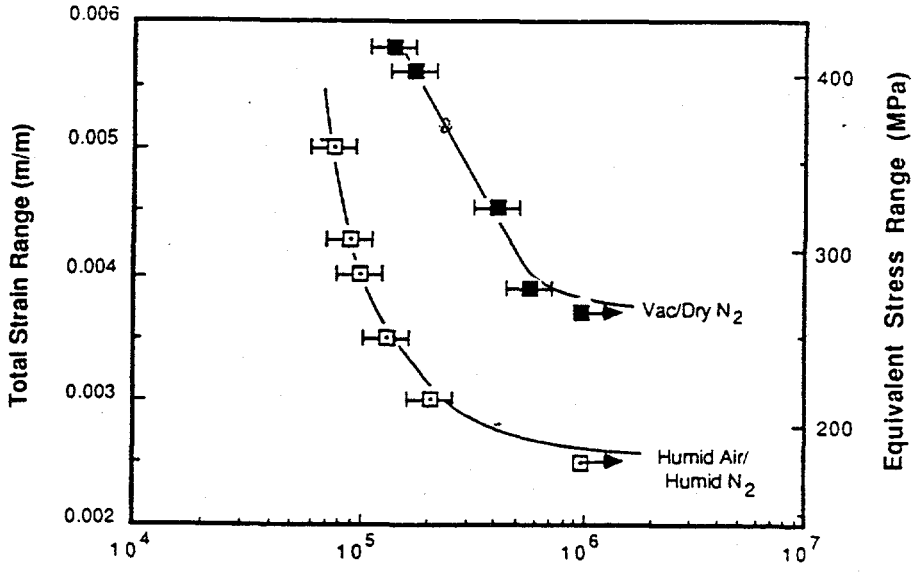

Fig. 2.1 continued (b) Effect of moisture-bearing nitrogen on the high cycle fatigue life of an Al-Mg-Zn alloy (5).

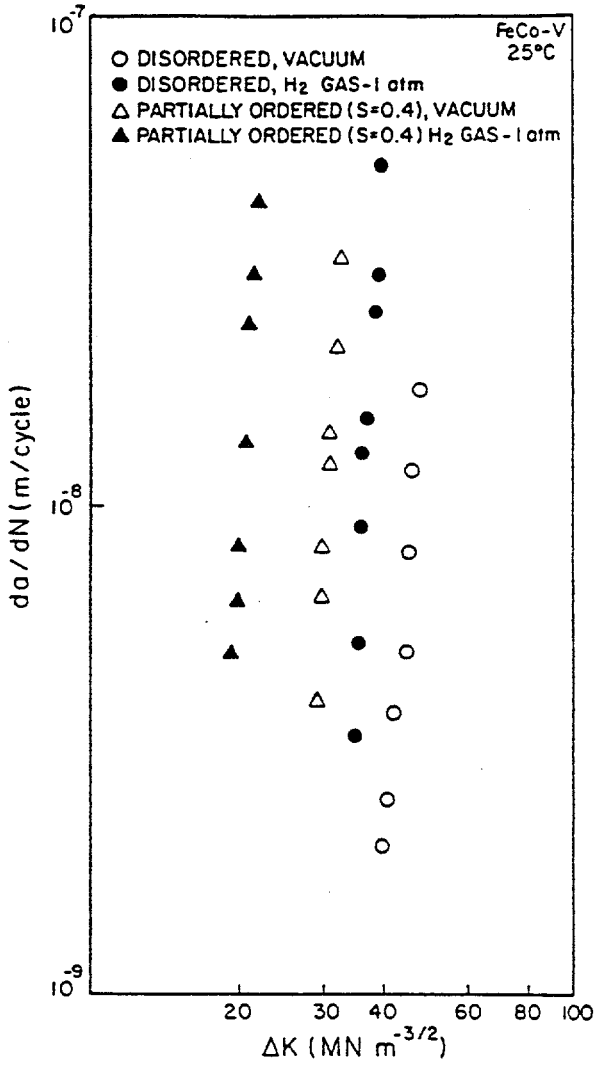

Fig. 2.1 continued (c) Effect of hydrogen on the FCG resistance of FeCo-V (6).

2.1.1 The Embrittlement Process

The process of hydrogen embrittlement can be broken down into a sequence of stages which include:

- transport of the embrittling species to an exposed surface
- surface phenomena (chemical reactions and/or adsorption)
- transport of hydrogen to the embrittled zone
- hydrogen-metal interaction
- fracture at load, stress intensity or deformation levels which are lower than in inert environments

Each of these stages has a rate associated with it which may be dependent on various parameters such as temperature, concentration, alloy composition, and degree of plastic work. The particular alloy, environment and loading situation will determine the rate at which each of these stages progresses. Each stage will often be dependent on the previous stage. For example, the rate of hydrogen transport to the embrittled zone will depend both on what transport mechanism is active and how much hydrogen is available at the surface to be transported. Sometimes one or more of these can be identified as the rate-limiting factor in the embrittlement process. The rate-limiting factor will dictate the rate and degree of embrittlement because it will constrain all subsequent stages of the embrittlement process.

2.1.1.1 Transport to the Surface

Transport to the surface of the material and the crack tip can occur by diffusion or mixing, and will depend on what the embrittling species is and whether it must be

transported through an aqueous or gaseous media. Diffusion of H^+ ions in H_2O occurs approximately 10-1000 times faster than diffusion of hydrogen molecules or atoms in a gaseous environment. In gaseous environments, transport will depend on the temperature, the partial pressure of the embrittling species and whether any other gaseous species are present. Other gaseous species may compete with the embrittling species for sites at the surface and reduce the effective transport rate. Successful transport can be considered to be impingement of the embrittling species on the exposed surface such that the entire surface, or a critical fraction of that surface, is covered.

As an example of transport to the surface being rate-limiting, Gudladt and Petit (29) calculated the time required to cover the exposed surface of an Al-Zn-Mg alloy with H_2O vapor in both low vacuum and N_2 gas. They found that the rate at which the surface becomes covered with H_2O vapor is decreased by a factor of 10-100 when N_2 is present due to competition between H_2O and N_2 for sites at the materials surface. The Al-Zn-Mg alloy was fatigued in H_2O vapor, moist N_2, and vacuum. In H_2O vapor and moist N_2 the alloy exhibited a low ΔK_{TH} and high Paris slope at low stress intensities compared to those measured in vacuum. However, the da/dN vs. ΔK curve measured in moist N_2 quickly merged with that measured in vacuum. At low crack growth rates in the moist N_2 test, transport of H_2O vapor though the N_2 was rapid enough for embrittlement. At high growth rates, not enough time per cycle was available and transport became rate limiting. The amount of H_2O in the moist N_2 test reaching the surface fell below the critical amount required for embrittlement because of the interference of nitrogen, but this was not the case in the H_2O vapor test where there was no interference.

Another example of transport limited diffusion was reported by Hanna et. al. (30) , found that 4340 martensitic steel suffered accelerated crack propagation in water, and that the failure time at a given stress was dependent on the amount of dissolved oxygen in the water because dissolved oxygen competes with the steel surface for hydrogen ions in the

water. The steel surface acts as a catalyst for the combination of positive hydrogen ions with electrons, which produces hydrogen atoms capable of embrittlement. When oxygen is present, oxygen combines with the hydrogen ions to form H_2O, thus reducing the amount of free hydrogen that can be produced.

A rate limiting transport phenomena often manifests itself in a difference between the chemistry near the surface, especially within the crack of a cracked material, and far from the surface. Embrittlement involving a rate limiting process can also be expected to vary with frequency of cyclic loading. Crack length and specimen geometry are also important, as these influence the distance which the embrittling species must be transported, and the distance which chemical reaction by-products must transported away from the crack tip.

2.1.1.2 Surface Phenomena

Once the embrittling species reaches the surface it must adsorb or absorb into the material, possibly undergo surface diffusion to reach the crack tip, and undergo various chemical reactions.

Surface chemical reactions can be rate limiting if a chemical transformation of the embrittling species is required. In gaseous hydrogen, hydrogen present in the form of molecular H_2 must dissociate to atomic H, before adsorption can take place. At elevated temperatures this dissociation becomes less likely (31) and limits the amount of hydrogen available for transport into the bulk of the material. Even at room temperature, adsorption of hydrogen at the surface is the rate limiting step in fatigue of steel in hydrogen gas (32). In aqueous environments hydrogen ions which have been oxidized to form atomic hydrogen are likely to combine with other hydrogen atoms to form molecular H_2, and thus reduce the degree of embrittlement because hydrogen adsorbs and diffuses in the monatomic form. In this situation the $H + H \rightarrow H_2$ step often is the rate-limiting process, where a fast reaction will inhibit embrittlement. The recombination of hydrogen can be

slowed by the use of a hydrogen recombination poison, such as $NaAsO_2$ (33) . The concentration of atomic hydrogen at the surface is increased, and the degree of embrittlement is also increased.

It has been postulated that aluminum alloys, and alloys which contain significant amounts of aluminum are embrittled due to water vapor in the air reacting with aluminum at the materials surface to produce aluminum oxide and hydrogen according to:

$$2Al + 3H_2O \rightarrow Al_2O_3 + 6H^+ + 6e^- \qquad \text{Eq. 1.}$$

$$6H^+ + 6e^- \rightarrow 6H$$

Hydrogen evolved in this manner is of a high fugacity and can penetrate rapidly into the bulk of the material. This type of reaction has been demonstrated to reduce FCG resistance in Al-Zn-Mg alloys (Gudladt and Petit (29)), as well as reduce the high cycle fatigue life (Ricker and Duquette (5)). Water vapor will rapidly decompose according to Eq. 1 whenever any one of a number of reactive elements is present in sufficient quantity. These elements include Al, V, Si, and Ti. Iron and nickel aluminides are very susceptible to this type of embrittlement by H_2O vapor (1, 34, 35), as is Co_3Ti (7, 8, 9) and $(FeNi)_3V$ (6, 15).

2.1.1.3 Bulk Transport

An important requirement in the transport of hydrogen to the region of hydrogen-metal interaction is plastic work during exposure to hydrogen. There are many reports of steels (36) or other intermetallics (37) which are not embrittled when exposed to hydrogen prior to testing in air, or even elastically strained in hydrogen prior to testing in air, but become embrittled when plastic deformation and hydrogen are applied simultaneously. One widely

accepted theory is that the motion of dislocations caused by plastic deformation enhances hydrogen transport. An atmosphere of hydrogen forms about a dislocation near the surface where the local hydrogen concentration is high. As plastic deformation occurs, the dislocations which move away from the surface drag the hydrogen atmosphere with them. Hydrogen atoms may "ride" dislocation further into the material bulk than would be possible by diffusion. Several studies report finding large increases in H_2 concentration within a steel specimen tested in tension. Hydrogen was found at a depth up to 10 times deeper than diffusion could carry the atoms (38). When the same material was elastically strained in hydrogen, no H_2 concentration increase was noted. Planar slip in ordered Ni_2Cr (39) has been observed to cause dislocation pile-ups at the intersection of slip planes, and it was theorized that dislocations carrying hydrogen pile up at these intersections where they cause a high local concentration of hydrogen. This high concentration is responsible for embrittlement by a decohesion mechanism along the slip plane intersections, creating a step-like pattern in the fracture surface.

The significance of dislocation transport does not exclude the role of diffusion. Ricker and Duquette found that the fatigue life of an Al-Zn-Mg alloy was considerably shortened by either fatiguing in moist nitrogen or pre-exposing the material to moist air for at least 30 days and then fatiguing in dry nitrogen. In this material diffusion appears to be an active mechanism for bulk transport when sufficient time is available. The damage incurred during pre-exposure was reversible, as the hydrogen could be allowed to diffuse out by exposure to vacuum after the pre-exposure to moist air, resulting in restoration of the fatigue lives to the original levels. This highlights the fact that, as is true for stress corrosion cracking, the applied load and embrittling species must be present simultaneously for embrittlement to occur.

An effect of the diffusion rate of hydrogen on embrittlement is observed in several intermetallics which can be stabilized at more than one ordered state. In these alloys the

chemical composition is unchanged, but a shift from a disordered to ordered lattice (or an open to close-packed lattice) decreases the bulk diffusivity of hydrogen and mobility of dislocations. In two particular alloys, $(FeNi)_3V$ (6, 15) and Co_3Ti (7), little embrittlement is observed in the disordered state but extreme embrittlement is observed in the ordered state.

At first glance this observation seems to be inconsistent because more severe embrittlement is observed in the ordered material, where hydrogen transport by diffusion and dislocation motion is decreased. An explanation may lie in the fact that the ordered lattice is prone to regions of relatively high hydrogen concentration. The high concentration regions may be slip planes, grain boundaries, or regions of tri-axial stress. In the disordered state, hydrogen is much more free to relieve high concentration regions by diffusing away through the bulk, or not as likely to build up on particular slip planes because dislocation motion and cross slip onto other planes is easier.

2.1.1.4 Hydrogen-Metal Reactions

Several theories describing the actual hydrogen-metal interaction have been proposed. One of the current theories of interest is the "decohesion" mechanism first introduced by Troiano (40) coupled with the triaxial stress condition (41). Hydrogen is believed to segregate to regions of maximum tri-axial stress, where it lowers the binding (cohesion) energy of atoms on particular lattice planes. In the presence of a crack or notch under tensile stress, the location of maximum triaxial stress occurs at the end of the plastic zone (42). As the stress intensity increases, and notch sharpness decreases, the plastic zone tip moves further from the notch tip.

Cracks initiate in these regions of high hydrogen concentration, propagate beyond this region, and stop until the new plastic zone reforms the high hydrogen concentration region. The result is crack propagation in discontinuous steps. Evidence of this mechanism is seen

in certain high strength steels where a notch is required to produce embrittlement, and the degree of embrittlement is dependent on the notch sharpness.

Another possible hydrogen-metal interaction is given by the pressure theory which states that hydrogen atoms diffusing into the bulk recombine into H_2 molecules at internal voids (43). As the amount of hydrogen in the voids increases the internal pressure builds up, adding to the applied stress. While this theory is consistent with the temperature and strain rate dependencies, it cannot be the sole mechanism unless there is a regular network of voids, which is rarely the case.

Another theory is that hydrogen reduces the surface energy of a material, hence the energy needed to propagate a crack. Dislocations carry hydrogen to the vicinity of a microcrack, where a metal-hydrogen interaction lowers the surface energy. However, the energy required to propagate a crack includes a plastic work term in addition to the surface energy term. Since the plastic work term is 10-20 times larger than the surface energy term, this mechanism can provide only a small contribution to the embrittling process.

A well-documented hydrogen-metal interaction which occurs primarily in titanium alloys such as Ti_3Al is hydride formation (44). The chemical potential of solute hydrogen at tensile stress concentrations, such as at a crack tip, decreases and hydrogen diffuses into these areas. Precipitation of metal hydrides occurs. These hydrides are generally very brittle and have a large ΔVolume of formation, making them incoherent in the metal lattice. This significantly reduces the effective fracture toughness in the region of the crack and the crack advances rapidly in a transgranular cleavage mode. The kinetics of hydride formation are often slow enough that the hydrides cannot form continuously ahead of an advancing crack, and the crack will occasionally extend beyond the region of hydride formation and slow until the hydrides catch up. In high strain rate tensile tests the hydrides do not have time to form.

A material which is hydrogen embrittled may experience more than one type of hydrogen-metal interaction. While observations of the fracture surface of an embrittled material often indicate the type of reaction that occurs, and where in the material (i.e., throughout the bulk, along crystallographic planes, or along grain boundaries), it is not always possible to rule out one type of interactions on the basis of such observations.

For example, polycrystalline materials which undergo embrittlement at grain boundaries are not necessarily impervious to embrittlement in their single crystal form. These materials may be prone to hydrogen embrittlement on particular cleavage planes or localized plasticity throughout the bulk, but this type of embrittlement will be masked in the polycrystalline form by a more severe embrittlement of the grain boundaries. In the case of polycrystalline Co_3Ti and Co_3Ti-Ni alloys, failure in inert environments is always in a dimpled transgranular mode, while in aggressive hydrogen environments it is in an intergranular mode (7, 8, 9). However, Liu et. al.(7), observed severe hydrogen embrittlement in single crystal Co-23Ti-3Ni. A dimpled surface with no predominant cleavage facets was seen when tested in vacuum, while in hydrogen gas no dimpling occurred and pronounced {100} cleavage facets were evident.

2.1.2 Features of Environmental Embrittlement

Hydrogen embrittlement, like stress corrosion cracking, requires the detrimental environment and loading conditions to be applied simultaneously for embrittlement to occur (45). However, hydrogen embrittlement can occur with no embrittling agent present in the environment if the material was exposed previously to such an environment and the material retains the hydrogen in some way. This is the case for cathodic pre-charging as seen in Fig. 1a, in which hydrogen is introduced internally through the pre-charging process and the material is embrittled when tested in what otherwise be a non-embrittling environment.

Hydrogen embrittlement exhibits a very strong temperature dependence in most embrittled alloy systems. The peak in embrittlement often occurs at room temperature, with nearly no embrittlement at 50-100°C above and below room temperature. The peak at room temperature is particularly unfortunate as this is a very common temperature for engineering structures to operate at. Cottrel and King (31) have measured fatigue crack growth (FCG) rates in 4360 steel and found very little variation in growth rates in air between 25°C and 80°C, with a Paris slope between 4.0 and 4.2. When fatigued in hydrogen, the crack growth rate shows the expected increase due to hydrogen embrittlement at 25°C, with a Paris slope of 8.7. However, in hydrogen the Paris slope decreases steadily as temperature increases up to 80°C because the embrittlement effect is diminished with increased temperature. In martensitic steels (36), severe embrittlement due to charged hydrogen was observed near room temperature, and steady drop in embrittlement occurs as temperature was increased to 200°C, at which point the hydrogen charged steel behaved in a manner similar to that of hydrogen-free steel.

Two likely explanations for this strong temperature dependence near room temperature are that at higher temperatures, dissociation of H_2 molecules becomes more unfavorable which decreases the availability of atomic hydrogen, and that dislocations ahead of the crack tip are less likely to trap hydrogen which results in a lower hydrogen concentration in the vicinity of the crack tip (46). In hydride forming materials the hydrides are typically unstable at elevated temperatures, thus prevent embrittlement by hydride formation (44).

The degree of hydrogen embrittlement in a material often increases as strain rate or frequency of cyclic loading decreases. As discussed in the previous sections, one of the transport phenomena, such as diffusion of the embrittling species to the specimen surface or into the bulk, or a surface chemical reaction may be rate limiting. The effect of low strain rate or frequency is to provide more time for the slow step to be completed. The trend of

increasing ductility with increasing strain rate is reverse of that often seen in materials which do not undergo environmental embrittlement.

Numerous studies have documented the strain rate effect on degree of embrittlement. For example, Takasugi and Izumi (9) have observed no change in ductility in a Co-23Ti alloy in vacuum when the strain rate was decreased from $5.6x10^{-2}$/sec to $5.6x10^{-4}$/sec, while in air the ductility decreased by 85% for the same strain rate decrease. In $Ni_3(Al_{0.4}Mn_{0.6})$ Masahashi, Takasugi, and Ozumi (14) found that ductility increases from 4 to 10% for a 1000x increase in strain rate. Similar results are seen in Fe_3Al. Scott (47) found that the ductility of DO_3 ordered Fe_3Al tested in tension in air at 25°C increased from 1% at a strain rate of $3x10^{-8}$ $(sec)^{-1}$ to 8% at a strain rate of $1x10^{-2}$ $(sec)^{-1}$.

Other mechanical properties which may affect embrittlement are yield and ultimate tensile strength (UTS). Yield stress will have an effect on the size of the plastic zone and magnitude of tri-axial stress ahead of a crack or notch. High UTS materials may have faster dislocation velocities during plastic deformation which would increase embrittlement if a dislocation-transport mechanism is active.

The dependence of embrittlement on concentration in gaseous environments is often weak once a sufficient amount of the embrittling species is present. Further increases in concentration may not increase the degree of embrittlement. This threshold concentration of the embrittling species is often linked to the rate of deformation. In cyclic loading it is the frequency of the loading cycle, and in monotonic loading it is the strain rate. During fatigue crack growth, the crack growth rate per cycle, da/dN, will greatly affect the threshold concentration and concentration dependence. As discussed in section 2.1.1, a material with a propagating crack may exhibit environmentally enhanced crack growth at low growth rates, and crack growth independent of the environment at high growth rates because the concentration threshold for embrittlement was increased beyond the concentration present.

2.1.3 Environmentally Assisted Crack Growth

It has been proposed that fatigue crack growth in an embrittling environment can be considered to be the superposition of crack growth in the alloy due to only mechanical fatigue, crack growth due to stress corrosion cracking, and crack growth due to corrosion fatigue phenomena. The superposition is expressed as:

$$da/dN = (da/dN)_{mech} + (da/dN)_{scc} + (da/dN)_{cf}. \qquad \text{Eq. 2.}$$

McEvily and Wei (48) described the superposition as illustrated in Fig. 2.2, where purely mechanical and purely stress corrosion crack growth are shown in Figs. 2.2a and 2.2b, respectively. Note that stress corrosion cracking is not cycle dependent. It occurs as a function of time and is the result of sustained-load cracking at stress intensity levels above the stress corrosion cracking threshold, K_{ISCC}. When a true corrosion fatigue interaction occurs, described by the term $(da/dN)_{cf}$ in Eq.2, there is accelerated crack growth at all stress intensity values (Fig.2.2c). A different type of behavior occurs when mechanical fatigue crack growth is superposed with a stress corrosion cracking response, given by $(da/dN)_{scc}$ of Eq.2. In this case the $(da/dN)_{scc}$ term does not have an effect until K_{ISCC} is reached, at which point the crack growth rate is enhanced above that in an inert environment, as illustrated in Fig. 2.2d. A combination of stress corrosion cracking and corrosion-fatigue results in a ΔK vs. da/dN plot in which crack growth is accelerated at low stress intensity values and then accelerated further when K_{ISCC} is surpassed, as seen in Fig. 2.2e. Stress corrosion cracking and corrosion fatigue need not occur together. Many materials which exhibit corrosion fatigue are not susceptible to stress corrosion cracking, or do not exhibit stress corrosion cracking at the stress intensity levels of interest in fatigue (49, 50).

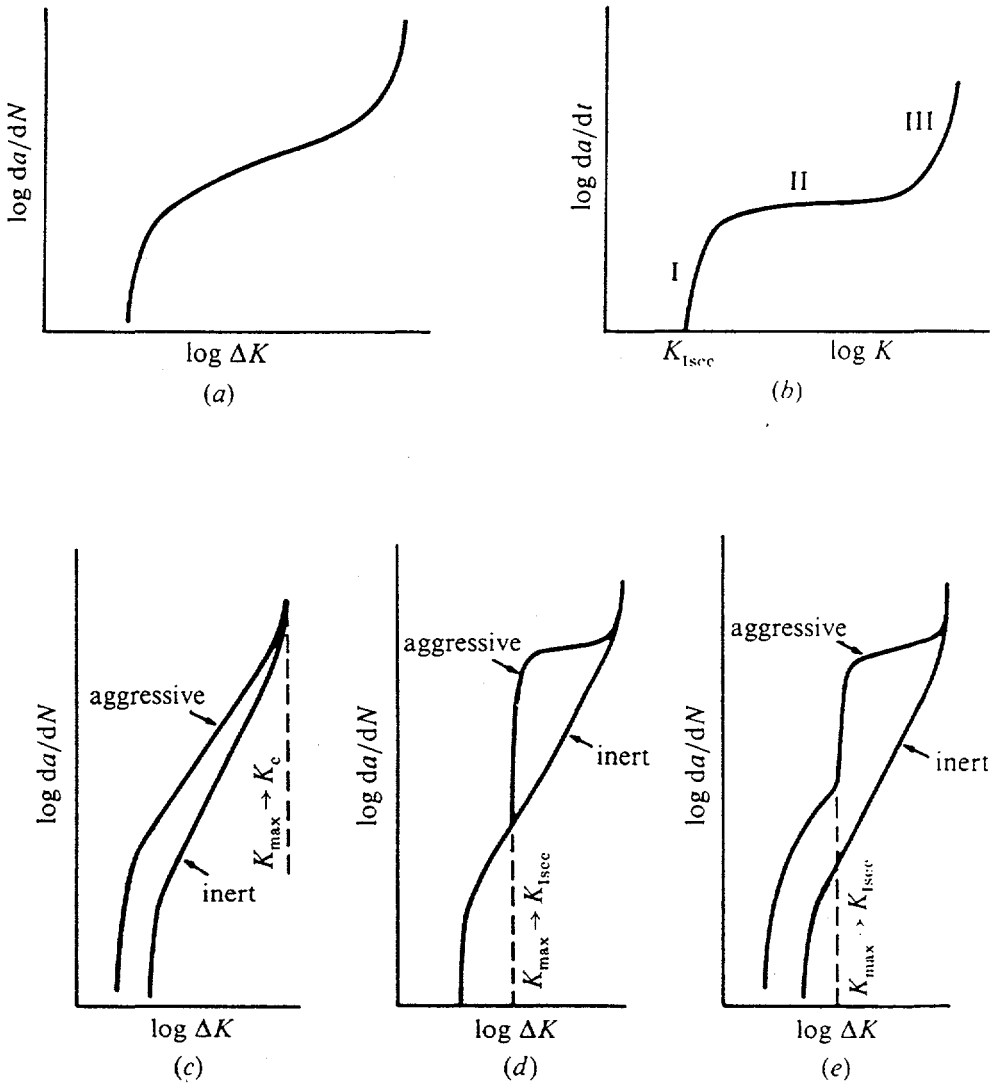

Fig. 2.2 Superposition of mechanical, stress corrosion cracking and corrosion fatigue. a) purely mechanical fatigue; b) purely stress corrosion cracking; c) mechanical fatigue with corrosion fatigue; d) mechanical fatigue with stress corrosion cracking; e) superposition of mechanical fatigue, corrosion fatigue, and stress corrosion cracking. (48)

2.2 Intermetallic Compounds

2.2.1 Interest in Intermetallic Compounds

Intermetallic compounds exhibit a number of properties desirable in structural materials, and have received much attention from researchers attempting to exploit these alloys. The three main desirable characteristics of ordered alloys are good mechanical properties, slow diffusion rates, and matrix compatibility in 2-phase alloys.

Many industries, such as aeronautics and turbine technology, are in need of structural materials capable of operating at high temperatures. Operating temperatures of aircraft turbine materials can exceed 1100°C. The strong tendency for intermetallic alloys to form ordered lattices results in very high melting temperatures for many of these alloys, making them candidate materials where high strength at elevated temperatures is required. Many intermetallic alloys retain their strength at a significant fraction of the melting temperature, in some cases up to T/T_m of 0.7. The anomalous increase in YS with increasing temperature observed in many intermetallics further enhances their potential at high temperatures.

A number of intermetallics, especially the aluminides, have low densities compared to steels and superalloys. When the density compensated strength of intermetallics is considered, they become attractive alternative materials for some applications. The densities of nickel-base superalloys (the Inconel, Udimet, Nimonic, and Hastelloy series) are approximately 8.0 - 8.5g/cc, and the density of cobalt-base superalloys such as Haynes-188 are greater than 9g/cc (51). The densities of various aluminides, in contrast, are 4 g/cc for Ti-Al, 6.5g/cc for Fe_3Al, 5.2g/cc for NiAl, 6.8g/cc for Ni_3Al, and 7.3g/cc for Co_3Ti.

Many of the aluminides exhibit excellent corrosion resistance due to the formation of a protective alumina coating.

2.2.2 The Ordered Lattice

Intermetallic compounds are solid solution metallic compounds which have a strong tendency to exhibit an ordered crystal structure. In an ordered lattice, the main constituent atoms, atoms of type A and type B for the case of a binary, occupy specific sites on the lattice unit cell. When discussing any arbitrary ordered alloy in this thesis, it will be assumed to be a binary alloy and be composed of A and B type atoms.

Ordered compounds exist at or near specific atomic ratios, such as AB, A_2B, A_3B. Some ordered intermetallics exhibit an extensive range of solubility over which order exists, as with iron aluminides.

Most intermetallic alloys have a critical ordering temperature, Tc, below which one type of order exists and above which the alloy transforms to either a disordered state or a different type of order. A few intermetallic systems exhibit atomic order at temperatures up to the melting point. The kinetics of ordering transformations varies considerably between alloy systems, and depends on factors such as stoichiometry, lattice defects, and second phases present.

An interaction energy, W, is associated with the A and B atoms of the ordered alloy. The interaction energy is dependent on the configuration of atoms in the lattice, and is minimized for particular configuration. For example, W may be a minimum when the number of A-A and B-B nearest neighbor atom pairs is minimized. This is often the case when there is a significant size difference between the A and B atoms, and maximizing the number of A-B bonds minimizes the lattice strain energy. In other alloys, the configuration which minimizes W is dependent on electron/atom ratios in the unit cell, and the number of A-B bonds is not necessarily minimized. The atomic configuration which minimizes W in a

particular alloy system determines the type of ordered crystal structure. Variations of ordered crystal structures may also involve conditions on the number and type of next-nearest neighbor atomic bonds. This often results in large and complex unit cells.

Three of the more common types of crystal structures are close-packed, BCC derivatives, and topologically close packed (TCP). The BCC derivative structure includes many alloys of interest, including those used in the present study, FeAl (B2) and Fe_3Al (DO_3). The atom configuration of the B2 and DO_3 unit cells are shown in Figs. 2.3a and 2.3b, respectively. The B2 structure consists of two interpenetrating simple cubic lattices in which A atoms are sublattice I, and B atoms are on sublattice II. The DO_3 lattice consists of four interpenetrating FCC lattices, with A atoms on sublattices I, II, and III, and B atoms on sublattice IV.

The close-packed structure includes a wide variety of alloys which are currently being studied, such as Ni_3Al ($L1_2$ type) and Al_3Ti (DO_{22}). The TCP structure is well known for brittle and undesirable phases, such as Laves and Sigma phases, which may form in nickel-base superalloys.

At temperatures below Tc the interaction energy W is much larger than the thermal energy, given by:

$$E_{Thermal} = kT, \qquad \text{Eq. 3.}$$

where k is the boltzman constant and T is the absolute temperature. Therefore, atomic ordering is driven by the need to minimize W which will minimize the overall internal energy of the material. However, at temperatures above Tc, $E_{thermal}$ is much larger than W. Minimizing W by atomic ordering would have a negligible effect on the overall energy in this case. The alloy becomes disordered with a random distribution of the atoms.

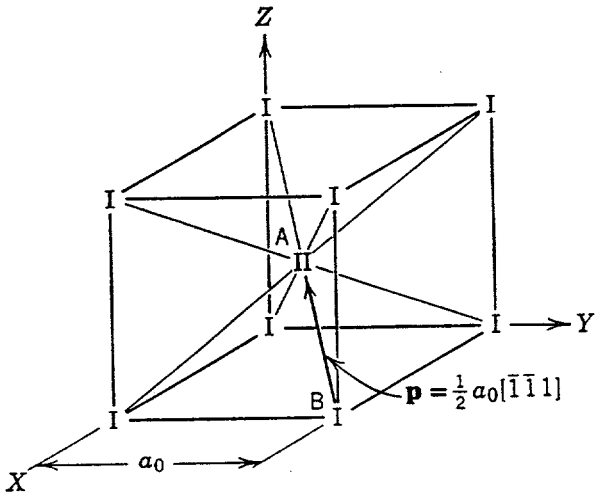

(a)

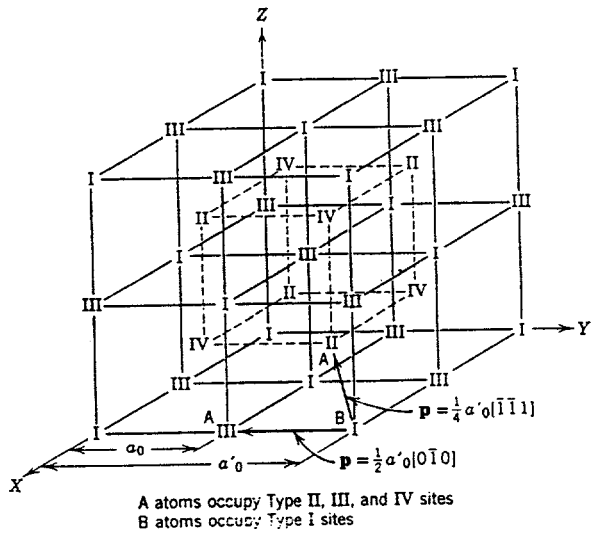

(b)

Fig. 2.3 Schematic of B2 (a) and DO_3 (b) unit cells.

Near Tc, when W is approximately equal to $E_{Thermal}$, the alloy may be partially ordered. In a partially ordered binary A_xB_y, the number of A atoms which are on A sites, or B atoms on B sites, in the lattice is greater than what would be expected for a random distribution. The degree of ordering is expressed by the ordering parameter S in Eq. 4

$$S = \frac{F(A,a) - F(A)}{1 - F(A)} \qquad \text{Eq. 4.}$$

where F(A,a) is the fraction of A atoms on A sites and F(A) is the total percentage of A atoms in the alloy. It can be seen from Eq. 4 that the order parameter S ranges from 0, when the alloy is completely disordered to 1 when the alloy is completely ordered. Some alloys experience a continuous decrease in order parameter as temperature is increased through Tc, such as FeCo (52), while others exhibit an abrupt loss of order at T_C, such as Cu_3Au (53). The temperature region of intermediate values of S indicates the onset of changes in properties due to the loss of order.

2.2.3 Anti-Phase Domains, Anti-Phase Boundaries, and Superlattice Dislocations

The periodic arrangement of atoms on an ordered lattice extends perfectly throughout the entire crystal in a defect-free single crystal material, or throughout entire grains in defect-free polycrystalline materials. Plastic deformation by unit dislocations disturbs the periodic arrangement by the introduction or removal of extra atom planes. Order exists on either side of the unit dislocation, but the two regions of order are out of phase from one another. For the simple binary alloy AB, illustrated in Fig. 2.4, each ordered region contains only unlike A-B nearest neighbor bonds. The pattern at the boundary where the two regions meet is disturbed, and contains A-A and B-B bonds. Each of the regions of order are called anti-

phase domains (APD's), and the boundary between APD's is called an anti-phase boundary (APB). The type of APB shown in Fig. 2.4 is found in B2 ordered lattices and is known as a nearest-neighbor APB (NNAPB). A atoms which had B atoms as their nearest neighbor now have A atom nearest neighbors. More complex structures, as the DO_3 type lattice can have next-nearest neighbor APB's (NNNAPB).

As the unit dislocation moves through the ordered lattice, the atomic order is continuously destroyed, and one APD grows at the expense of an adjacent APD. This type of dislocation motion is not energetically favorable as the interaction energy corresponding to the ordered configuration must be increased to that of a disordered configuration. An anti-phase boundary energy can be defined which is proportional to the difference in interaction energies of unlike A-B bonds and the average of A-A and B-B bonds. The APB energy gives a relative measure of the difficulty in disturbing the atomic order. The energy, or stress levels required, to create APB's and move dislocations through an ordered lattice is generally higher than for the same alloy in the disordered state.

Dislocations of the same sign traveling in pairs can move through the ordered lattice without leaving behind an APD. The trailing dislocation restores the order which was disturbed by the leading dislocation. The only disturbance in the atomic order is a strip of APD between the pair, and the energy increase in the lattice due to disturbance of the ordered structure is minimized. These pairs are referred to as superlattice dislocations. A superlattice dislocation of the type observed in B2 ordered lattices is shown in Fig. 2.5. The spacing between the two dislocations is determined the by APB energy, and increases as APB energy decreases.

In some ordered structures it is energetically favorable for each dislocation of the superlattice dislocation to dissociate into two partial dislocations, creating a 4-fold superlattice dislocation. In this case there is a stacking fault or NNNAPB between each dissociated member of the pair, and a strip of APB between the two pairs (Fig. 2.6).

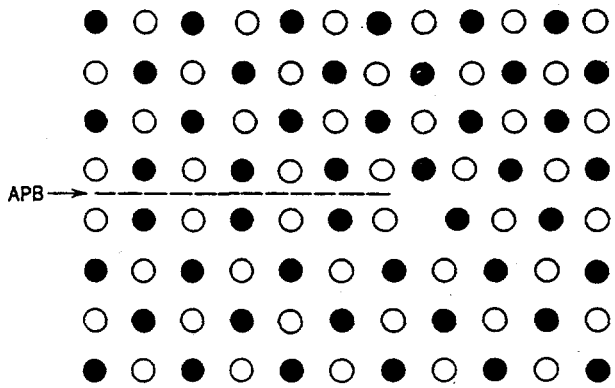

Fig. 2.4 Region of disorder created by a unit dislocation in an ordered alloy.

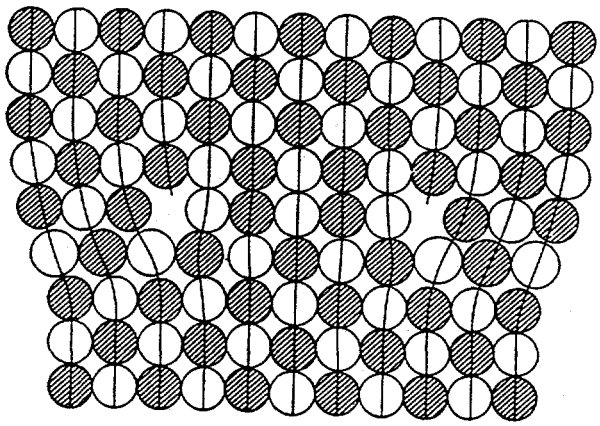

Fig. 2.5 Superlattice dislocation in a B2 ordered lattice.

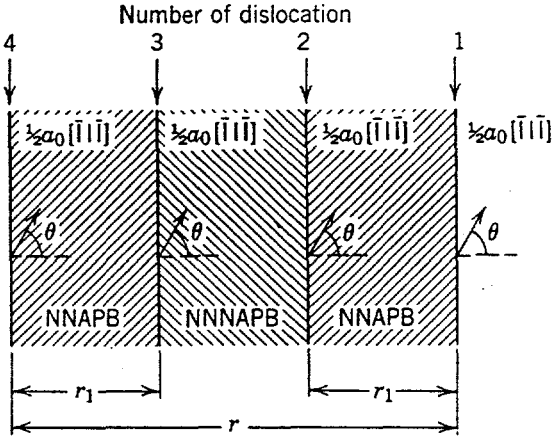

Fig. 2.6 Four-fold superlattice dislocation in a DO_3 ordered lattice

When a disordered alloy is annealed at a temperature in its ordered range, small regions of order nucleate and grow through the material. These regions will grow until they impinge upon a grain boundary or another ordered region. When two ordered regions impinge, they will often be out of phase with one another and an APB is formed. These are thermal APB's and do not involve dislocation motion. For some alloys and annealing conditions the smaller domains will gradually be incorporated into the larger ones, eliminating the thermal APB's.

2.2.4 Effect of Order on Mechanical Properties

Atomic ordering has a great influence on the mechanical and electrical properties in intermetallic compounds. These properties include yield strength, tensile strength, ductility, strain hardening, toughness, fatigue resistance, creep resistance, diffusion, corrosion, environmental embrittlement, and electrical resistance. The effect of ordering on these properties can be attributed primarily to changes in dislocation structure and slip behavior, and to changes in diffusion rates. Dislocation structure and slip phenomena determine the mechanical properties which involve plastic deformation, such as yielding, fatigue resistance, and ductility. Diffusion rates control the rates at which creep and, in some instances, corrosion and embrittlement can occur. Diffusion rates can also affect dislocation motion during diffusion-assisted climb and cross slip. The effects of order on various mechanical properties and environmental embrittlement will be discussed in more detail in the following sections.

2.2.5 Mobility of Superlattice Dislocations

The greatest influence of an ordered structure on the plastic deformation of an alloy is due to a restriction of cross slip and number of slip systems. Two-fold and four-fold

superlattice dislocations which are generated in the ordered lattice have great difficulty undergoing cross-slip. When the leading dislocation of a super-dislocation reaches the intersection of two slip planes, it may cross slip to the second plane under an appropriate loading condition. However, once on the second plane it may become sessile if the trailing dislocation remains on the original plane. At slip plane intersections, dislocation pile-ups occur which result in stress concentrations and sites for premature fracture.

Cross slip is inhibited also by the relatively low diffusion rates of many ordered alloys. Diffusion rates are found to drop in intermetallic compounds when they transform into their ordered state, such as in Ni_3Pt and Ni_3Fe (54). A dislocation which is sessile on one particular plane may undergo diffusion-assisted climb to reach a plane on which it is mobile. In the ordered alloys the likelihood of climb of sessile dislocations is reduced. Many ordered alloys become quite ductile at elevated temperatures because thermally activated climb relieves the pile-ups.

Dislocation mobility is very closely related to the APB energy. Cross slip of superlattice dislocations is more likely to occur when the partial dislocations are very close together, which occurs when the APB energy is high. Also, when the APB energy is low and the spacing between partials is high there is a larger region disordered material between the partials and more energy is required to move these dislocations.

The APB energy of an ordered alloy is very sensitive to stoichiometry and changes in alloy composition. The APB energy and resulting slip mechanisms active in Fe_3Al alloys, for example, are very dependent on the aluminum concentration of the alloy. The NNAPB energy increases quickly from 101 to 152 dyne/cm as the aluminum concentration increases from 25% to 35%, and that for NNN APB's decreases form 115 to 36 dyne/cm over the same range (55). The shear stress required to produce NNN and NN APB's can be calculated from the relation in Eq. 5,

$$\tau_{APB} = \frac{\gamma}{|b|} \quad , \qquad \text{Eq.5.}$$

where γ is the APB energy and b is the Burger's vector of the super-dislocation formed. At aluminum concentrations below 31%, the stress needed to form the NNN APB required for a perfect DO_3 type 4-fold superlattice dislocation is higher than that required to nucleate an ordinary dislocation. Slip, therefore, occurs by nucleation and motion of unit dislocations when the Al content is below 28%. When the Al content is above 31%, the alloys can nucleate superlattice dislocations and deformation occurs by motion of paired superlattice dislocations. This effect can be readily observed by examining slip lines on the surface of deformed Fe_3Al (52, 55). Below 31% Al, the slip lines are wavy, indicating slip by ordinary dislocations which are relatively free to cross slip. Above 31% Al, the slip lines are coarse and straight, indicating superlattice dislocations which tend to be confined to a particular slip plane. This correlation between slip line appearance and motion of ordinary or superlattice dislocations is observed also in ordered alloys which can be annealed to form either an ordered or disordered structure. In FeCoV (52), straight slip lines are observed in the ordered state while wavy slip lines are observed in the disordered state.

Temperature affects the APB energy of ordered alloys as well, and this is a cause for the unique tensile behavior observed in ordered alloys. Many ordered intermetallics exhibit an increase and peak in yield strength as temperature increases , before the yield strength begins to decrease with temperature as is common in disordered alloys. The anomalous yield strength peak often coincides with the transition temperature, T_C, between ordered and disordered states, or two different ordered structures.

Different mechanisms are responsible for the anomalous yield behavior for different alloys. In Fe_3Al, Park et. al. (56) proposed that the effect is due to a change in the superlattice dislocation type. As temperature rises above room temperature, 2-fold B2 type

superlattice dislocations begin to nucleate in preference to the 4-fold DO_3 type. However, they are less mobile in the DO_3 ordered lattice, and the yield stress increases until T_C is approached, at which a B2 structure begins to form and the 2-fold dislocations can move more freely. Other theories have attributed the yield stress peak in Fe_3Al to the existence of a 2-phase $DO_3+\alpha$ region below T_C and a 2-phase $B2+\alpha$ region above T_C (57).

In some $L1_2$ alloys there is no yield stress anomaly because superlattice dislocations dissociate at low temperatures and become sessile.

The unique interactions of dislocations in an ordered material are responsible also for the high strain hardening rates observed in many ordered alloys, particularly in $L1_2$, B2, and DO_3 structures. Strain hardening is typically due to the inability of dislocations to cross slip past pile-ups which normally occur during plastic deformation. In Fe_3Al alloys high strain hardening rates occur when the aluminum concentration is high and superlattice dislocations can nucleate, and low strain hardening rates when the aluminum concentration is low and ordinary dislocations dominate (58).

The high strain hardening rates in ordered intermetallic alloys are one reason why many ordered alloys exhibit significant ductility, yet still have a fracture surface appearance which often is typical of brittle failure, such as transgranular cleavage facets or grain boundary failure. As the ordered intermetallic strains plastically, the required applied stress increases steadily so that the cleavage or grain boundary fracture strength is overcome before ductile tearing takes place.

2.3 Fe_3Al Alloy System

The Fe_3Al intermetallic phase of the Fe-Al system (shown in Fig. 2.7) exists at aluminum compositions from 24%-32%. The ordered range of the phase diagram is shown

in more detail in Fig. 2.8. Fe_3Al within this Al concentration range can exhibit two different ordered states, as well as a disordered state, depending on the temperature. The DO_3 structure (shown in Fig. 2.3b) exists at temperatures below 560°C, while the B2 structure (shown in Fig. 2.3a) exists at temperatures from 560°C to 800°C. Above 800°C long range ordered breaks down and a disordered α phase forms.

The kinetics of the phase transformation from disordered α to the B2 structure is rapid enough that only a very small percentage of α can be retained in the B2 phase on a rapid quench from above T_C. The rate at which the B2 structure transforms DO_3 is much slower. It is possible to retain a predominantly B2 ordered structure at room temperature by quenching from above 560°C. A two-phase structure consisting of α + DO_3 can be maintained at the appropriate Al concentration (see Fig. 2.8).

2.3.1 Properties of Iron Aluminides

Iron-aluminum intermetallics do not possess high room temperature ductility in air, typically 2-8%, depending on the ordered state and aluminum content. Like many other intermetallics and steels, Fe_3Al has been shown to be susceptible to embrittlement, which is one cause for the low ductility

Fe_3Al alloys have demonstrated ductility of up to 20% when tested in vacuum or gaseous oxygen environments (17, 59, 60). This result indicates that Fe_3Al is a moderately ductile material and some environmental interaction is causing the low ductility in air. Fe_3Al alloys have been shown to undergo (110) <111> type slip which provides for at least 5 slip systems, exhibit only moderate yield and tensile strength, and fracture in a generally transgranular manner (61), all of which are properties associated with inherently ductile materials.

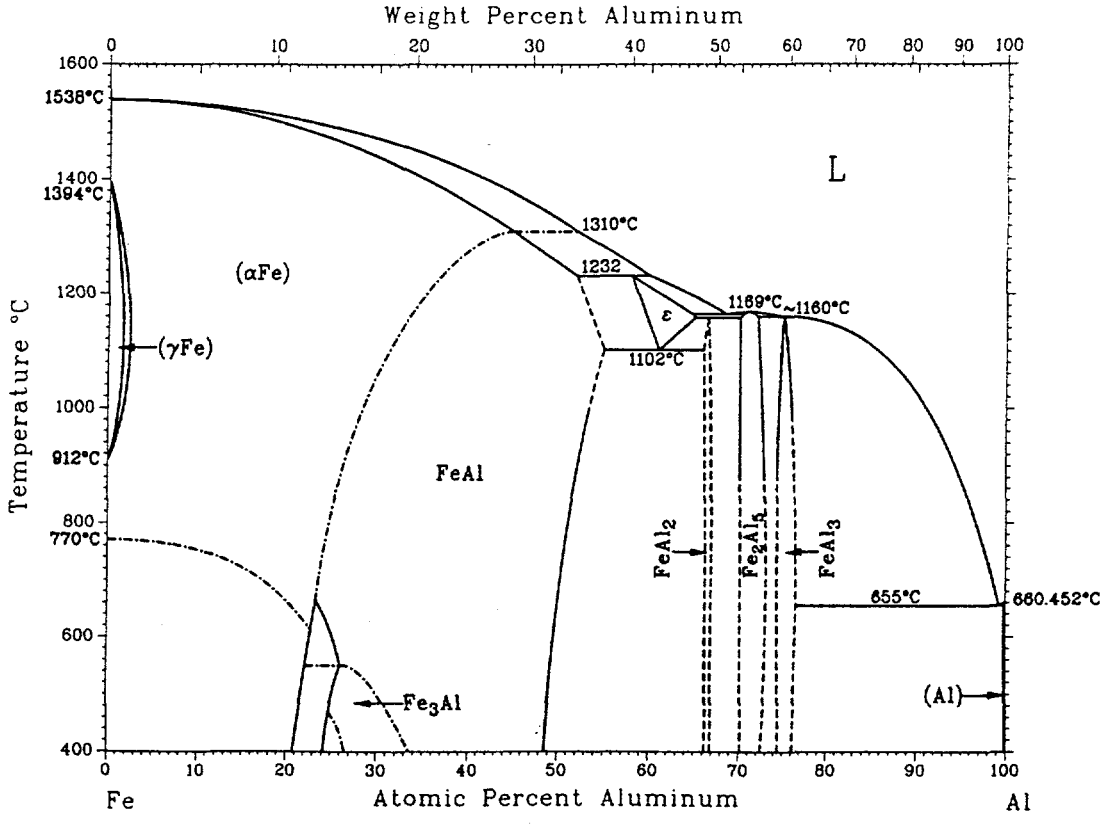

Fig. 2.7 Fe-Al Phase Diagram (62).

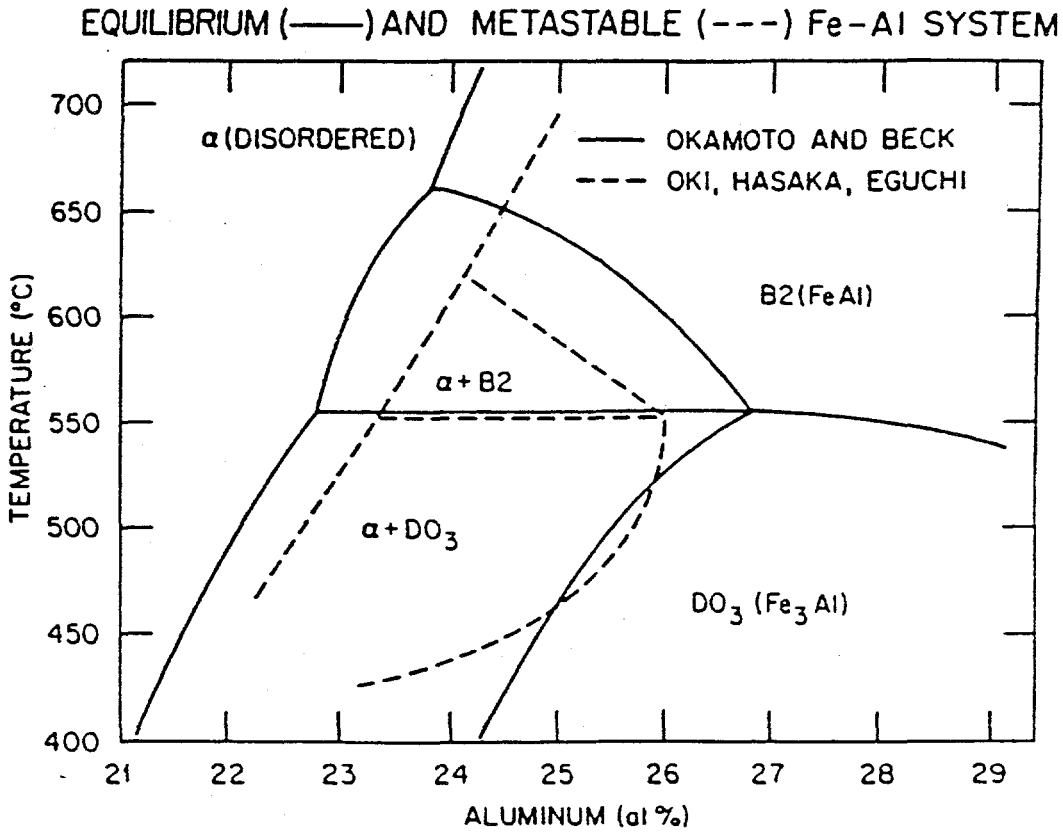

Fig. 2.8 Ordered Fe_3Al region of the Fe-Al phase diagram (63).

The inherent ductility of iron aluminides, as measured at room temperature in an inert environment such as oxygen or vacuum, is very sensitive to changes in aluminum concentration in the alloy. A combination of changes in the ordered structure, slip mechanisms, and grain boundary chemistry is responsible.

Fe-Al alloys which contain less than 20% Al are inherently ductile. Plastic strain to failure of 15-20% in inert environments is typical. These low aluminum alloys lie outside the ordered region of the phase diagram, and thus lack the ordered DO_3 phase which is often accompanied by brittle behavior. When the aluminum content is increased to between 20-27% Al, the ductility in inert environments drops down to 6% or less (1, 16, 18, 61). The drop in ductility coincides with the appearance of the ordered phase. Iron aluminides with 20-27% Al are often two-phase materials, consisting of the ordered DO_3 phase and the disordered α phase. Nucleation and mobility of dislocations are inhibited by the two-phase structure. The predominant dislocation type is the ordinary single dislocation, which trails an APB as it moves through the ordered regions.

Inherent ductility rises again, up to 14%, at aluminum concentrations of 28-35%. The structure of the alloy is now completely ordered. There is a corresponding change in dislocation structure to glide of superlattice dislocations, which are more mobile than single dislocations in the ordered phase.

A final drop in ductility of iron aluminum alloys is observed when the aluminum concentration surpasses 35% (17). At these aluminum levels, the chemistry of the grain boundaries changes sufficiently such that they are prone to brittle intergranular failure at low stresses and low plastic strains. In contrast, the fracture surfaces of iron aluminides with less than 35% aluminum are nearly always transgranular in appearance.

2.3.2 Hydrogen Embrittlement in Iron Aluminides

With the ductile nature of iron aluminides in mind, many researchers have investigated the mechanisms of embrittlement in iron aluminides (17, 64), as well as methods of preventing embrittlement such as alloying or coating (16). Research conducted at the Oak Ridge National Laboratory (17) has shown that the predominant embrittling mechanism in Fe_3Al involves the chemical reaction with water vapor in the air and aluminum described in section 2.1.1.2. However, embrittlement in gaseous hydrogen can occur as well. There are many theories as to what happens after hydrogen is evolved at the surface, but little agreement on whether one or some combination of these is correct.

Embrittlement in iron aluminides containing over 20%Al under monotonic tension is consistently more severe in a moist air environment than in dry hydrogen gas. In addition, testing in a pure oxygen atmosphere effectively stops embrittlement and often results in ductility exceeding that in vacuum (7, 17, 18, 40). Liu, Lee, and McKamey (17) found that for a B2 ordered Fe-36.5%Al alloy tested in tension in various gaseous environments the lowest ductility was measured in laboratory air (2.2%) and H_2O vapor (2.4%). The ductilities in an argon-hydrogen mixture (5.5%) and a vacuum of 10^{-4} Pa (5.4%) were somewhat higher, while the best ductility was measured in oxygen at 11.3%. While both water vapor and hydrogen gas are clearly capable of embrittling the iron aluminide, water vapor is much more detrimental. It was concluded that oxygen acts as an inhibitor to hydrogen embrittlement via the H_2O + Al reaction. Possible explanations are that oxygen oxidizes the aluminum available at the surface, thereby preventing the H_2O reaction, or that oxygen effectively covers the surface of the material preventing the H_2O molecules from reaching the aluminum. Oxygen may also act to inhibit dissociation of hydrogen molecules into hydrogen atoms at the surface of a metal specimen, having the opposite effect of recombination poisons discussed previously.

Adsorbed oxygen has been observed to decrease the embrittling effect of hydrogen gas in martensitic steels (65), suggesting a surface coverage effect. In Fe-33Al and Fe-35Al alloys, water vapor - oxygen mixture has been shown to be somewhat less embrittling than a water vapor - argon mixture (3). However, both environments result in higher ductilities than an equivalent partial pressure of water vapor in vacuum. This suggests that both the oxidation and surface coverage mechanisms may be active in the aluminum-containing alloys. George, Liu, and Pope (13) found a similar effect of oxygen on Ni-23.4Al, where embrittlement in oxygen was much less severe than that in vacuum for the same levels of water vapor content.

Single crystal Fe_3Al alloys are subject to embrittlement in the same manner as polycrystalline Fe_3Al. Lynch, Gee, and Heldt (66) found that single crystal Fe-35Al suffered a loss of ductility from 22.7% in oxygen to 4.5% in air. The air environment caused no change in the preferred cleavage planes for fracture, which were predominantly (100) planes.

A precise threshold concentration of water vapor or hydrogen gas for embrittlement of Fe_3Al alloys has not been observed. Iron aluminides exhibit only a weak concentration dependence on embrittling water vapor when concentrations exceed 10^4 vpm. However, below this concentration there is a pronounced concentration dependence. Water vapor concentrations of as low as 5 vpm have been shown to significantly reduce ductility. Lynch and Heldt (3) have shown that the ductilities of Fe-33Al and Fe-35Al alloys during tensile tests at slow strain rates (3.3×10^{-4} / sec) are sensitive to water vapor concentrations between 5 and 1000 vpm. In an oxygen-water vapor mixture, ductility dropped from 9% at 5 vpm to 4.5% at 500 vpm, and no plateau was observed in a plot of ductility versus water vapor concentration. Sensitivity to very small concentrations of H_2O, with no apparent threshold occurs in the intermetallic Ni_3Al as well. George, Liu, and Pope (13) found that the ductility in Ni-23.4Al increases sharply in vacuum as the pressure is dropped below

10^{-4} Pa. Above this pressure there is little change in ductility, but below 10^{-4} Pa, ductility rises rapidly, up to 23% at 10^{-8} Pa, and again with no evidence of a plateau

While environment has a great effect on ductility and fracture toughness of iron aluminides, it has little or no effect on many other properties such as yield stress and strain hardening rate. These parameters are much more sensitive to changes in stoichiometry and alloy composition.

The appearance of the fracture surface in Fe_3Al for various compositions and environments can serve as an indicator of the mechanism of embrittlement. It has been observed that the fracture surface of iron aluminum alloys is very dependent on aluminum concentration, but only slightly sensitive to environment. Several studies have reported what type of fracture surface (TG, IG, or mixed) is expected for various aluminum concentrations when iron aluminides are tensile tested in air.

In binary Fe_3Al alloys tested in tension, a TG fracture mode is reported for alloys with less than 30%Al (1, 3, 18, 34), mixed mode TG and IG for alloys with 30-37%Al (1, 3), and IG for alloys with more than 37% Al (1, 67). The shift to IG failure as aluminum concentration increases is believed to be a result of weakened grain boundaries as their composition changes (1, 35).

Changes in fracture mode as the environment changes have been observed in binary alloys only when the aluminum concentration is between 35% and 36%. Binary Fe-35.5Al (17) undergoes a shift in fracture mode from TG in air to mixed mode in vacuum, and IG in oxygen; and binary Fe-36.5 has its fracture mode change from TG in air to mixed TG+IG in vacuum to IG in oxygen. Above 37% aluminum, binary iron aluminides fail intergranularly in both air and oxygen, while below 30% aluminum they fail transgranularly in hydrogen gas, air, vacuum or oxygen.

The shift in fracture mode from TG in the aggressive air environment to IG in the inert oxygen environment at aluminum concentrations of 35-57% indicates that hydrogen acts

on cleavage planes in iron-aluminum alloys. At aluminum concentrations well below 37%, the cleavage planes are weakened due to an embrittling environment, but the fracture mode remains unchanged because the grain boundary strength is higher than the cleavage strength in either environment. At aluminum concentrations above 37%, the grain boundary strength is greatly reduced by the high aluminum content. The grain boundaries become the weak point of the material in both air and oxygen even though there is a significant reduction in cleavage strength in the moisture-bearing air environment. The binary iron aluminides at 35-37% aluminum are near the observed cut-off between TG and IG fracture mode in air. The proximity of these alloys to the cutoff for fracture mode suggests that the grain boundary strength and cleavage strength are nearly equal, and that exposure of the alloy to moisture bearing air is sufficient to reduce the cleavage strength below the grain boundary strength in air, while in oxygen the intrinsic cleavage strength is higher than the grain boundary strength. When tested in vacuum, the alloys with 35-37% aluminum appear to have nearly equal cleavage and grain boundary strengths, which results in the mixed TG-IG fracture mode. It is clear that the natural humidity found in laboratory vacuum is sufficient to embrittle the iron aluminides (3).

The surface condition plays a role in the ductility and resistance to embrittlement of iron aluminides, especially in monotonic tension. McKamey and Liu (16) found that the tensile ductility in air of an Fe-28%Al-4Cr alloy can be increased when there is a protective oxide coating on the surface. The coatings they examined were a fine oxide layer created by polishing the surface and annealing in air, and a coarse oxide scale which was imparted when the material was rolled. The Cr addition to the alloy was crucial to the effectiveness of the coating, as a binary Fe-28%Al alloy showed no increase in ductility with similar processing procedures. It was theorized that Cr either modifies the coating chemistry to make it more impervious to diffusion of the embrittling species, or more resistant to cracking.

A similar effect can be achieved by simply coating the surface of the iron aluminide with oil, or some other barrier. For example, Liu, Lee and McKamey (17) measured an increase in tensile ductility in air of Fe-36.5%Al from 2.2% to 5.6% when a layer of oil was applied to the surface. However, the oil coating was not completely impervious to the embrittling environment, as the ductility measured in oxygen was 11.3%.

In aqueous environments, surface condition plays a large role in resisting corrosion and embrittlement. The corrosion rate of a material will decrease if a passive film forms at the surface, and alloying additions which make the passive film more stable will aid in corrosion and embrittlement resistance. Cr and Mo are two additions which have been shown to increase the passivation breakdown potential for iron aluminides in aqueous solutions (68 , 69 , 70).

A survey of data from the literature on ductility and embrittlement of iron aluminides is shown in Appendix A.

2.3.3 Improving the Mechanical Properties of Iron Aluminides

The ductility of Fe_3Al in air has been improved with alloying additions such as Cr. McKamey, Horton, and Liu (61) improved the room temperature ductility of DO_3 ordered Fe-28%Al from 3.7% to 9.4% with the addition of 2%Cr. The ductility increase was attributed to changes in the APB energy which allows for easier cross slip. No effect on degree of ordering was noted, only a small shift in T_C. Cr additions decreased the yield strength slightly as well, from 279 MPa to 247 MPa, due to a solid solution softening effect. Further increases in the Cr content did not improve the ductility. The effect of Cr on the alloy is attributed to an increase in cleavage strength and a change in slip character (61, 71). Slip band markings are seen to shift from coarse straight bands in the alloy without Cr to fine wavy slip lines in the alloy with Cr, indicating an increased incidence of cross slip. It was found that Cr decreases the APB energy of iron aluminides, which increases the

dislocation spacing between the individual dislocations of 4-fold superlattice dislocations. The super-dislocations are much more likely to dissociate, enabling cross slip to occur. A similar effect on APB energy is seen in the FeCo system, where additions of V will reduce the APB energy and make cross slip more likely.

The fracture surface changes from transgranular cleavage without Cr to 50% transgranular - 50% intergranular, which indicates that the cleavage strength is increased beyond that of the grain boundary strength. Clearly, intergranular fracture does not necessarily indicate brittle fracture in the iron aluminides.

Another attempt at ductility enhancements via alloying has been the addition of boron. Ductilization of nickel aluminides by micro-alloying with boron is a well-known phenomenon. Binary Ni_3Al is generally extremely brittle at room temperature in air. Ductility is nearly zero and the observed fracture surface is intergranular in nature. However, microalloying with boron can increase the ductility dramatically. Liu, White, and Horton (72) were able to increase the ductility of Ni-24Al from less than 1% to 54% when 0.1 wt.% B was added. The fracture surface changes from intergranular to transgranular with the boron addition. Analysis showed that the boron segregates strongly to the grain boundaries, indicating that B has a strengthening effect on grain boundaries.

The effect of aluminum concentration on the ductility and fracture surface of Fe_3Al (increasing Al% above 37% reduces ductility and promotes intergranular failure) was observed in Ni_3Al as well by Liu, et.al. In B-doped Ni_3Al, the ductility was seen to decrease from 49.4% at 24%Al to 37% at 24.5%Al to 0% at 26%Al, and the fracture surface appearance shifted from TG to mixed TG+IG to IG. As with the iron aluminides, the effect of increasing Al content is believed to be due to a decrease in grain boundary cohesive strength.

Similar attempts have been made to ductilize iron aluminides with boron (73, 74, 75, 76). Horton, Liu, and Koch (76) added 0.24%B to Fe-25Al, but found no change in

ductility in air, which was < 3%, or fracture surface appearance, which was transgranular. However, other researchers have observed a slight ductilizing effect of boron on Fe-40Al alloys. Gaydosh and Nathal (75) noted an increase in ductility from 0.8% to 2.8% with the addition of 0.5% B in a powder-processed Fe-40Al alloy, and Liu and George (74) observed a ductility increase from 1.2% to 4.3% with the addition of 0.12% B to a cast Fe-40Al alloy. Both studies also noted a shift in the fracture surface appearance from intergranular without boron to transgranular with boron. Liu and George found also that boron segregates strongly to grain boundaries in Fe_3Al as it does in Ni_3Al. These findings point to boron increasing the grain boundary cohesive strength. The fact that no effect of boron was found in Fe-25Al (76) suggests that the ductilization mechanism of boron is related to the aluminum concentration at the grain boundaries. When the bulk aluminum concentration is below the 37% boundary for transgranular / intergranular failure, the weak points in the material are the cleavage planes, so boron, which strengthens the grain boundaries, has no observable effect. When the bulk Al concentration is 40%, the grain boundaries are now the weak point and the effect of boron on grain boundaries can be observed.

The ductilizing effect of boron on Fe-Al alloys in air is not nearly as large as the effect in Ni_3Al because the Fe-Al alloys are still being embrittled by the moisture-bearing air environment, which attacks cleavage planes. Although boron may greatly increase the grain boundary cohesive strength in air, that increase is of little benefit because the cleavage strength is exceeded well before the enhanced grain boundary strength is reached.

Liu and George demonstrated that boron-doped Fe-40Al suffers from severe environmental embrittlement. When tested in oxygen, the ductility was 16.8%, compared to 4.3% in air. The fracture surface remained transgranular in both air and oxygen, compared to Fe-35.5Al (73) and Fe-36.5Al (17) which exhibit intergranular failure in inert environments. In the boron-doped alloy, the grain boundaries are stronger than the cleavage

planes in both inert and aggressive environments. Ni_3Al, on the other hand, is very ductile in both inert ultra-high vacuum without boron (13) and in moisture-bearing air with boron (10, 11, 12).

Further improvements in ductility of iron aluminides can be realized by increasing the purity. Kasul and Heldt (77) found that Fe_3Al with high levels of impurities will tend to fail in an intergranular or mixed-mode manner, while ductility is improved and transgranular failure is observed when high purity components are used in the alloy. Kerr (2) noted an effect of low carbon levels on ductility. The ductility of an Fe-25.5Al alloy containing 500 ppm carbon was measured as 2.1%, but when the same alloy was decarburized to bring the carbon level down to 50 ppm, the ductility was nearly doubled to 4.1%. The carbon atoms formed a second phase, Fe_3AlC, which precipitated along the grain boundaries during annealing.

At present, the most promising of the iron aluminum alloys are those with 28-30% Al, and additions of up to 5% Cr. Further attempts to improve the tensile properties of these alloys are based on varying the processing and annealing parameters, which can affect the grain structure, dislocation structure, and ordered character of the alloy.

Iron aluminides which are prepared by casting and some combination of rolling or extrusion often are not fully recrystallized, and may have a pronounced directionality to the grain orientation. McKamey and Pierce (78) surveyed the effect of degree of recrystallization on an Fe-28Al-5Cr alloy. Recrystallization was controlled by varying the annealing temperature. There is a peak in ductility of 8.1% when the alloy is annealed at 750°C and is 10% recrystallized. Material which completely retains the as-rolled structure suffers a drop in ductility to 5.4%, and there is a similar drop for fully recrystallized material. The possible explanations are that the elongated grains imparted by the rolling process minimize the number of cleavage planes oriented parallel to the fracture plane, or that the unrecrystallized structure enhances dislocation mobility.

Warm working iron aluminides has a beneficial effect as well. Lynch and Heldt (3) were able to improve the ductility of partially unrecrystallized Fe-24.6Al from 4.0% to 6.4% in air by rolling the material at 700°C to a 45% reduction in thickness. However, warm working had no effect when the alloy was tested in oxygen. In both the worked and unworked conditions the ductility was 9%.

Another shortcoming of the iron aluminum alloys is their poor creep resistance and low strength at temperatures above 600°C. One way this difficulty has been addressed is solid solution strengthening with ternary additions. Mendiratta et. al. (79) were able to increase the yield strength in bending of Fe-35at.%Al at 700°C from 124 MPa to 331 MPa with the addition of 4at.%Ti, to 379 MPa with 1 at.%Mo, and to 345 MPa with 2 at.%Si. They found similar results with additions of V, Ni, Nb, Ta, and W. No significant effect on ductility was noted with these alloying additions. Diehm and Mikkola (80) found that they could increase the yield strength at 700°C of an Fe-27.4%Al alloy from less than 100 MPa to 650 MPa by alloying with Mo and Ti. They observed that besides increasing the yield stress at all temperatures by a solid solution effect, the anomalous peak in yield stress vs. temperature was shifted by 100°C, from 550°C to 650°C resulting in dramatically better strength at the elevated temperatures. The shift of the yield stress peak is attributed to an increase in the critical ordering temperature caused by the Mo and Ti additions.

McKamey, Maziasz, and Jones (81) found that additions of Mo also dramatically increased creep life at 600°C. For an applied stress of 138 MPa, creep life in an Fe-28%Al was increased from 87 hours to 835 hours with the addition of 2% Mo.

2.4 Fatigue Crack Growth

Fatigue of metals can be divided into two phases, nucleation of a crack and propagation. Crack nucleation in fatigue is dependent on plastic deformation and dislocation interaction. In material with limited cross slip and few slip systems, the resistance to crack nucleation under cyclic loading increases. This is the case for many ordered intermetallics.

Planar slip, which is often observed with superlattice dislocations, enhances resistance to crack nucleation by slip reversibility (82). Slip reversibility occurs when slip steps which would normally form at the surface of a fatigued material and act as nucleation sites are either annihilated or do no form to the same extent because slip which occurs during the tensile portion of the loading cycle is reversed during the unloading or compressive portion. Reversibility is likely when slip is constricted to a few crystal planes, or slip is planar. Planar slip in ordered alloys which deform by superlattice dislocations has been attributed to a lowered APB energy on planes in which slip does not normally occur. Kear (83) found that the APB energy in Cu_3Au crystals on {100} planes is much lower than on {111} planes, where slip normally occurs. Super-dislocations tend to cross-slip but become sessile on the {111} plane.

A good correlation was found between SFE and resistance to fatigue cracking by McEvily and Boettner in disordered Cu and Al alloys (82). Resistance to both crack nucleation and propagation increases as SFE decreases due to its effect on cross slip. Lower SFE, in addition to making cross slip less likely, increases the resistance to subgrain formation, which act as paths of enhanced crack growth.

A shift to an ordered structure has been shown to increase resistance to fatigue in several alloys. Boettner, Stoloff, and Davies (84) found that ordering increases the fatigue limit stress of FeCo-V and Ni_3Mn by approximately 20%. They attributed the increase to a

decrease in fatigue-induced surface roughness and crack nucleation sites as a result of inhibited cross slip.

There are a number of mechanical variables which affect the fatigue life or crack growth rates. These include waveform type, frequency, R-Ratio, mean stress, and specimen geometry. Environmental parameters which affect fatigue response are presence of embrittling species and temperature.

3 EXPERIMENTAL PROCEDURE

3.1 Alloy Composition and Heat Treatment

Three alloys were examined in this study, an Fe-28%Al alloy designated FA-129, an Fe-16 at.%Al alloy designated FAP-Y, and an Fe-35at.%Al alloy designated Fe-35Al. Alloy FA-129 is an ordered Fe_3Al type intermetallic, while Fe-35Al is a B2 ordered intermetallic. As can be seen from the Fe-Al phase diagram of Fig. 2.8, the 28 at.%Al alloy can exist in the B2 or DO_3 ordered state, depending on the temperature from which it is quenched, while the 35 at.% alloy is of the B2 type. The 16 at.%Al alloy FAP-Y is a disordered alloy. The compositions of these alloys are shown in Table 1. All alloys are fabricated at the Oak Ridge National Laboratory (ORNL) by vacuum induction melting, extrusion to a 2.54 cm thickness, and either hot or warm rolling to the final thickness. The final plate thickness of FA-129 used in compact tension specimens was 5.08 mm, while the final plate thickness for FA-129 used in tensile tests was 0.76 mm. All FAP-Y material was received in the form of 5.08 mm thick plate. All Fe-35Al material was received in the form of 12.7 mm thick plate.

Because the rolling process used in these materials imparts a certain directionality to the grain structure, the terms longitudinal, short transverse, and long transverse will be used to indicate the three perpendicular planes relative to the rolling direction. The longitudinal plane is the rolling plane, and the short and long transverse are the two remaining perpendicular planes, as illustrated in Fig. 3.1.

The annealing parameters for B2 ordered FA-129 consisted of a 700°C anneal for 1 hour with a mineral oil quench, which was then repeated. The annealing parameters for DO_3 ordered FA-129 were the same as for the B2 order heat treatment, with an additional reheat to 500°C for four days with a furnace cool. Fe-35Al and FAP-Y were annealed

TABLE 1
Composition and Grain Size of Annealed of Iron-Aluminum Alloys

	Atomic %		
	FAP-Y	FA-129	Fe-35Al
Fe	77.07	66.17	65.0
Al	16.12	28.08	35.0
Cr	5.44	5.04	-
Mo	1.07	-	-
Nb	-	0.51	-
Zr	0.11	-	-
C	0.13	0.20	-
Y	0.06	-	-
Grain Size	42μm	partially recrystallized	385μm

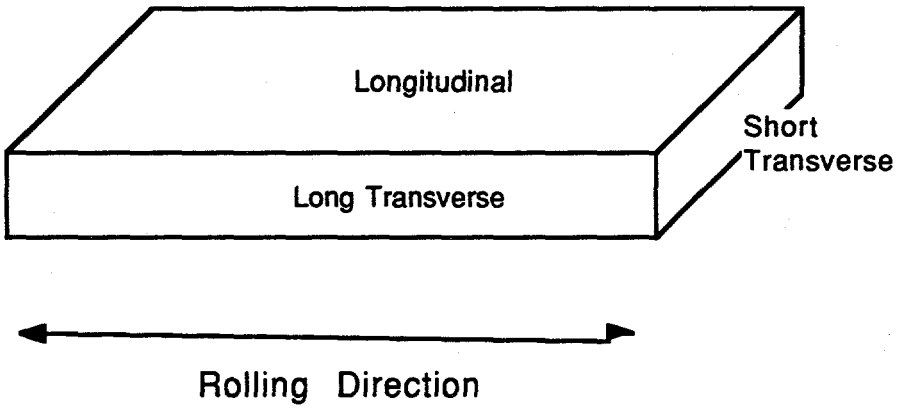

Fig. 3.1 Definition of longitudinal, short transverse, and long transverse planes on a rolled plate.

twice at 800°C for one hour with a furnace cool. A variation of the B2 heat treatment also was used for alloy FA-129, in which the first anneal was done at 900°C, and the second at 700°C. Both were one hour anneals followed by a mineral oil quench.

Metallography

Metallography was performed on all materials to examine the grain structure. Samples from each plate of material were cut on a cut-off wheel from the short transverse, long transverse, and longitudinal directions. These were mounted in either a bake-lite or epoxy mold. Polishing was performed on water lubricated polishing wheels with 240, 400, and 600 grit paper, followed by a cloth covered wheel impregnated with 16 and 9 μm diamond paste, and finally with a felt covered wheel coated with a 0.3 μm alumina slurry. The metallographic specimens were etched in glyceregia (30 ml glycerin, 30 ml HCl, 10 ml HNO_3) until the grain structure became visible. They were then photographed on a non-polarized metallograph. Polaroid no. 55 film was used in all metallography photographs.

3.2 Fatigue Crack Growth Tests

Fatigue crack growth tests were performed on alloy FA-129 in both the B2 and DO_3 ordered states, and on alloy FAP-Y and Fe-35Al. At room temperature, tests were conducted in hydrogen gas, laboratory air, and oxygen. Elevated temperature fatigue crack growth tests were conducted on FA-129 in air at 150°C in the B2 and DO_3 ordered state, and at 300°C and 450°C in the DO_3 ordered state. Note that the B2 ordered FA-129 was not tested at temperatures between 150°C and 550°C because the B2 lattice was expected to begin transforming to DO_3 at temperatures above 150°C.

Compact tension specimens were used in all fatigue tests and were cut by wire Electro-Discharge Machining such that the crack propagation direction would be perpendicular to

the rolling direction. Fig. 3.2 shows the specimen geometry and rolling direction. All specimens were polished to a 0.3μm finish and ultra-sonically cleansed in an acetone bath.

Crack length was monitored via the d.c. potential drop method. Fig. 3.3 shows the test set-up. A 10 amp current was supplied from a Hewlett Packard power supply via two current leads positioned on either side of the machine notch at a distance of 12.70 mm. The current was monitored via a resistive shunt, which led into an IBM PC computer fitted with a Metrabyte 12 bit analog to digital converter. The potential across the unbroken ligament was measured using with voltage probes on the compact tension specimen located on either side of the machined notch at a distance of 5.08 mm. In room temperature tests on alloy FA-129, the current leads and voltage probes were attached to the CT specimen using 2/72 sized machine screws bolted into holes which were drilled and tapped into the front face. However, this technique was not suitable for higher temperatures and in all other tests these connections were made by brazing the leads into short holes drilled into the front face.

Temperature was monitored at the specimen surface to correct for bulk resistivity changes using a chromel-alumel thermocouple cemented to the CT specimen as shown in Fig. 3.3. The thermocouple output was converted into a voltage proportional to the temperature by an Omega thermocouple reader, and this voltage directed into the analog to digital converter.

Calibration curves were created relating crack length to potential drop by optically measuring the crack length with a calibrated traveling microscope. This system was able to resolve changes in crack length of 50μm. The accuracy of the crack measurements was determined by the microscope used to form the optical calibration curves, which had an accuracy of 20μm. An example of the calibration curve obtained for alloy FA-129 is shown in Fig. 3.4

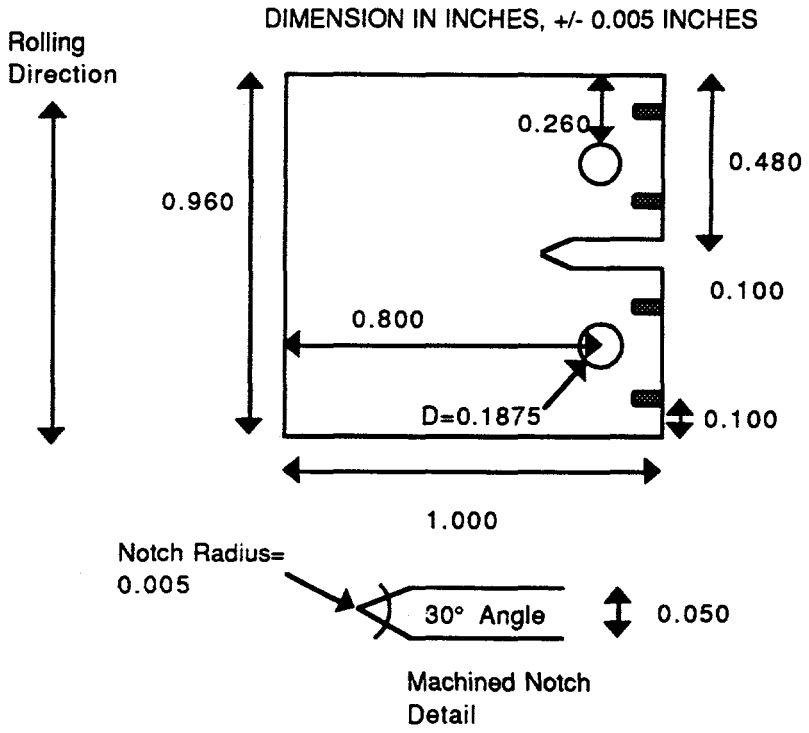

Fig. 3.2 Specifications of compact tension specimen.

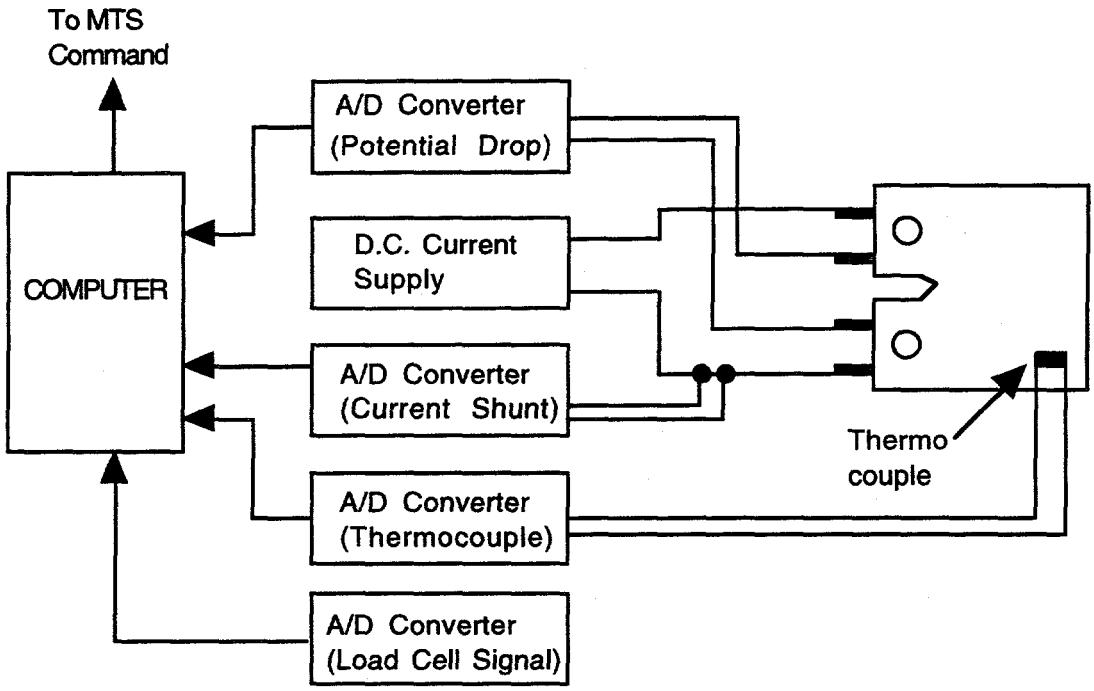

Fig. 3.3 Instrumentation set-up for d.c. potential drop system.

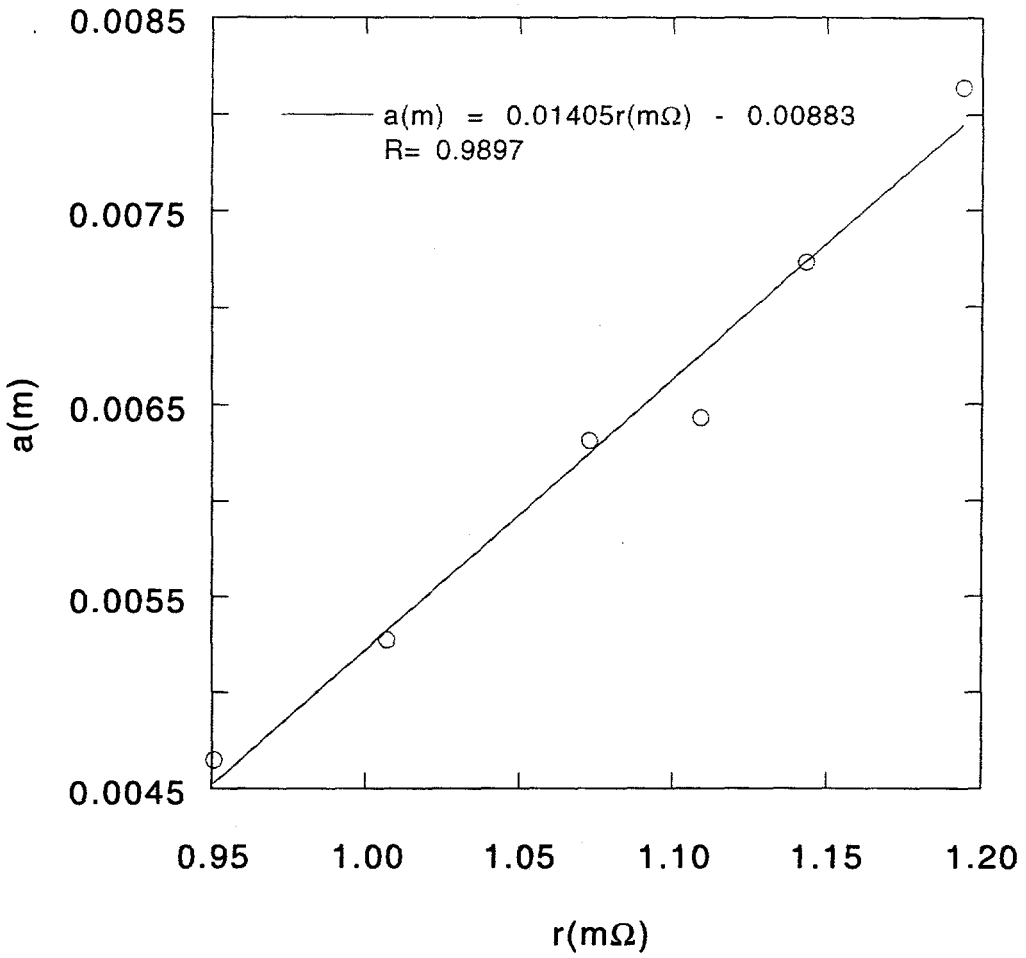

Fig. 3.4 Calibration curve relating resistance (mΩ) to crack length (m) in B2 ordered FA-129.

The load frame used was an MTS servo-hydraulic machine with a 22205 N load cell. Tests were run in load control using a sawtooth waveform and an R ratio ($\sigma_{min}/\sigma_{max}$) of 0.5. The standard test frequency was 20Hz. The effect of frequency was examined by fatiguing B2 ordered FA-129 at 2Hz, 0.2Hz, and 0.08Hz in addition to 20Hz. Also, the effect of R ratio was examined on several FA-129 samples.

Software written for a PC allowed a fully automated test procedure. The PC received the load applied to the specimen, current, voltage, and temperature via the analog to digital converter. The PC recorded these data, calculated the crack length, crack growth rate (da/dN) and stress intensity range (ΔK). The appropriate loading waveform was then calculated based on these measurements and the initially specified test parameters. The digital load waveform was then converted to analog form and sent to the MTS as a load-control input for the hydraulic actuators.

When testing in oxygen or hydrogen gas, the environmental chamber was first evacuated to $< 1.3 \times 10^{-4}$ Pa using a diffusion pump fitted with a liquid nitrogen cold trap. The appropriate gas was then admitted to the chamber at a pressure of 2300 Pa (1/3 psi) over atmospheric pressure. All gases used were of Ultra-High Purity Grade, with a maximum water vapor content of 3 ppm, which corresponds to a water vapor partial pressure of 0.3Pa at room temperature and one atmosphere.

All parameters of the fatigue crack growth tests followed the ASTM E-647 (85) procedures with the exception of the CT specimen size, which was slightly undersized due to constraints in material availability. The fatigue crack growth test was broken down into the following 5 stages:

1) Precracking of the CT specimens was accomplished by fatiguing in 20000 cycle increments at stress intensity levels increasing by 0.5 MPa$\sqrt{m}$ until crack initiation was observed.

2) A ΔK-increasing procedure was implemented at this point. The crack was grown approximately 0.5 mm from the 4.0 mm machined notch before collecting data to be used in the da/dN curves.

3) The ΔK-increasing procedure was continued until either the crack had propagated to 1.0 mm or a da/dN value of $1x10^{-8}$ m/cycle was achieved.

4) At this point a load shedding procedure was used to reduce the da/dN values back down to approximately $1x10^{-9}$ m/cycle to measure crack growth rates in the threshold region. This was the lowest growth rate that could be accurately and conveniently measured.

5) The ΔK-increasing routine was then continued until failure. In all stages the R-ratio was held at 0.5 and crack lengths recorded at intervals of 0.1 mm.

The following equation (85) for calculating the stress intensity range, ΔK, was used:

$$\Delta K = \frac{\Delta P}{B\sqrt{W}} \frac{(2+\alpha)}{(1-\alpha)^{3/2}} (0.886 + 4.64\alpha - 13.32\alpha^2 + 14.72\alpha^3 - 5.64\alpha^4) \qquad \text{Eq. 6}$$

In Eq. 6, ΔP is the cyclic load range, B is the specimen thickness, W is given by (specimen length / 1.25), and alpha is the ratio (crack length / W). The crack length is always measured from the center of the load-pin holes to the crack tip.

3.2.1 Crack Closure Measurements

A concern in the fatigue crack growth experiments was closure. To confirm that crack closure was not artificially increasing the critical and threshold stress intensities measured, closure measurements were made during a fatigue crack growth test at room temperature. An extensometer strapped to a pair of bolts set in the specimen face was used to measure

displacement of opposite faces of the machined notch at crack length intervals of 0.1 mm, and the corresponding values of crack opening displacement (COD) were calculated.

3.3 Tensile Tests

A series of tensile tests were conducted on alloys FA-129 and FAP-Y. Alloy FA-129 was tested in air, vacuum, and oxygen at temperatures of 25°C, 150°C, and 600°C for the B2 state, and at 25°C, 150°C, 300°C, and 450°C in the DO_3 state. The FA-129 specimens, as shown in Fig. 3.5a, were punched from 0.76 mm thick plate. Alloy FAP-Y was tested at 25°C in hydrogen gas, air, and oxygen. The FAP-Y tensile specimens were machined from 5.08 mm thick plate, and the specimen geometry is shown in Fig. 3.5b.

The specimens were pin loaded and tested in a servo-hydraulic MTS machine. The tensile tests were run in stroke control with the stroke feedback signal used as a measure of displacement. All tensile specimens were polished to a 0.3 μm finish and ultra-sonically cleansed in acetone prior to testing. The plastic strain rate used in these tests was 3.3×10^{-4} /sec. Two tests were performed in each condition, except in the vacuum environment at temperatures of 150-600°C. This was due to limited availability of material. The procedures for testing in gaseous environments which were previously described in section 3.2 for FCG tests were used in the tensile tests.

Liquid metal embrittlement tests were also performed on alloy FA-129 using the same geometry tensile bars described in Fig. 3.5a. Mercury was used as the embrittling agent and was applied in the form of a solution of 50 wt.% indium - 50 wt.% mercury solution. This solution allowed wetting of the tensile specimen. These tests were performed in an oxygen environment to preclude any effects of hydrogen embrittlement. The procedure of evacuating the test chamber before admitting the oxygen had to be altered to avoid

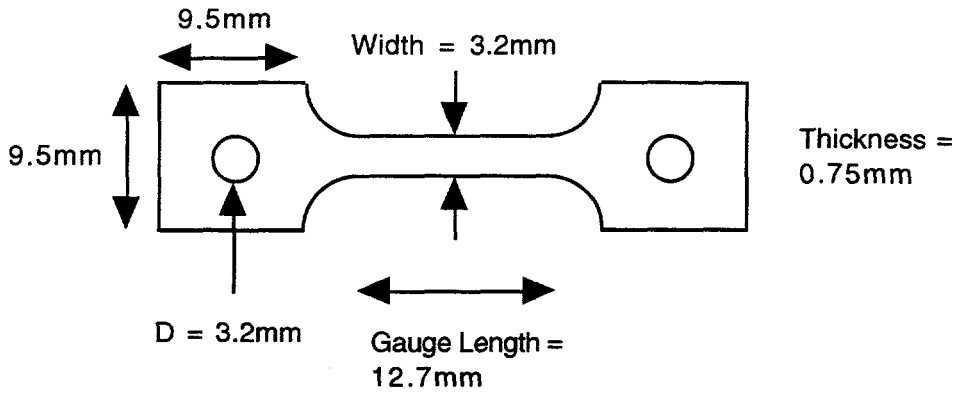

(a)

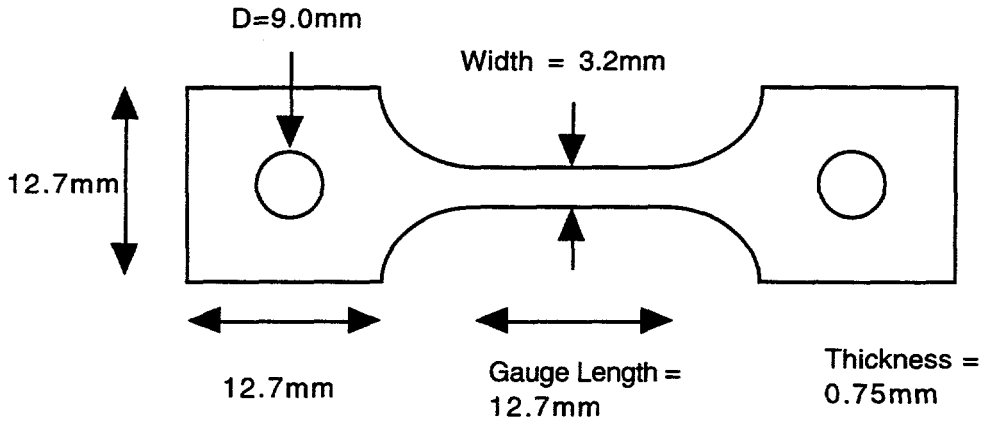

(b)

Fig. 3.5 Tensile specimen geometry for alloy FA-129 (a) and FAP-Y (b). Rolling direction ↔.

evaporating mercury into the vacuum system. Instead of evacuating to < 1.3 x 10^{-4} Pa, the chamber was evacuated to approximately 1 Pa using a rotary mechanical pump.

3.4 Microscopy

3.4.1 Scanning Electron Microscopy

After failure, the fracture surfaces of fatigue crack growth specimens were examined in an AMR-1000 scanning electron microscope (SEM) and the fracture mode (cleavage, transgranular dimples, intergranular, striations, etc.) noted. The fracture surfaces were cut off the rest of the failed specimen on a cut-off wheel, and mounted on an aluminum SEM mount using cement. A carbon-based paint was used to paint over the CT specimen-mount junction to ensure electrical conductivity and eliminate difficulties with specimen charging. The SEM was used with a working distance of 12 mm and an accelerating voltage of 20 kV. All SEM photographs were taken with Polaroid no. 55 film.

3.4.2 Transmission Electron Microscopy

FA-129 and FAP-Y compact tension specimens tested in fatigue crack growth experiments were analyzed by transmission electron microscopy to characterize the microstructure and dislocation structure of these specimens, and to compare changes when tested in fatigue in various environments. Chemical analysis of precipitates was performed using an EDAX analysis system.

TEM thin foils were prepared and examined on a 300 kV Phillips TEM. The foils were cut from the fatigued regions of specimens of both B2 and DO_3 ordered conditions tested in a variety of environments. Foils far from the fatigue zone and from untested material also were prepared as control specimens.

The foils were prepared by slicing off a thin section of the fracture surface on a diamond-blade cutoff wheel or wire-slurry saw. The fracture surface was carefully ground on a slowly revolving polishing wheel with 240 grit paper as far as required to create a smooth surface, typically 0.2 - 0.4 mm. The opposite face was then ground in a similar manner until the total thickness was approximately 0.3 mm. The circular foils were then removed by cutting out 3.0 mm diameter disks with a slurry disk drill. These disks were mechanically ground on both sides with 400 and 600 grit paper, until a thickness of 150 μm was reached. All TEM foils were cut as close to the crack plane as possible, but due to the need to smooth out the rough surface prior to electropolishing these foils, the average distance from the foil center to the crack plane was approximately 125μm. The disks were then electropolished to perforate them using a Ficshione jet-polisher. The electrolytic solution consisted of 6% perchloric acid in methanol. The jet-polishing parameters were as follows: 100 mA current, -20°C temperature, and 30-60 seconds of polishing time. All TEM photographs were taken using Kodak Ectar high density electron microscope film.

3.5 Hardness Measurements

The micro-hardness of each alloy was measured using a LECO R-600 hardness tester for each of the plate orientations: short transverse, long transverse, and longitudinal. Specimens were mounted and polished as described above before being tested. The hardness is reported on the Rockwell A scale. Vickers hot hardness measurements were performed on alloy FA-129 at temperatures from 25°C to 900°C. The hot hardness tests were performed at the Los Alamos National Laboratory.

Vickers hardness measurements were taken on compact tension specimens after fatiguing using a LECO M-400 hardness tester to determine if plasticity or other aging effects were strain hardening the material during testing.

4 RESULTS

4.1 Grain Structure

The 1 hour, 700°C anneal used for alloy FA-129 resulted in an increase in recrystallization from 20% in the as received condition to approximately 50%. As discussed in chapter 2, the grain structure is intentionally left partially unrecrystallized because this condition was found by researchers at the Oak Ridge national Laboratory to provide for the best ductility in the material. The 500°C, 4 day anneal used to create a DO_3 ordered lattice had no effect on degree of recrystallization or grain size. Fig. 4.1a shows the grain structure of as received FA-129. Figs. 4.1b and 4.1c show the longitudinal plane of B2 and DO_3 ordered FA-129 respectively, after annealing. Large precipitates (up to 5 μm) were seen throughout the FA-129 material. They were scattered in non-homogeneous clusters and tended to segregate at grain boundaries as seen in Fig. 4.1d. Annealing FA-129 at 900°C anneal resulted in a nearly fully recrystallized material as seen in Fig. 4.2.

The 1 hour, 800°C anneal used for FAP-Y resulted in a nearly fully recrystallized grain structure with a grain size of 42 μm. Fig. 4.3a shows the grain structure of as-received FAP-Y, and Fig. 4.3b shows the grain structure of FAP-Y after annealing. The grain structure of both FA-129 and FAP-Y retained some of the grain alignment imparted by the rolling process. The rolling direction is still clearly visible in FA-129 (Fig. 4.1b and 4.1c) and FAP-Y (Fig. 4.3b). Alloy Fe-35Al was completely recrystallized by the 800°C anneal. The grain structure of as-received Fe-35Al is shown in Fig. 4.4a, and that of annealed Fe-35Al in Fig. 4.4b. There is evidence of mechanical twin boundaries in the as received Fe-35Al caused by the rolling process (Fig. 4.4a) Note also that in this alloy there is no

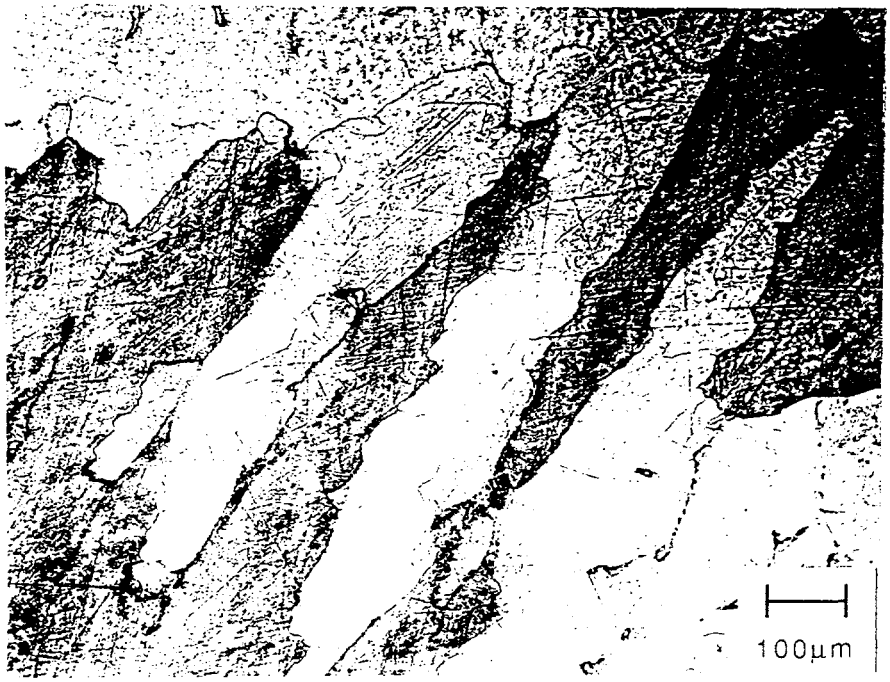

(a)

(b)

Fig. 4.1 Grain structure in the longitudinal plane of as received FA-129 (a) and B2 ordered FA-129 (b). Rolling direction ↔

(c)

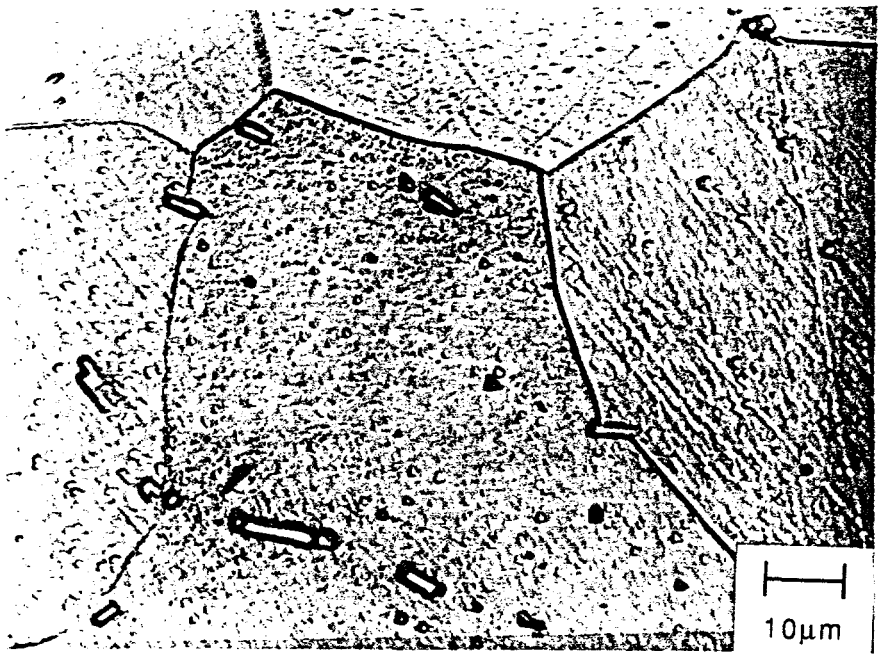

(d)

Fig. 4.1 continued Grain structure in the longitudinal plane of DO_3 ordered FA-129 (c), and B2 ordered FA-129 showing precipitates (d).

Fig. 4.2 Grain structure of B2 ordered FA-129 utilizing a 900°C + 700°C anneal. Rolling direction ↔

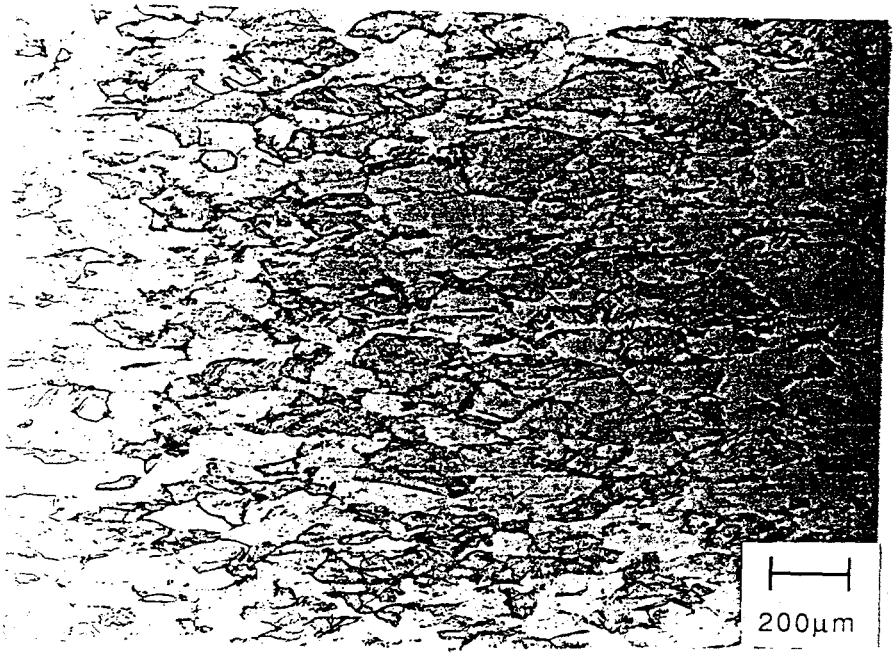

(a)

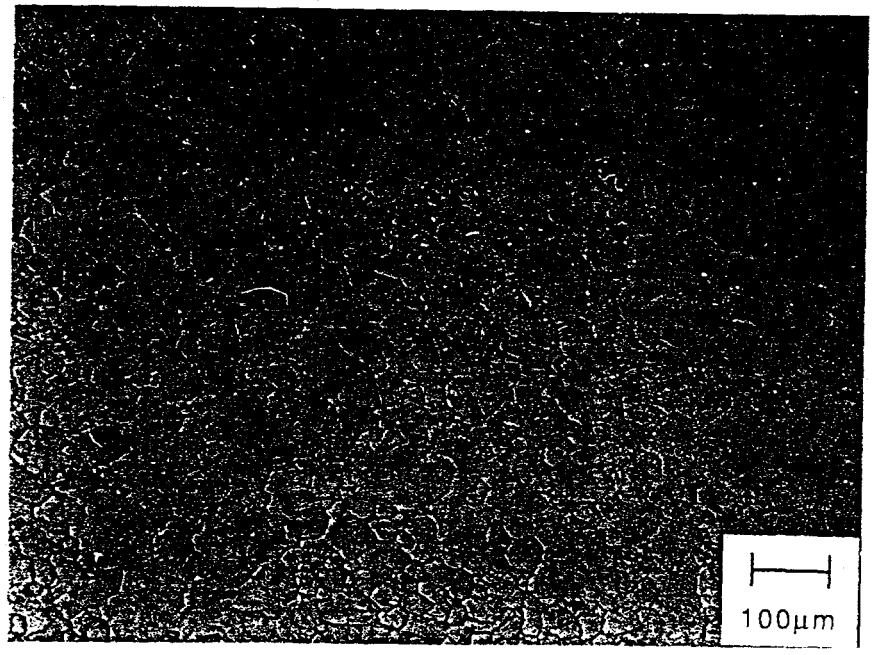

(b)

Fig. 4.3 Grain structure in the longitudinal plane of as received FAP-Y (a) and annealed FAP-Y (b). Rolling direction ↔

(a)

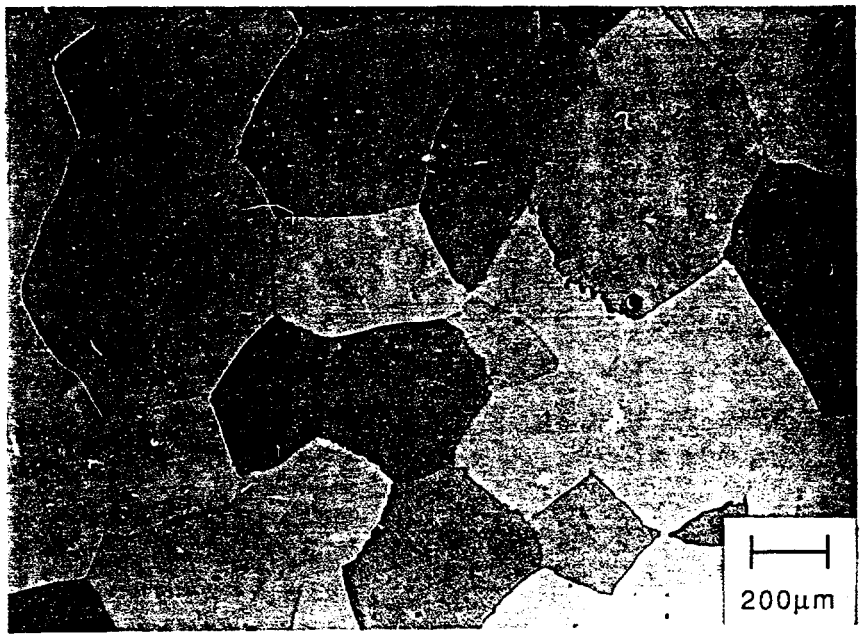

(b)

Fig. 4.4 Grain structure in the longitudinal direction of as received Fe-35Al, with arrows indicating twin boundaries (a) and annealed Fe-35Al (b). Rolling direction ↔

directional aspect to the grains, such as occurs in the lower aluminum alloy, and that the grain size of Fe-35Al was much larger than in FA-129 or FAP-Y (385μm compared to 42μm).

4.2 Hardness

The Rockwell A hardness values for the iron aluminides are listed in Table 2. There was only a small variation in hardness among the alloys, and nearly no variation with hardness on the longitudinal, short, and long transverse planes. Alloy Fe-35Al was the hardest, at 63.5. A shift from B2 to DO_3 order in FA-129 caused only a slight increase in hardness, from 58.5 to 59.5. Alloy FAP-Y was the softest at 57.5.

The Vickers hot hardness results for alloy FA-129 are shown in Fig. 4.5. The hardness is seen to drop quickly as temperatures exceed the critical ordering temperature of approximately 550°C, which corresponds to the B2-DO_3 T_C.

TABLE 2
Rockwell A Hardness Measurements of Iron Aluminides

Alloy	Order	Rolling Plane	Hardness Rockwell A
FAP-Y	-	ST	57.3
FAP-Y	-	LT	57.6
FAP-Y	-	Longitudinal	57.7
FA-129	B2	ST	58.5
FA1-29	B2	LT.	58.7
FA-129	B2	Longitudinal	58.4
FA-129	DO_3	ST	59.6
FA-129	DO_3	LT	59.6
FA-129	DO_3	Longitudinal	59.6
Fe-35Al	DO_3	ST	62.4
Fe-35Al	DO_3	LT	63.7
Fe-35Al	DO_3	Longitudinal	63.5

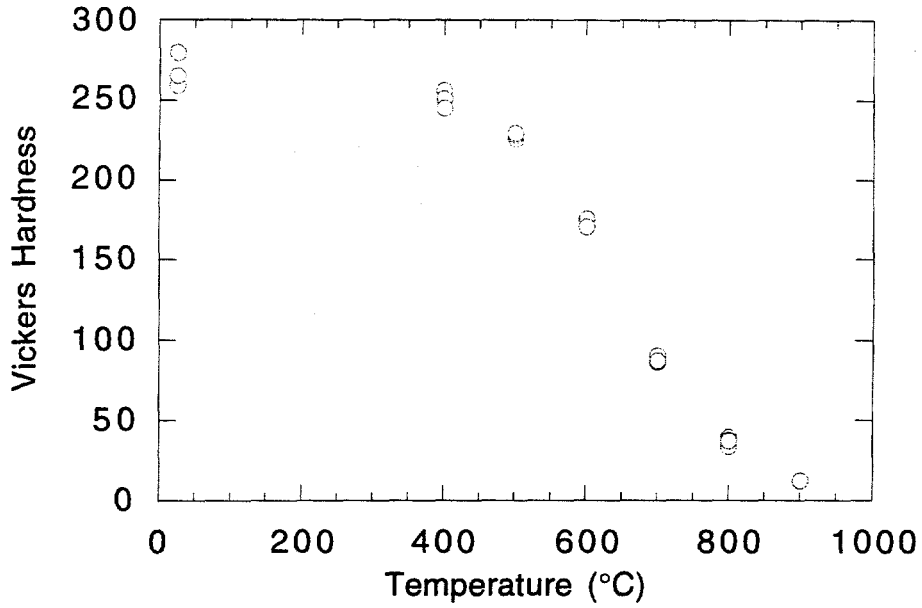

Fig. 4.5 Vickers hot hardness measurements of alloy FA-129.

4.3 Tensile Tests

4.3.1 Tensile properties of FAP-Y

The tensile stress-strain curves for alloy FAP-Y tested at 25°C in hydrogen gas, air, and oxygen are shown in Fig 4.6, and the RA, YS, and UTS are summarized in Table 3. Alloy FAP-Y exhibits significant ductility, as evidenced by the reduction in area (RA), in the inert oxygen atmosphere (RA=57.4%), as well as in air (RA=57.5%). However, FAP-Y is extremely embrittled by hydrogen, which reduces the RA to 3.6%. As is typical in environmental embrittlement, the YS is not significantly affected by environment, and remains between 484-498 MPa in the three environments (Table 3). The UTS is approximately the same in oxygen and air, 653 and 665 MPa, respectively. In the embrittling hydrogen gas, the UTS is decreased to 614 MPa. The decrease in UTS when testing in hydrogen gas is small (6.3% decrease between oxygen and hydrogen environments) compared to the decrease in RA (94% decrease between oxygen and hydrogen environments). This is due to the low strain-hardening rate of the disordered FAP-Y alloy, as seen in the stress-strain curves of Fig. 4.6.

Fractography of the FAP-Y tensile samples are shown in Figs. 4.7(a-c) for oxygen, air, and hydrogen gas, respectively. The change in fracture mode with environment is consistent with the changes in RA. In both oxygen (Fig. 4.7a) and air (Fig. 4.7b), the fracture surface was predominantly transgranular cleavage, with a large amount of ductile dimpling. A small amount of longitudinal cracking was also observed. In hydrogen gas, there was no evidence of dimpling and a significant amount of longitudinal cracking occurred (Fig. 4.7c)

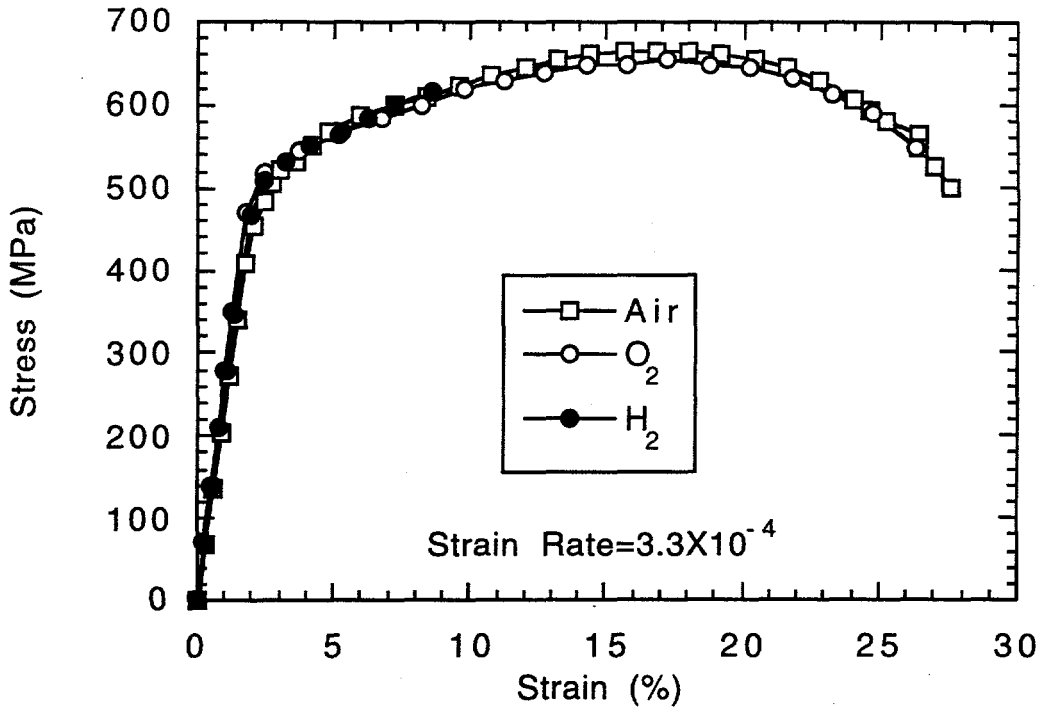

Fig. 4.6 Stress-Strain curves for alloy FAP-Y tested in tension at room temperature.

TABLE 3
Tensile Properties of Alloy FAP-Y at 25°C

Environment	RA(%)	YS (MPa)	UTS (MPa)
Hydrogen	3.6	484	614
Air	57.5	487	665
Oxygen	57.4	498	653

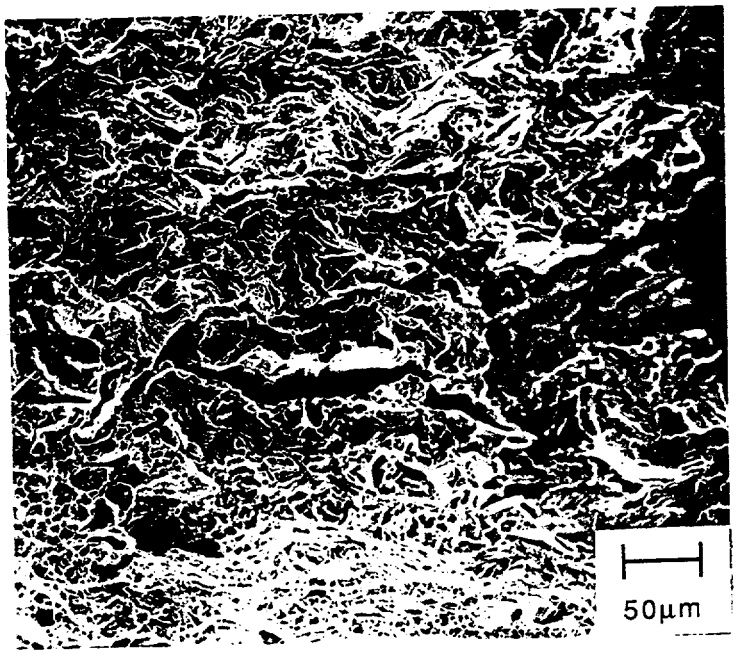

(a)

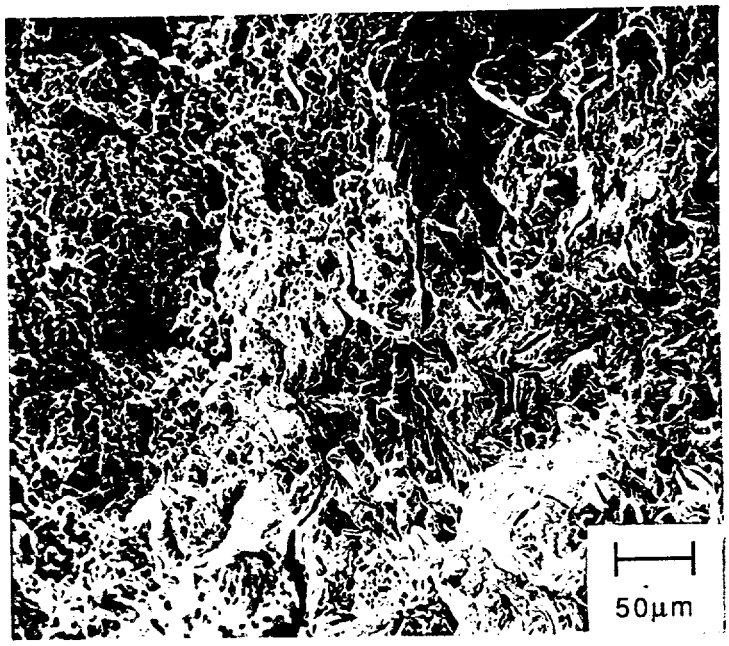

(b)

Fig. 4.7 Fracture surface of FAP-Y tested in tension in oxygen (a) and air (b) at 25°C.

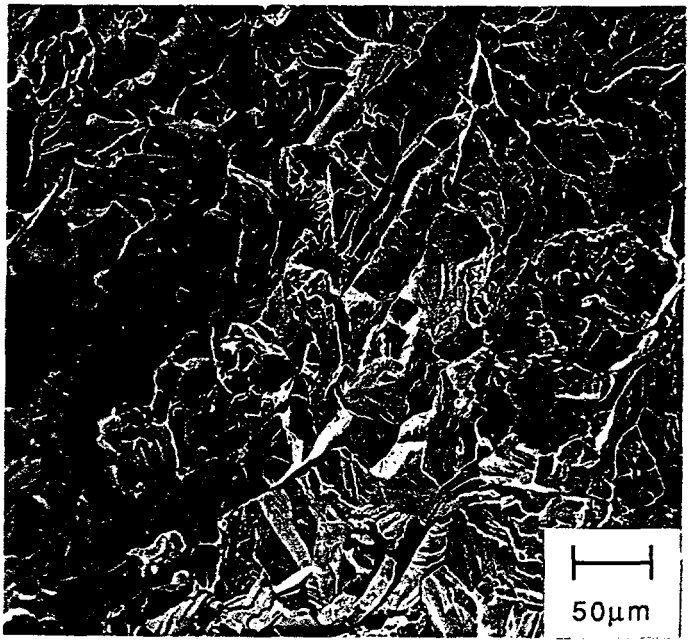

Fig. 4.7 continued Fracture surface of FAP-Y tested in tension in hydrogen gas at 25°C (c).

4.3.2 Tensile Properties of FA-129

The stress-stain curves for all tensile tests on alloy FA-129 are shown in Appendix B, figures B1-B7.

Fig. 4.8 shows the variation of RA in B2 ordered FA-129 with temperature and environment. The corresponding YS and UTS are shown in Fig. 4.9. The tensile properties of DO_3 ordered FA-129 are shown in Figs. 4.10 and 4.11. These tensile properties are summarized in Table 4. The stress-strain curves of test can be found in Appendix B.

The RA and UTS are greatly reduced at 25°C for both B2 (Figs. 4.8 and 4.9) and DO_3 (Figs. 4.10 and 4.11) ordered FA-129 by testing in air compared to testing in oxygen. Both alloys show a similar degree of embrittlement in air. In the B2 state, RA in oxygen (14.5%) is reduced by nearly one-fourth when tested in air (10.8%), and in the DO_3 state, RA decreases by one-third from 15.7% in oxygen to 10.4% in air. The vacuum environment provided for much better RA in air, but slightly less than that measured in oxygen, as seen in (Table 4).

The UTS in both materials was decreased significantly in the embrittling air, which is typical of materials with high strain hardening rates. A decrease of 21% was noted in the UTS for B2 ordered FA-129 between the oxygen (858 MPa) environment and air (677 MPa). The decrease in UTS in the DO_3 ordered material was double, 40%, between the oxygen environment (904 MPa) and air (645 MPa). The UTS of DO_3 ordered FA-129 is more sensitive to environment because the strain hardening rate is much greater than in B2 ordered FA-129.

The yield stress was not significantly affected by environment, except for DO_3 ordered FA-129 in air (Table 4), where it decreased by 15% compared to the oxygen and vacuum

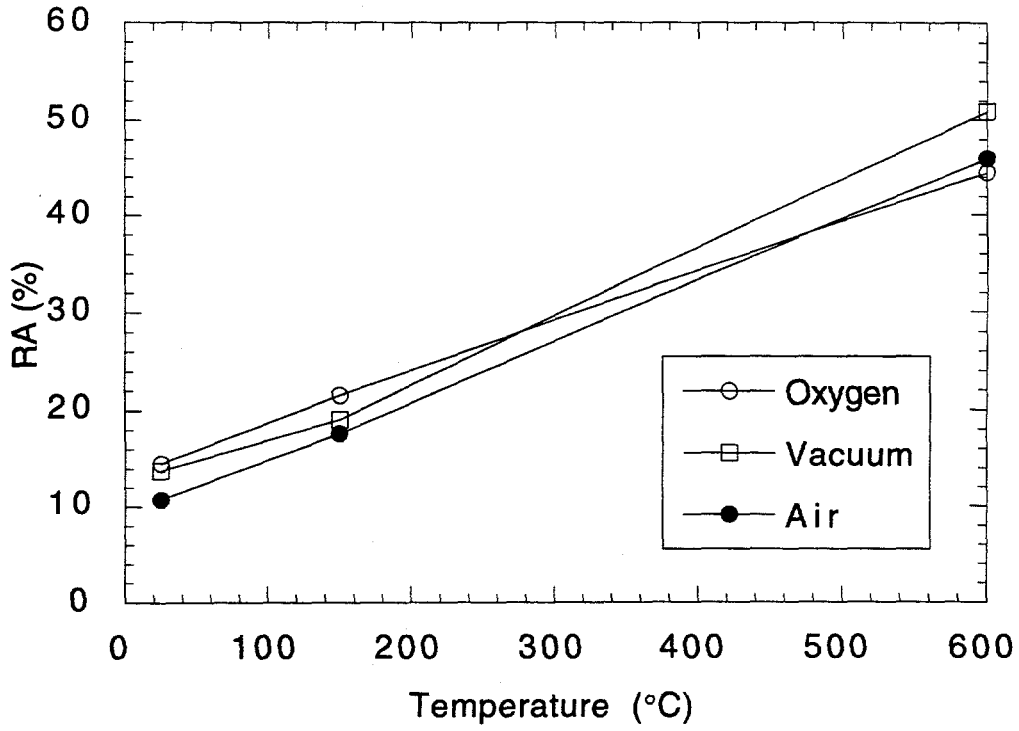

Fig. 4.8 Reduction in Area of B2 ordered FA-129 tested in tension.

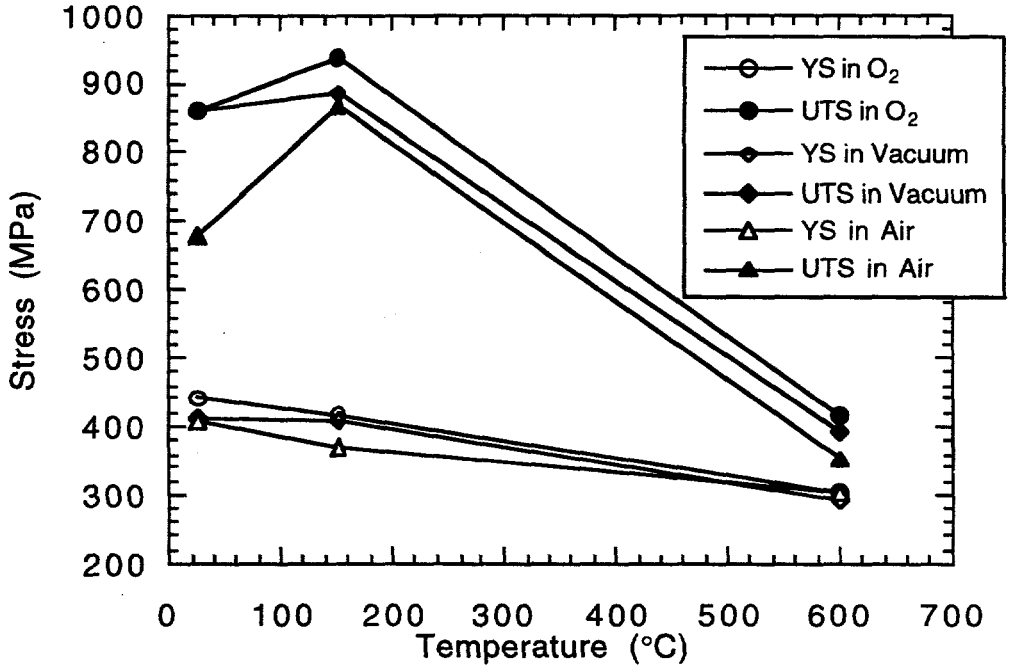

Fig. 4.9 YS and UTS of B2 ordered FA-129 tested in tension.

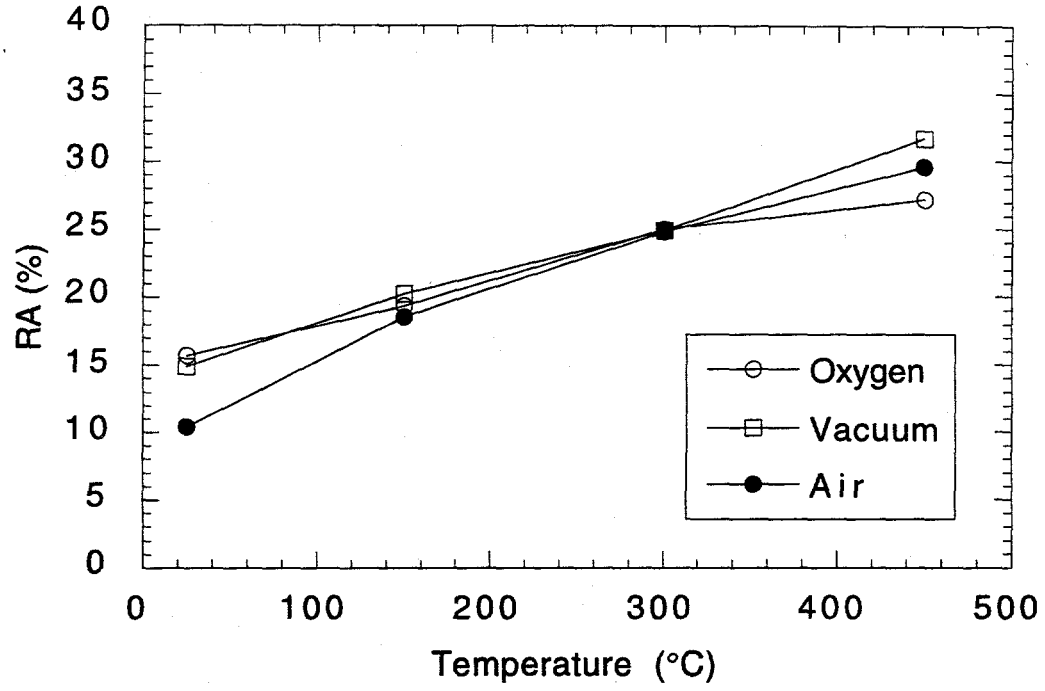

Fig. 4.10 Reduction in Area of DO_3 ordered FA-129 tested in tension.

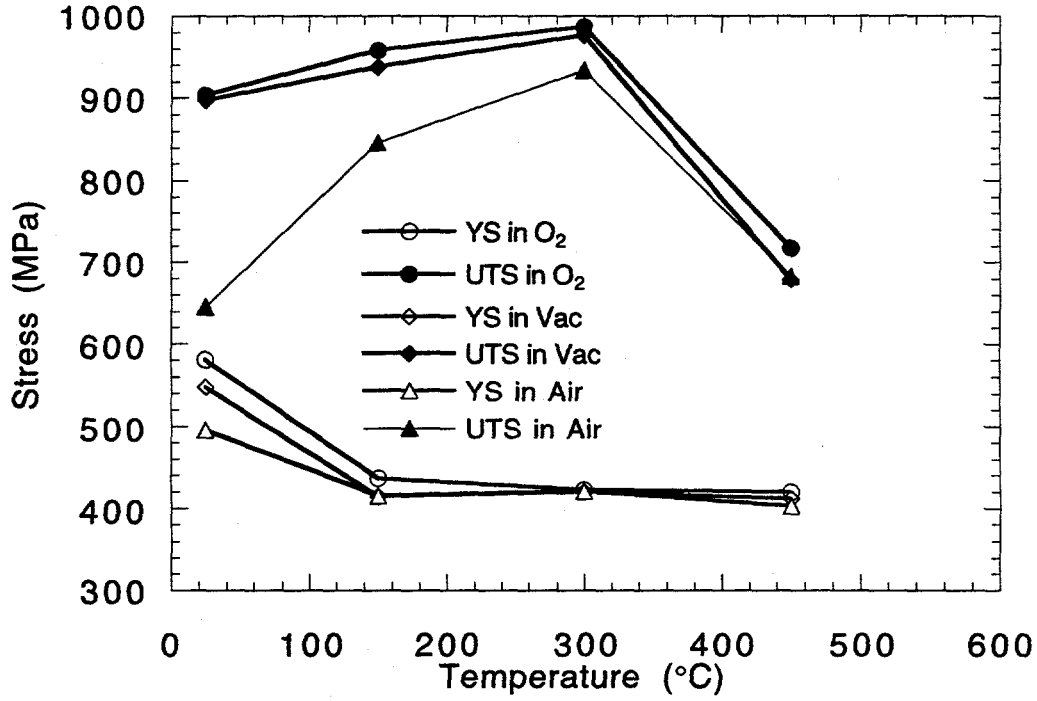

Fig. 4.11 YS and UTS in DO_3 ordered FA-129 tested in tension.

TABLE 4
Tensile Data for FA-129

		Air			Vac			O_2		
Order	Temp (°C)	RA (%)	YS (MPa)	UTS (MPa)	RA (%)	YS (MPa)	UTS (MPa)	RA (%)	YS (MPa)	UTS (MPa)
B2	25	10.8	409	677	13.8	412	859	14.5	440	858
	150	17.6	369	865	19.0	409	885	21.5	417	936
	600	46.0	303	351	50.9	293	392	44.5	306	416
DO_3	25	10.4	495	645	14.9	547	897	15.7	580	904
	150	18.5	415	846	20.2	414	938	19.3	436	958
	300	24.8	421	934	24.9	420	977	25.0	423	987
	450	29.6	403	683	31.7	412	679	27.2	420	717

environments. The YS in the DO_3 state was higher in each environment at 25°C (averaging 540 MPa), than in the B2 state (averaging 420 MPa).

At 150°C, the RA of both B2 and DO_3 ordered FA-129 increased (Table 4) in all environments. Again, oxygen provided for the highest RA, followed by vacuum and air. However, the spread between the RA measured in each environment decreased.

A similar effect was seen in the UTS of both B2 and DO_3 ordered FA-129. However, the YS of B2 ordered FA-129 was not significantly affected by the increase in temperature to 150°C, while the YS of DO_3 ordered FA-129 was decreased significantly at 150°C. These results indicates that the main effect of increasing temperature to 150°C on B2 ordered FA-129 is to reduce the embrittling effects of air, while in DO_3 ordered FA-129 there is both a decrease in embrittlement and a change in the deformation mechanism and dislocation structure.

As temperature is increased further to 300°C in DO_3 ordered FA-129 the RA is found to be nearly the same in all three environments (25.0 - 24.8%), and higher than at 150°C for each environment, indicating no hydrogen embrittlement. This temperature corresponds also to a peak in UTS (Fig. 4.11). No further significant changes in YS were noted at temperatures above 150°C.

At 450°C, the RA of DO_3 ordered FA-129 is again higher than at 300°C, with vacuum providing the highest RA, followed by air and oxygen. This effect of environment is different from that noted at 25°C and 150°C. At elevated temperature it is possible that oxygen embrittlement is occurring. This would explain the effect of environment on RA, as the RA decreases as amount of oxygen available increases (most available O_2 and lowest RA in pure O_2, followed by air, and lowest available O_2 and highest RA in vacuum). The UTS decreases sharply at 450°C, but there is little effect of environment (Fig. 4.11).

At 600°C, B2 ordered FA-129 exhibits very high RA, 50.9% in vacuum, 46.0% in air, and 44.5% in oxygen. As with the DO_3 ordered FA-129 at 450°C, the effect of

environment on RA suggests an oxygen embrittlement effect at elevated temperature. The UTS was also greatly reduced compared to values measured at 150°C (Fig. 4.9). The YS measured at 600°C was also much lower than at 150°C, but was unaffected by environment.

In B2 and DO_3 ordered FA-129, there is a change in fracture surface when the environment is changed from air to oxygen at 25°C. Failure mode is predominantly transgranular in air, as seen in Fig. 4.12a for B2 ordered FA-129. The failure mode is mixed transgranular - intergranular in oxygen, as seen in Fig. 4.12b for B2 ordered FA-129. A similar shift in fracture mode is observed in DO_3 ordered FA-129 in air (Fig. 4.13a) and oxygen (Fig. 4.13b).

Fig. 4.14 shows a comparison of the RA measured in the alloys FA-129 and FAP-Y. Alloy FA-129 is clearly more ductile in the B2 ordered condition than in the DO_3 at room temperature. However, at 150°C the RA of these materials becomes comparable (Table 4). FAP-Y exhibits much higher RA than FA-129 in either ordered condition in oxygen. Unlike FA-129, FAP-Y is not embrittled in tensile testing by air. Similar RA's were measured in both air and oxygen (57.5% and 57.4% respectively, Fig. 4.14), but FAP-Y is severely embrittled in hydrogen gas (RA reduced to 3.6%).

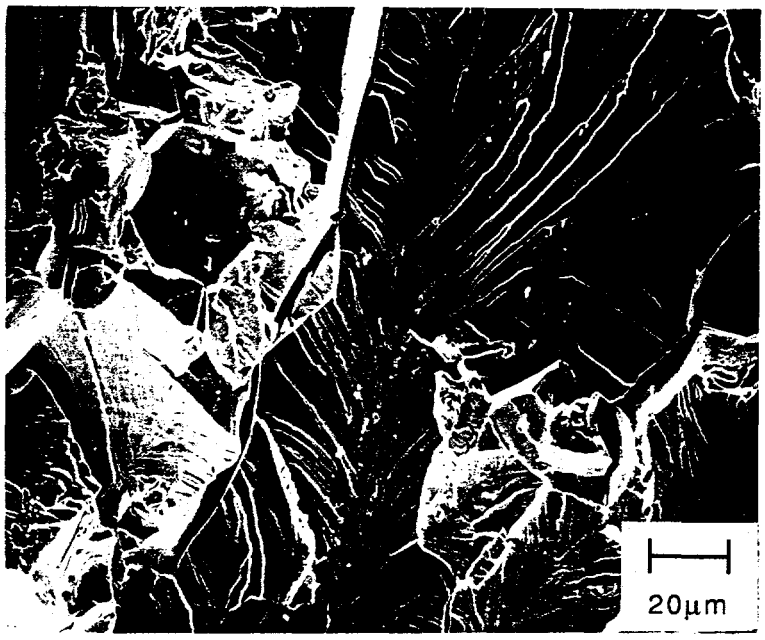

(a)

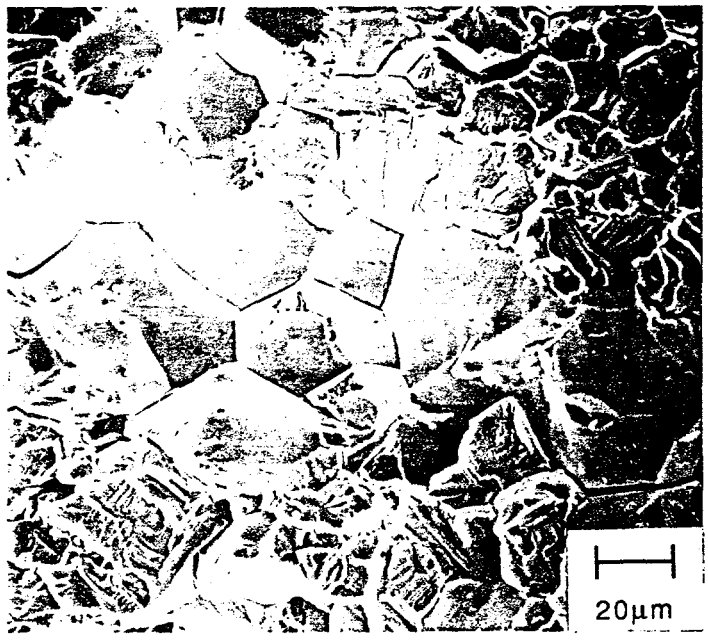

(b)

Fig. 4.12 Fracture surface of B2 ordered FA-129 tested in tension at 25°C in air (a), and in oxygen (b).

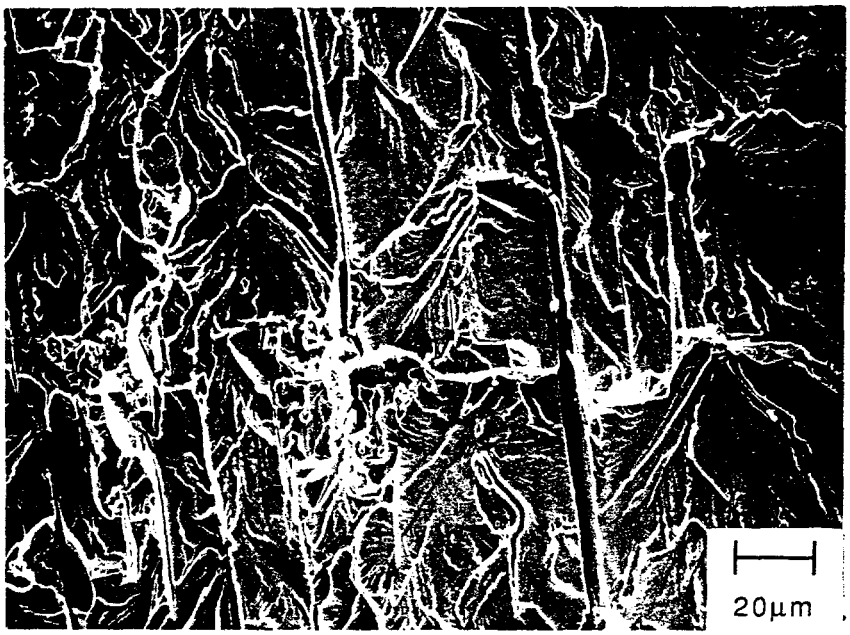

(a)

(b)

Fig. 4.13 Fracture surface of DO_3 ordered FA-129 tested in tension at 25°C in air (a), and in oxygen (b).

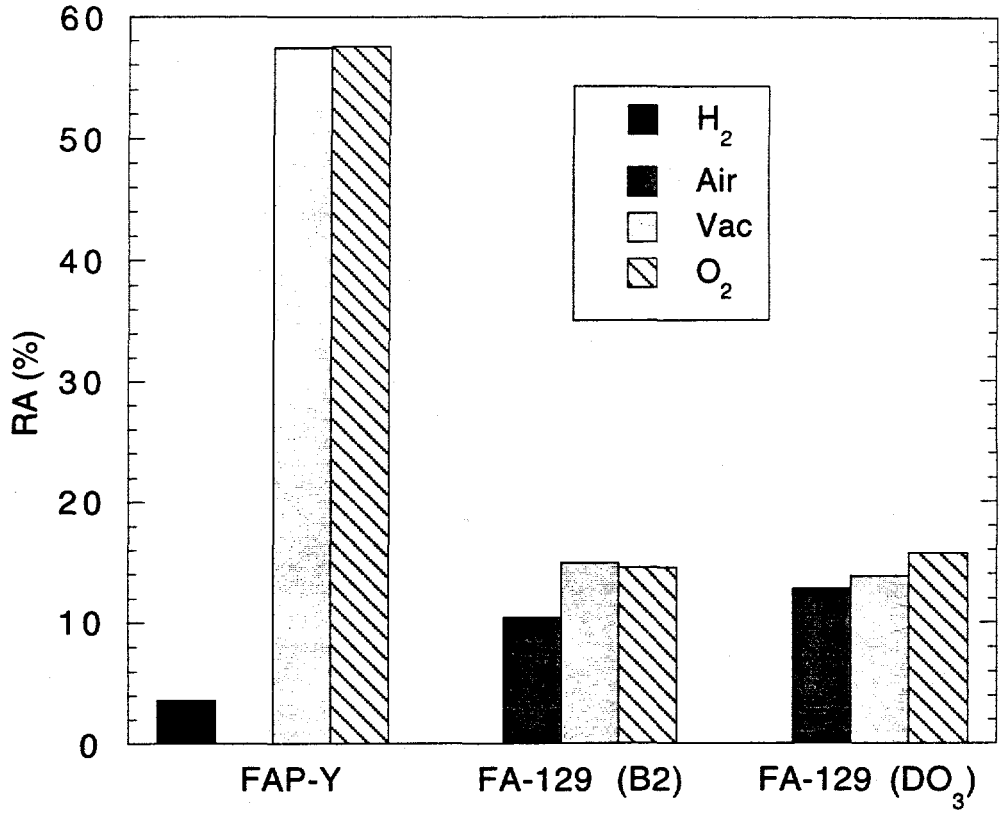

Fig. 4.14 Comparison of tensile reduction in area in FAP-Y and FA-129 at 25°C.

4.4 Fatigue Crack Growth

The threshold and critical stress intensities measured for the iron aluminides are listed in Table 5. Results of a single test are reported for each condition. A linear region of the da/dN vs. ΔK curves for use in calculating the Paris slope, m, of

$$da/dN = C(\Delta K)^m, \qquad \text{Eq. 7}$$

could not always be defined. Therefore, the stress intensity range which resulted in a crack growth rate of 10^{-7}m/cycle was measured, $\Delta K(10^{-7})$, and this value is reported in Table 5 as well. ΔK_{TH} was taken as the stress intensity range which produced a crack growth rate of $5x10^{-9}$ m/cycle, or the stress intensity range extrapolated at $5x10^{-9}$ m/cycle.

4.4.1 Effect of Alloy Composition and Order on Fatigue Crack Growth

FCG curves in oxygen at room temperature for each alloy are shown in Fig. 4.15 (a), and duplicate tests for B2 and DO_3 ordered FA-129 in oxygen are shown in Fig. 4.15 (b) to illustrate the consistency of FCG measurements. The oxygen environment is considered to be the inert reference environment. FCG resistance depends strongly on alloy composition and ordered structure. B2 ordered FA-129 exhibits the best FCG resistance, with a ΔK_{TH} of 20MPa$\sqrt{m}$ and a K_C of 71.8 MPa$\sqrt{m}$. Changing the ordered structure of FA-129 to DO_3 has a dramatic effect on the fatigue response. In the DO_3 state, compared to the B2 state, the critical and threshold stress intensities, as well as the stress intensity to achieve 10^{-7} m/cycle, are reduced by approximately 40%.

TABLE 5
Fatigue Crack Growth Data for Iron Aluminides

Alloy	Environment	$\Delta K(10^{-7})$ (MPa$\sqrt{m}$)	ΔK_{TH} (MPa$\sqrt{m}$)	ΔK_C (MPa$\sqrt{m}$)	K_C
FAP-Y	O_2, 25°C	11.1	10.3	12.8	25.6
FAP-Y	Air, 25°C	10.5	10.0	11.7	23.4
FAP-Y	H_2, 25°C	—	—	—	—
FA-129 (B2)	O_2, 25°C	29.9	20.0	35.9	71.8
FA-129 (B2)	Air, 25°C	23.9	14.5	29.9	59.8
FA-129 (B2)	H_2, 25°C	21.3	13.8	25.9	51.8
FA-129 (DO_3)	O_2, 25°C	19.2	13.5	23.5	47.0
FA-129 (DO_3)	Air, 25°C	16.7	13.3	19.8	39.6
FA-129 (DO_3)	H_2, 25°C	12.2	11.1	17.4	34.8
Fe-35Al (DO_3)	O_2, 25°C	28.6	18.3	32.8	65.6
Fe-35Al (DO_3)	Air, 25°C	24.1	16.3	25.6	51.2
Fe-35Al (DO_3)	H_2, 25°C	15.2	13.4	26.3	52.6
FA-129 (B2)	Air, 150°	35.5	20.4	40.5	81.0
FA-129 (DO_3)	Air, 150°C	33.6	18.5	34.5	69.0
FA-129 (DO_3)	Air, 300°C	—	18.0	33.1	66.2
FA-129 (DO_3)	Air, 450°C	23.8	16.2	31.1	62.2

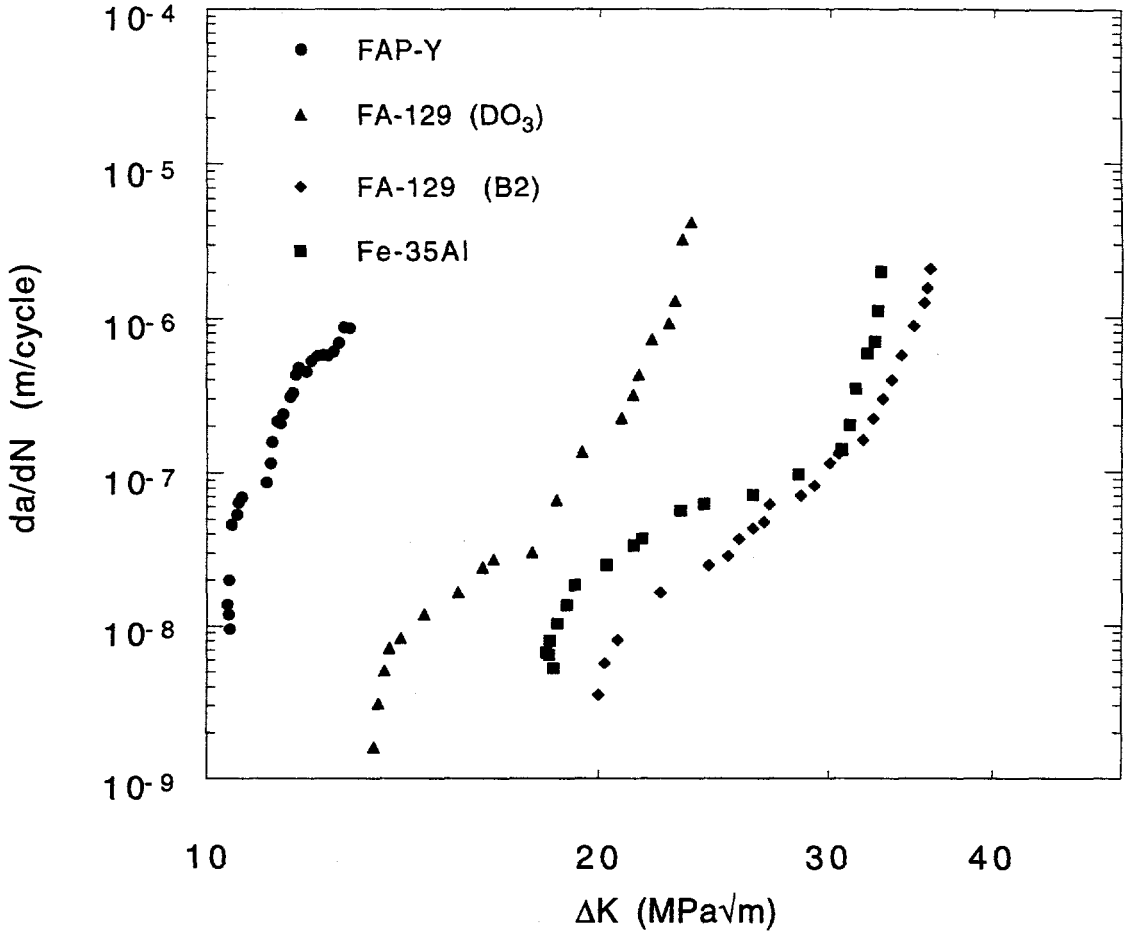

(a)

Fig. 4.15 Comparison of FCG in FAP-Y, DO_3 ordered FA-129, B2 ordered FA-129, and Fe-35Al in oxygen gas at 25°C. Frequency = 20Hz, R=0.5. (a)

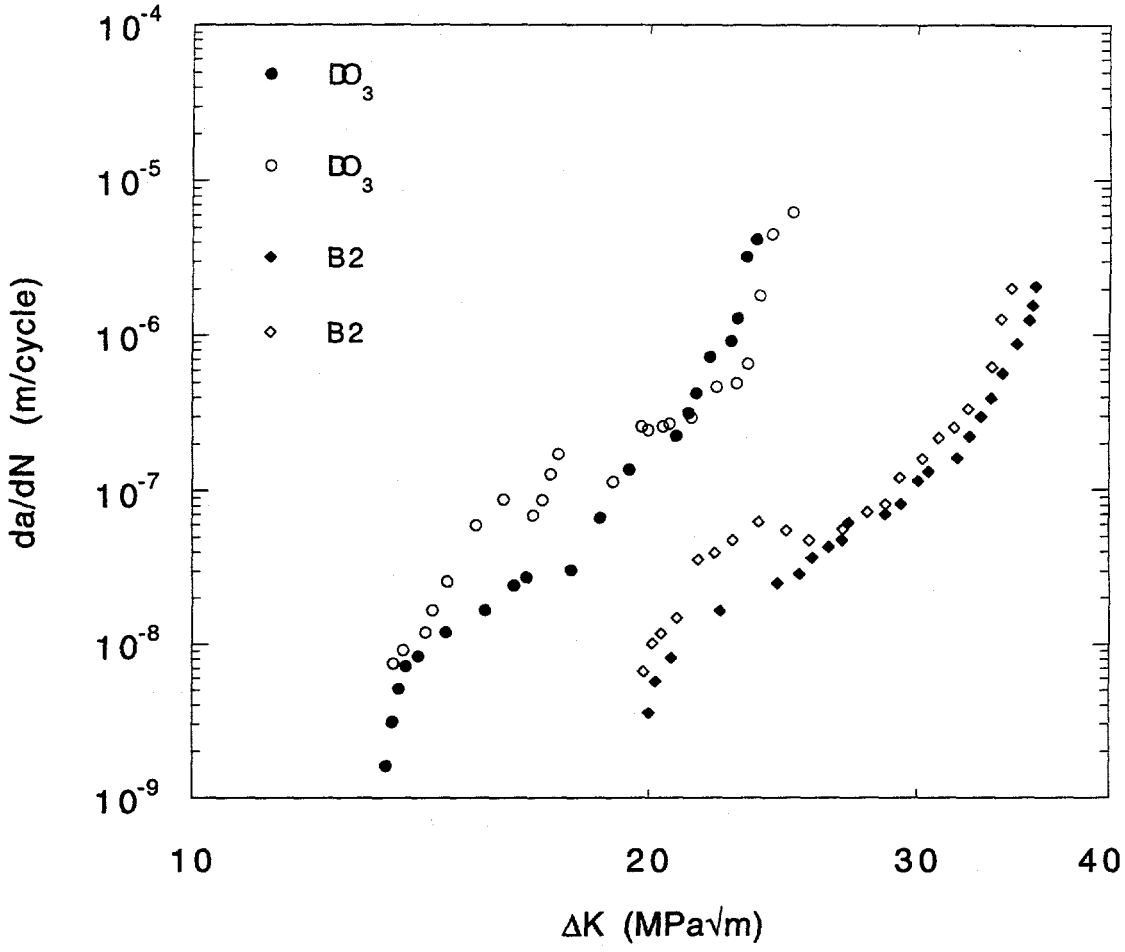

(b)

Fig. 4.15 continued — Duplicate fatigue crack growth tests in B2 and DO_3 ordered FA-129 performed in oxygen at 25°C. Frequency = 20Hz, R=0.5. (b)

The higher aluminum Fe-35Al exhibits FCG behavior similar to that of the B2 ordered FA-129. The disordered alloy FAP-Y, however, exhibits extremely poor FCG resistance compared to FA-129 and Fe-35Al. The threshold and critical stress intensities measured in FAP-Y in air (ΔK_{TH} = 10.3 MPa$\sqrt{m}$ and K_C = 25.6 MPa$\sqrt{m}$) were less than half those measured for B2 ordered FA-129.

When the fatigue crack growth curves were normalized for elastic modulus by plotting da/dN vs. $\Delta K/E$, the effect of alloy composition was decreased slightly. The elastic modulus of FA-129 is 207 GPa, while that of FAP-Y is 175 GPa (86). However, the fatigue crack growth resistance of alloy FAP-Y is still less than that of B2 or DO_3 ordered FA-129.

4.4.2 Effect of Environment on Fatigue Crack Growth

The fatigue crack growth curves at room temperature in the three environments (hydrogen gas, laboratory air, and oxygen gas) are shown in Fig. 4.16 for Fe-35Al, Fig. 4.17 for FA-129, and Fig. 4.18 for FAP-Y. Note that fatigue tests in only air and oxygen are shown in Fig. 4.18. Stable crack growth was not achieved in alloy FAP-Y in hydrogen gas and da/dN vs. ΔK data in hydrogen gas could not be measured. Table 5 and Figs. 4.16-4.18 show that hydrogen gas is clearly an embrittling environment for FCG. In FA-129 and Fe-35Al, ΔK_{TH}, $\Delta K(10^{-7})$, and K_C are lower in hydrogen gas than in oxygen. Alloy FAP-Y was so sensitive to the hydrogen gas that stable crack growth could not be achieved with the specimen geometry used.

Testing in laboratory air proved to be embrittling for all alloys as well. However, the degree of embrittlement in air was less than that in hydrogen gas. In B2 ordered FA-129, for example, hydrogen reduces ΔK_{TH} and K_C by 31% and 28%, respectively, as compared

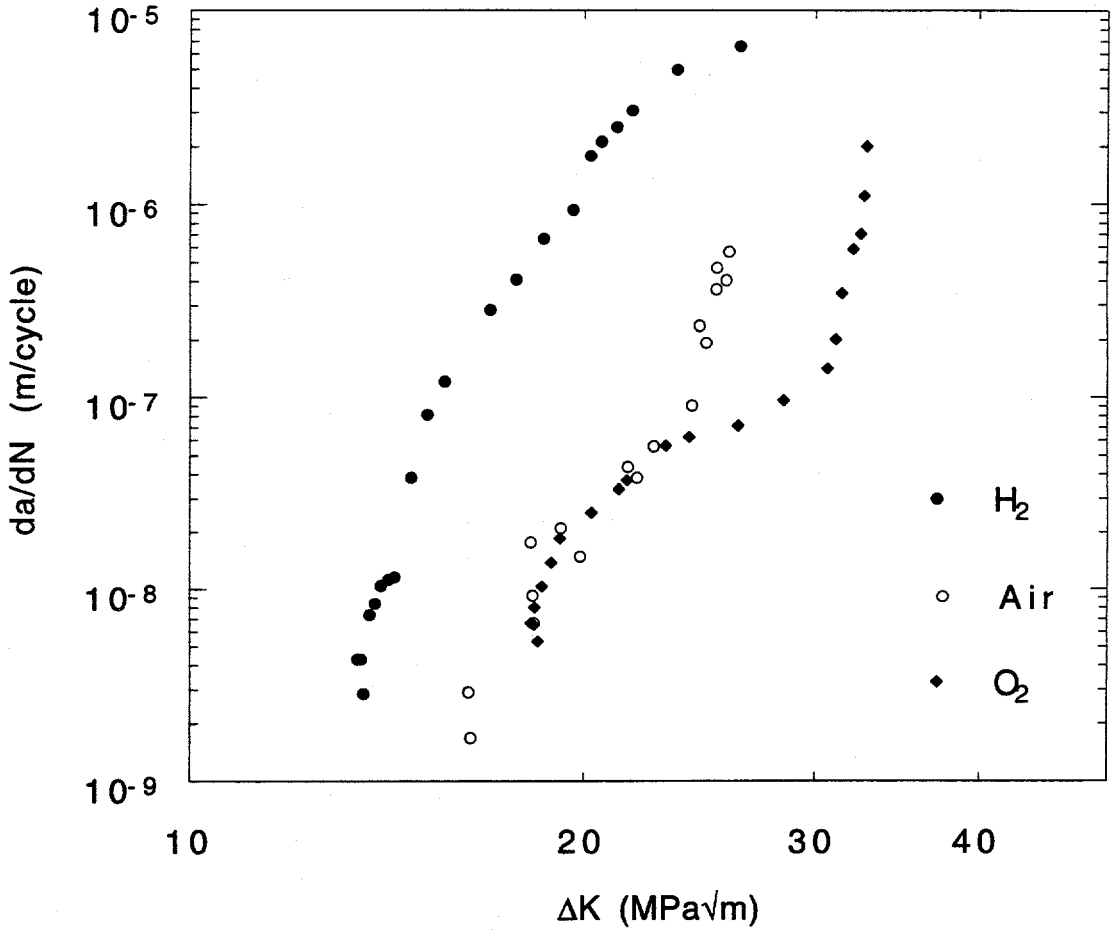

Fig. 4.16 Fatigue crack growth curves for Fe-35Al at 25°C. Frequency = 20Hz, R=0.5.

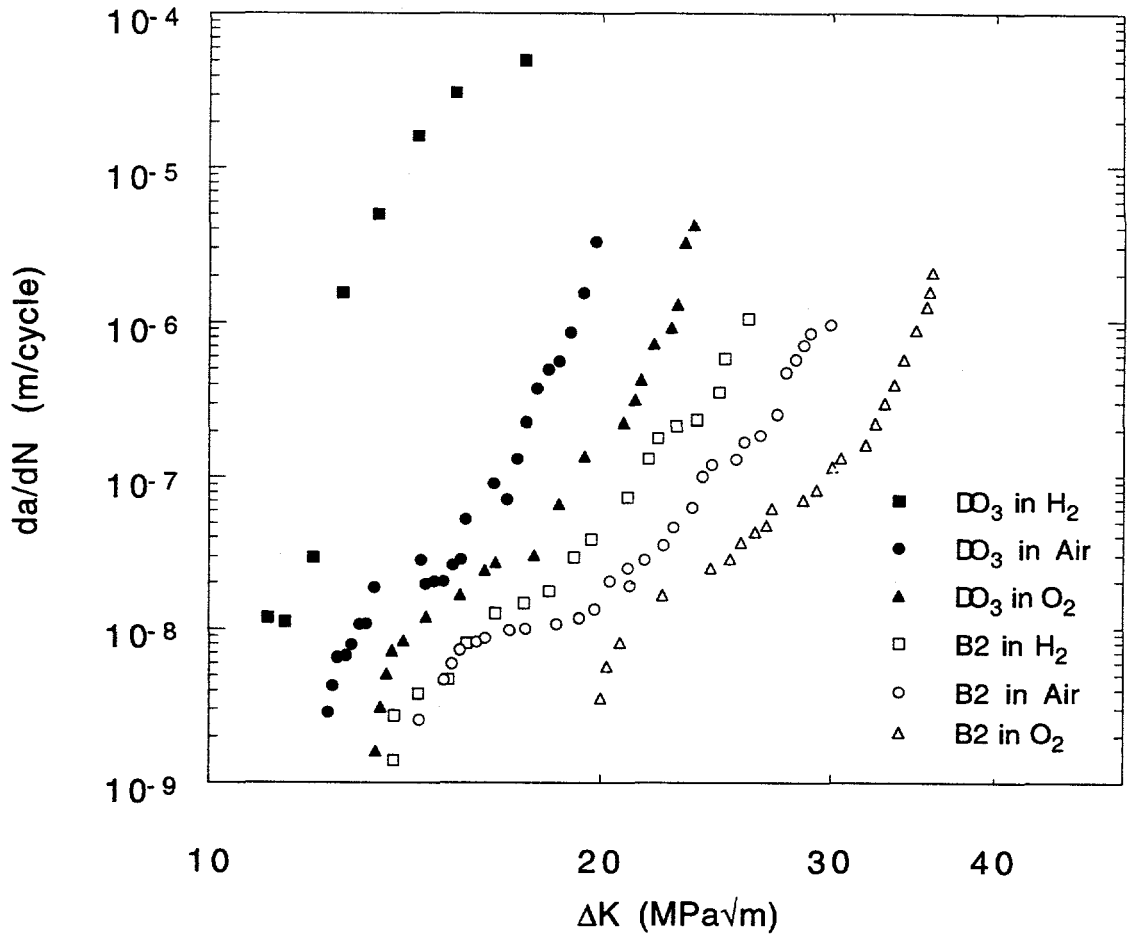

Fig. 4.17 Fatigue crack growth curves for B2 and DO_3 ordered FA-129 at 25°C. Frequency = 20Hz, R=0.5.

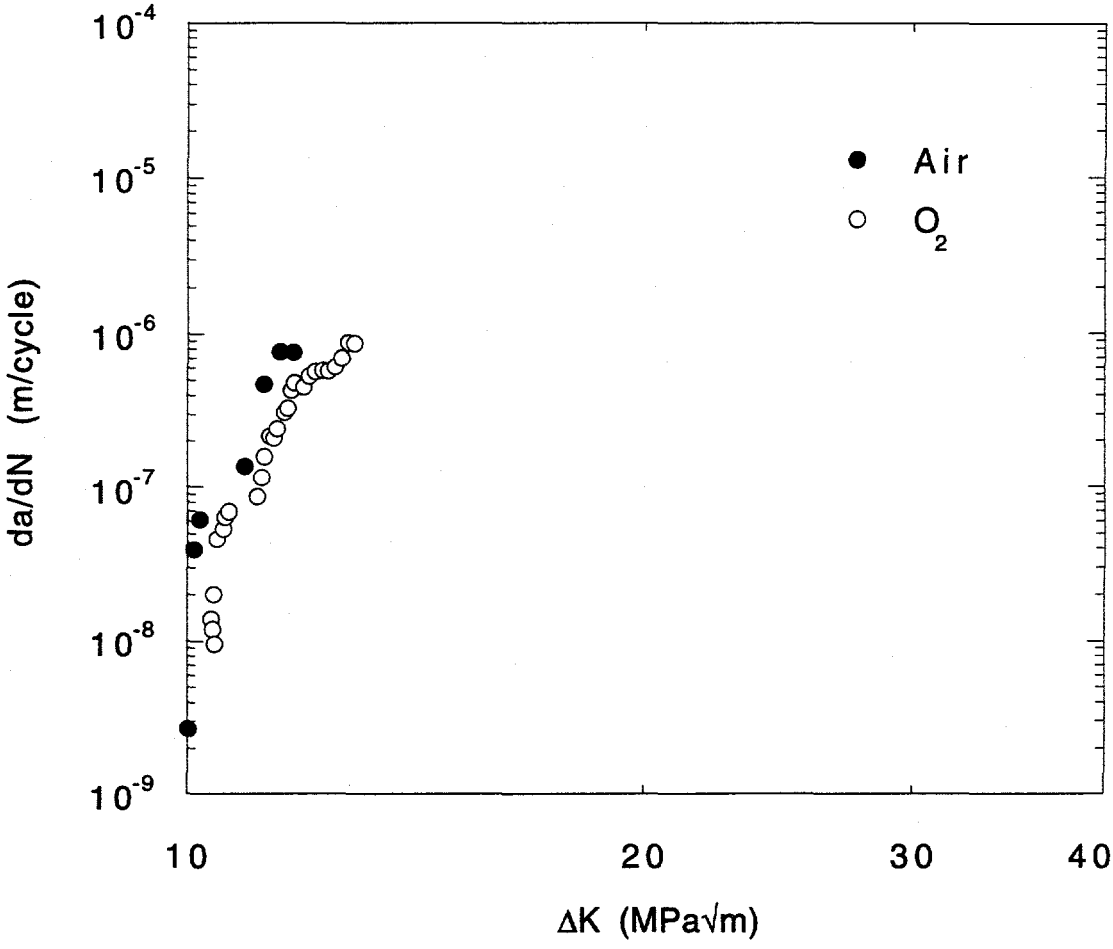

Fig. 4.18 Fatigue crack growth curves for FAP-Y at 25°C. Frequency = 20Hz, R=0.5. Stable crack growth in hydrogen gas was not achieved.

to oxygen. Testing in laboratory air, however reduces ΔK_{TH} by 27% while K_C is reduced by only 17%. A similar result is seen in the other alloys tested as well.

The degree of embrittlement in air was similar for the ordered FA-129 and Fe-35Al alloys, with the decrease in K_C being approximately 20%. However, alloy FAP-Y appeared to suffer less severe embrittlement in air and than the other alloys. The decrease in K_C in air, compared to in oxygen, of 8.5% was much smaller than in B2 (16%) or DO_3 (21%) ordered FA-129, and Fe-35Al (22%), indicating that FAP-Y is less susceptible to moisture-induced embrittlement. However, the fact that stable crack growth could not be achieved in FAP-Y indicates that it is extremely susceptible to hydrogen gas embrittlement.

A summary of ΔK_{TH} and K_C for each alloy in hydrogen gas, air, and oxygen gas at 25°C is shown in Figs. 4.19 and 4.20. Note that even in oxygen, which was the most favorable condition, the FCG resistance of DO_3 ordered FA-129 was worse than that of B2 ordered FA-129 in the aggressive hydrogen environment. $\Delta K(10^{-7})$ has been tabulated for each test condition in Fig. 4.21.

4.4.3 Effect of Temperature on Fatigue Crack Growth

Elevated temperature fatigue crack growth curves in air for alloy FA-129 are shown in Fig. 4.22 (a) for the B2 ordered condition and Fig. 4.23 (a) for the DO_3 condition. Note that ΔK on these curves has been decreased to account for an error in the experimental set-up. The hydraulic gain on the MTS machine was accidentally set too low and the applied ΔK level was lower than desired. The difference between desired and actual ΔK was constant over the testing range, so the data was shifted left on the ΔK axis to correspond with the actual applied stress intensity.

An increase in temperature to 150°C from 25°C causes a great increase in FCG resistance in air. In the B2 ordered FA-129, ΔK_{TH} increases from 14.5 to 20.4 MPa$\sqrt{m}$

(Table 5), and K_C is increased from 59.8 to 81 MPa$\sqrt{m}$. The stress intensity range required to achieve a crack growth rate of 10^{-7} m/cycle increased from 23.9 to 35.5 MPa$\sqrt{m}$ (Fig. 4.22).

A similar increase in FCG was observed in DO_3 ordered FA-129 fatigued in air at a temperature of 150°C. ΔK_{TH} increased from 13.3 to 18.5 MPa$\sqrt{m}$ (Table 5) and K_C increased from 39.6 to 69.0 MPa$\sqrt{m}$, and the stress intensity range required to achieve a crack growth rate of 10^{-7} m/cycle was 33.6 MPa$\sqrt{m}$ at 150°C compared to 16.7 MPa$\sqrt{m}$ at 25°C.

Increasing temperature further in the DO_3 condition, resulted in a gradual decrease in FCG resistance (Fig. 4.23). DO_3 ordered FA-129 still performed better at 450°C than at 25°C. However, when the fatigue crack growth curves are normalized by dividing the stress intensity range by Young's modulus, the high temperature FCG curves appear to collapse onto a single family of curves in the DO_3 ordered case. The modulus normalized curves are shown in Fig. 4.22b and 4.23b for the B2 and DO_3 ordered material, respectively.

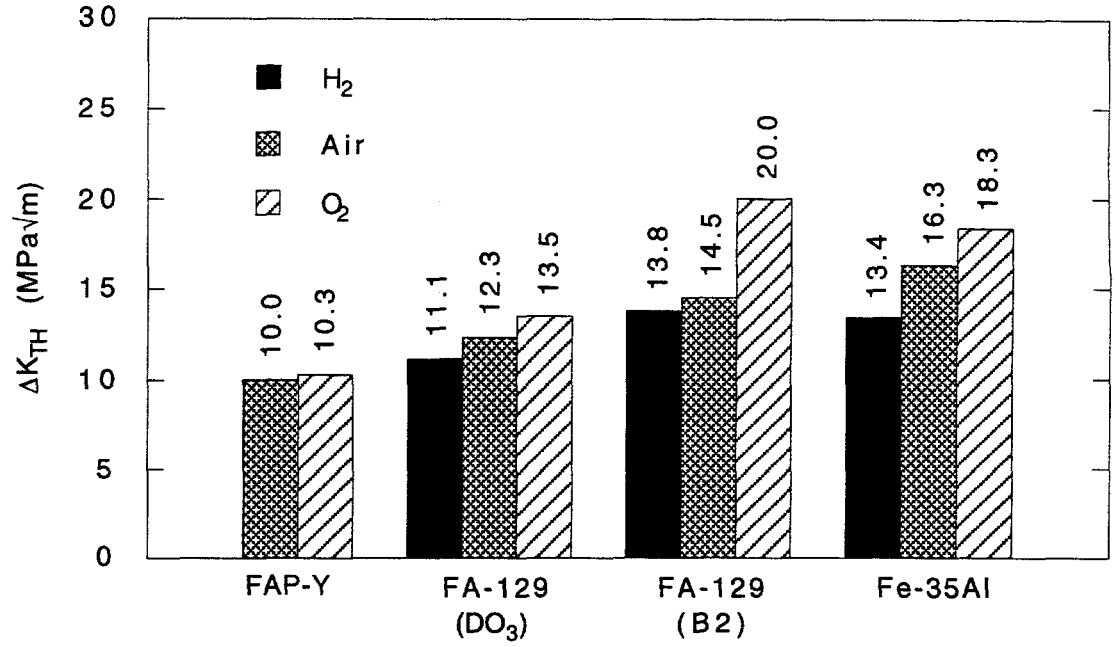

Fig. 4.19 Summary of threshold stress intensities in iron aluminides fatigued at room temperature. Frequency = 20Hz, R=0.5.

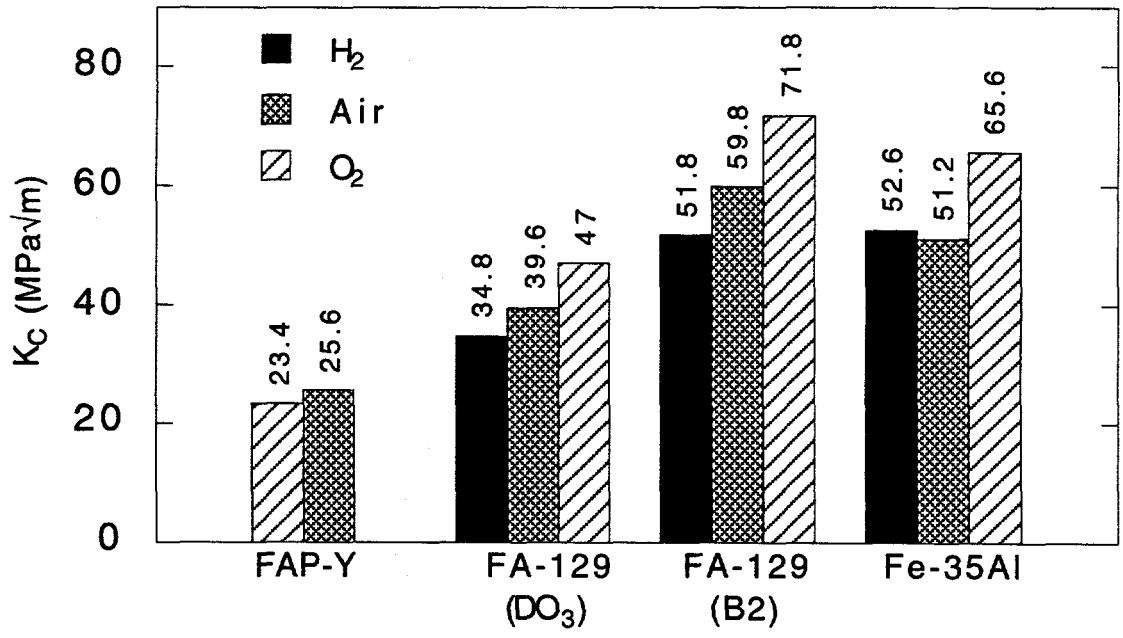

Fig. 4.20 Summary of critical stress intensities in iron aluminides fatigued at room temperature. Frequency = 20Hz, R=0.5.

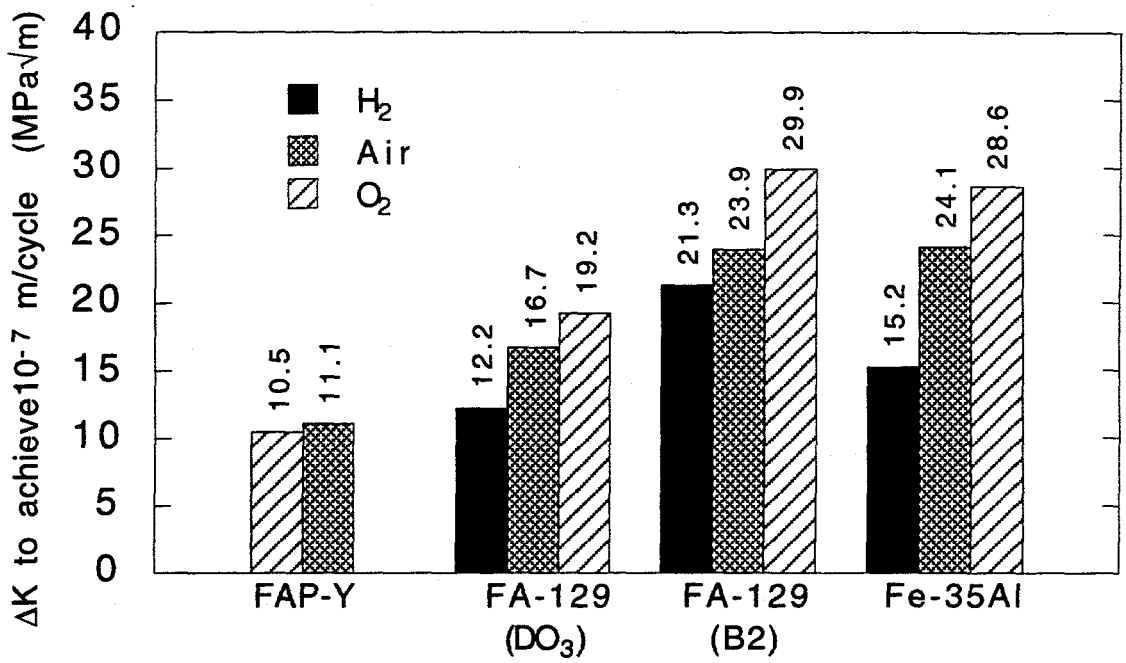

Fig. 4.21 Summary of stress intensities required to achieve a crack growth rate of 10^{-7} m/cycle in iron aluminides fatigued at room temperature. Frequency = 20Hz, R=0.5, temperature = 25°C.

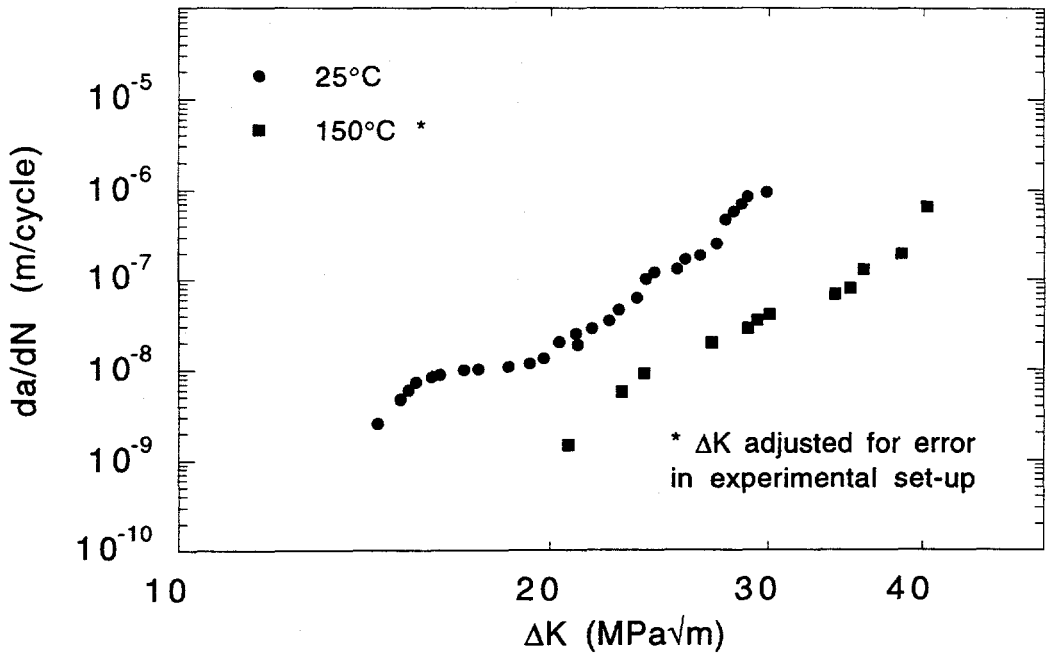

(a)

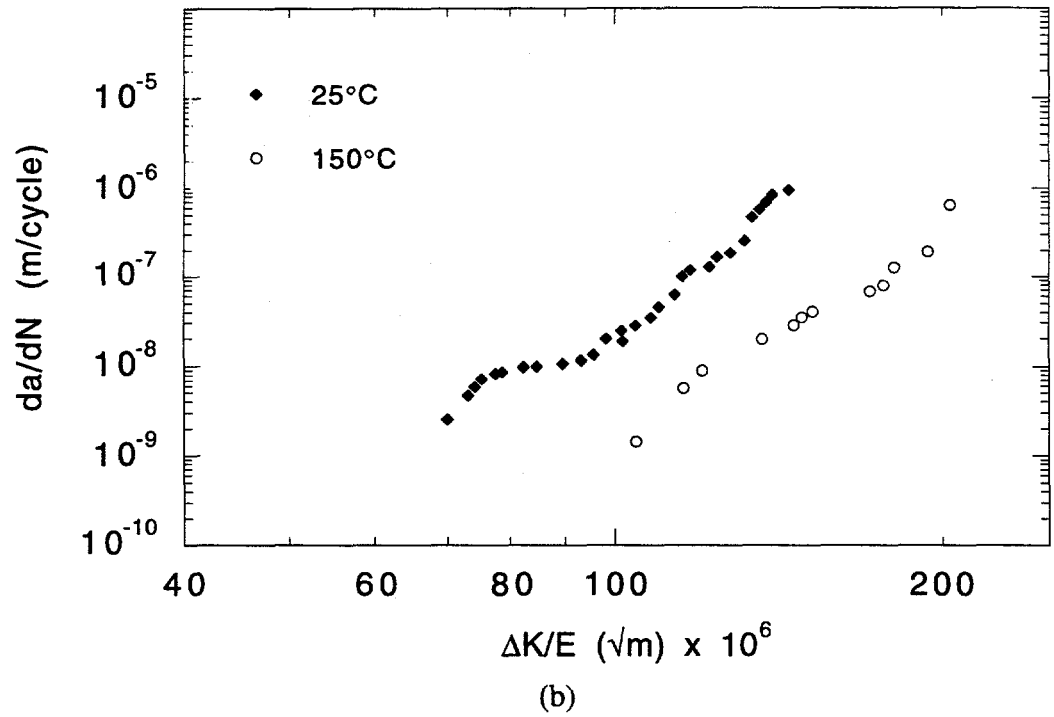

(b)

Fig. 4.22 Fatigue crack growth curves in B2 ordered FA-129 in air at 25°C and 150°C (a), and same data normalized by elastic modulus (b). Frequency = 20Hz, R=0.5.

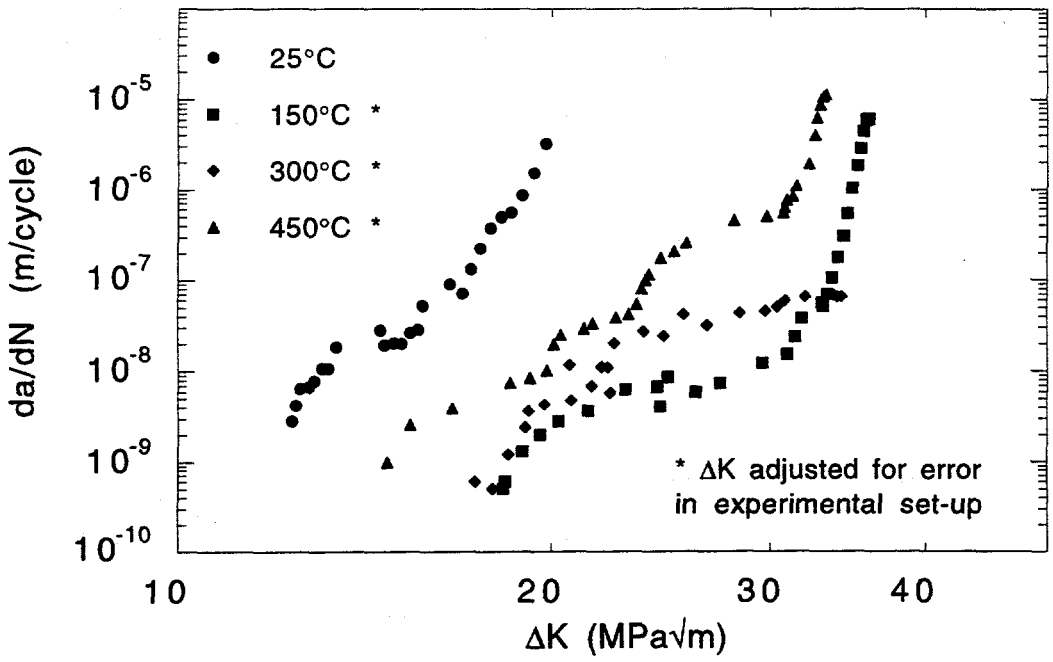

(a)

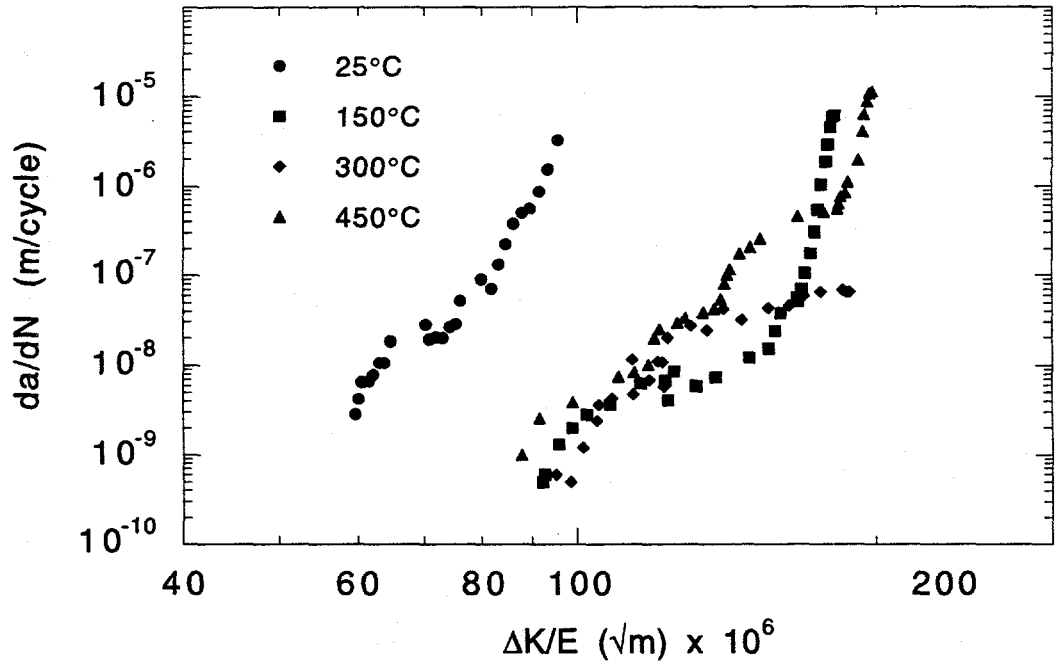

(b)

Fig. 4.23 Fatigue crack growth curves in DO_3 ordered FA-129 in air at various temperatures (a), and same data normalized by elastic modulus (b). Frequency = 20Hz, R=0.5.

4.4.4 Effect of Frequency on Fatigue Crack Growth

The da/dN vs. ΔK curves for B2 ordered FA-129 fatigued at frequencies of 20Hz, 2Hz, 0.2Hz, and 0.08Hz in air at 25°C are shown in Fig. 4.24. Also shown in this figure is the fatigue test conducted in oxygen, which is considered the inert environment for determining the magnitude of crack growth enhancement. The effect of frequency on the FCG resistance was not examined in the oxygen environment. However, no effect is expected as the oxygen environment has been shown to yield similar or better mechanical properties as a high-vacuum environment (see Appendix A and tensile data of section 4.3). As seen in Fig. 4.24, lower frequencies enhance crack growth rates at higher stress intensities. Frequency has a pronounced influence on the measured critical stress intensity. The highest K_C, 60MPa$\sqrt{m}$, is seen at the highest frequency of 20Hz. K_C steadily drops as frequency is decreased, to K_C = 50.4 MPa$\sqrt{m}$ at a frequency of 0.08Hz.

Frequency has almost no effect on threshold stress intensity. In all tests in air ΔK_{TH} was measured between 14 and 14.5MPa$\sqrt{m}$. The curves appear to diverge when the stress intensity range reaches about 15MPa$\sqrt{m}$ and the growth rate reaches $5x10^{-9}$ - $1x10^{-8}$ m/cycle.

4.4.5 Plasticity and Crack Closure Measurements

Calculations of the plastic zone size induced in the compact tension specimens during fatiguing, see Table 7 in section 5.1, indicate that plane strain conditions may not be satisfied in specimens with high toughness (i.e., B2 ordered FA-129 fatigued in O_2 at 25°C, or in air at elevated temperatures). Micro hardness measurements were made on CT specimens fatigued to failure at room temperature to determine if a large plastic zone occurred. These measurements were made along the edge of the crack front, beginning from the machined notch and continuing past the point of unstable crack growth (start of catastrophic failure). Only a slight increase in hardness was found along the crack in the

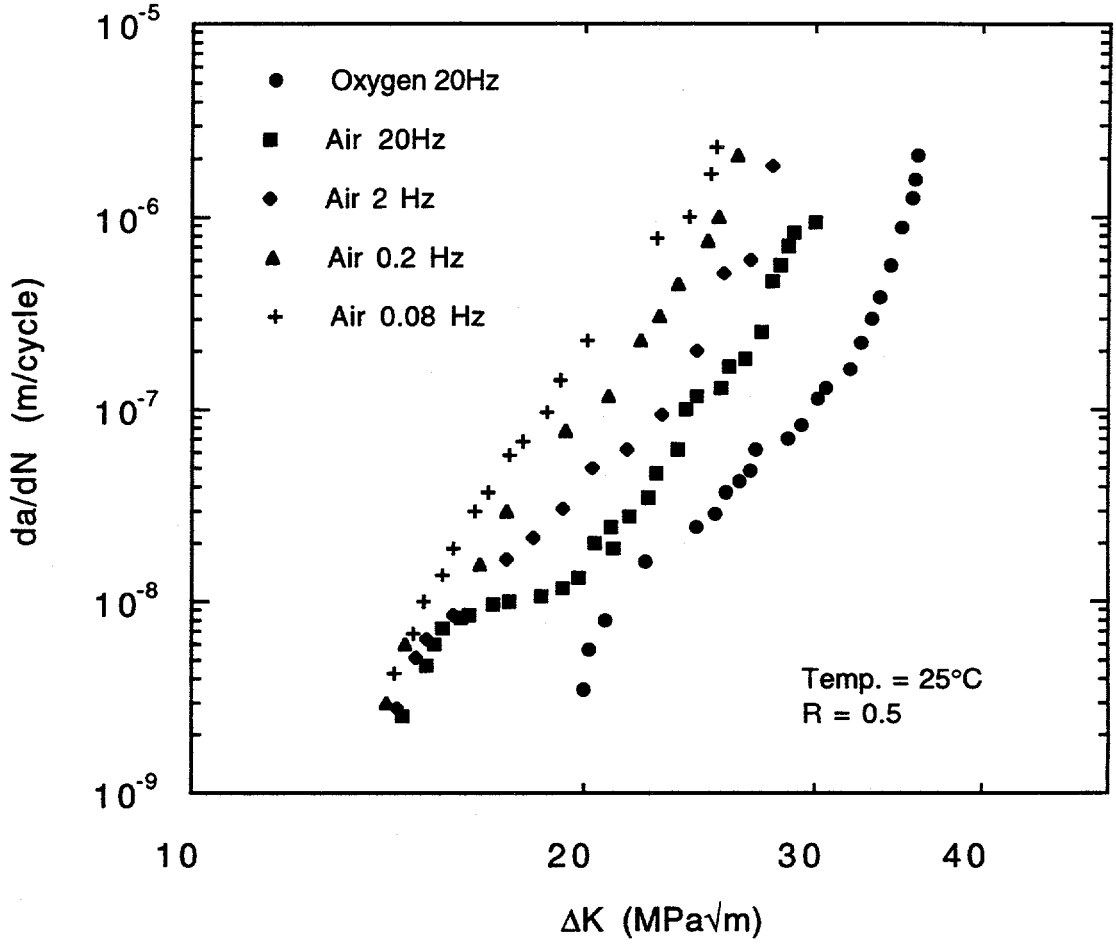

Fig. 4.24 Effect of frequency on B2 ordered FA-129 fatigued in air at room temperature. R=0.5.

stable region, while significant hardening was found beyond the point of unstable crack growth. This observation indicates that little work-hardening occurs during fatiguing, and is consistent with predominantly plane strain deformation.

Another factor which often influences fatigue crack growth testing is closure, either oxide, plasticity, or surface roughness induced. Fig. 4.25 shows the measured COD vs. load applied over an individual cycle at crack lengths of 4.64 mm, 5.15 mm, and 5.80 mm for B2 ordered FA-129 fatigued in air at 25°C. The curves show no deviation from linearity, indicating that no measurable crack closure was observed. These results also indicate that there is little plasticity or surface roughness induced closure during stable crack growth. At long crack lengths just prior to failure a slight curvature of the COD vs. load line at high loads was observed. This indicates the onset of plasticity and plane stress conditions just prior to catastrophic failure. The specimen compliance, determined from the COD measurements demonstrated the expected increase as crack length increased.

4.5 Fractography of FCG Specimens

The crack propagation direction in all fracture surfaces shown in this section is horizontal from left to right.

The fracture surface of the fatigued iron aluminides was found to be dependent on alloy composition and ordered state, environment, and temperature. Failure mode in alloy FAP-Y is entirely transgranular, by what appears to be a tearing mechanism; with extensive cleavage facets in hydrogen gas and neither facets nor extensive dimpling evident in air or oxygen. Fig. 4.26 shows the faceted surface of FAP-Y fatigued in hydrogen gas. Fig. 4.27 shows the transgranular fracture surface of alloy FAP-Y fatigued in air near the critical crack length. When fatigued in oxygen, the fracture surface of FAP-Y remains predominantly transgranular tearing in nature, very similar to that observed in air.

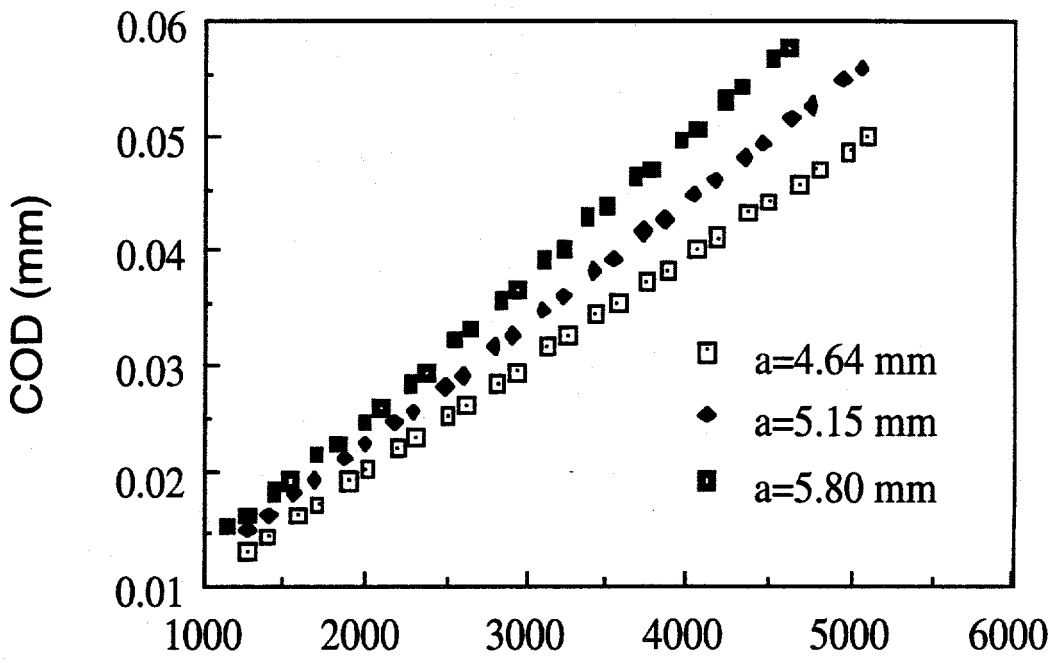

Fig. 4.25 Crack opening displacement vs. load at crack lengths of 4.64mm, 5.15mm, and 5.80 mm. Material is B2 ordered FA-129 in air at 25°C. Frequency = 20Hz, R=0.5.

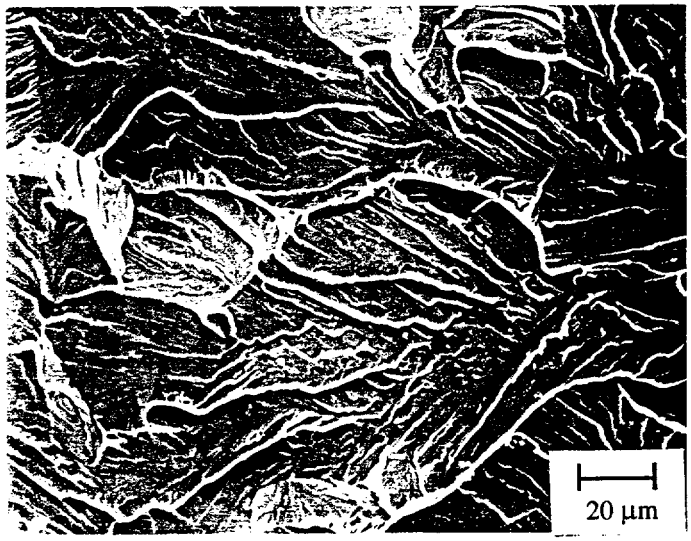

Fig. 4.26 Fracture surface of alloy FAP-Y fatigued in hydrogen gas at 25°C.

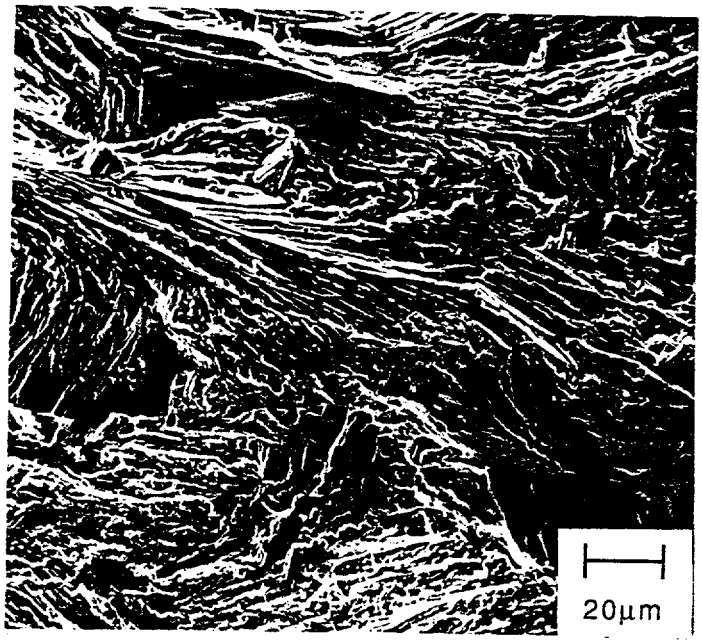

Fig. 4.27 Fracture surface of alloy FAP-Y fatigued in air at 25°C near the critical point at ΔK=12.5 MPa$\sqrt{m}$.

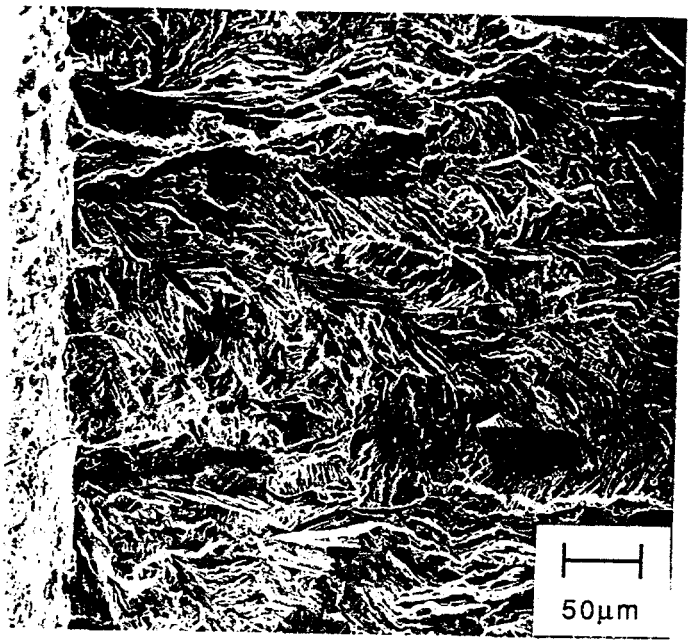

(a)

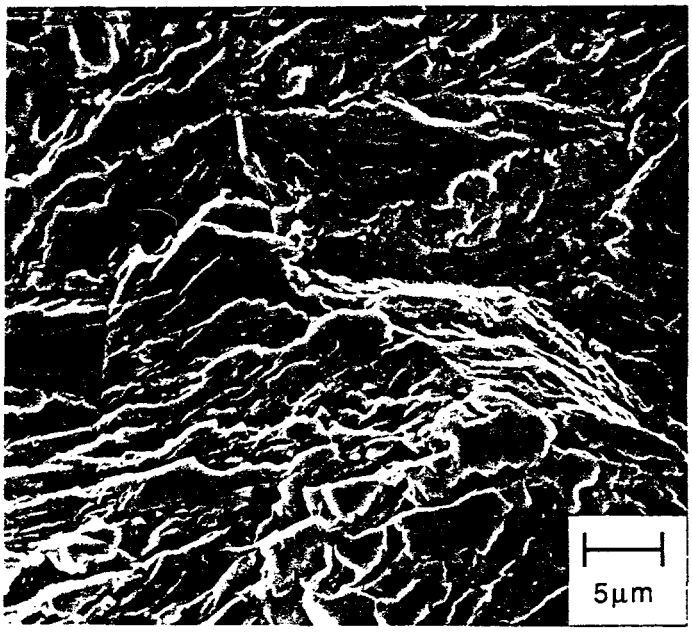

b)

Fig. 4.28 Fracture surface of alloy FAP-Y fatigued in oxygen at 25°C, in pre-cracking region at ΔK=10 MPa$\sqrt{m}$ (a) and higher magnification of same region (b).

Fig. 4.28a shows the pre-cracking zone of FAP-Y fatigued in oxygen, and Fig. 4.28b shows a higher magnification of the region seen in Fig. 4.28a. Occasional regions with fatiguestriations were observed at low to intermediate ΔK levels and crack growth rates, as seen in Fig. 4.29a. The striation spacing is approximately 2μm, which corresponds to approximately 10 times the measured crack growth rate of $2x10^{-7}$ m/cycle.

A small amount of longitudinal cracking was observed at higher stress intensities in FAP-Y fatigued in oxygen, as seen in Fig. 4.29b. The crack plane in the compact tension specimens is the short-transverse plane, which is perpendicular to the elongated direction of the grains. The longitudinal cracks run along the longitudinal plane, parallel to the elongated direction of the grains.

Once the critical stress intensity is reached and the crack grows catastrophically, there is a shift from transgranular tearing to transgranular cleavage facets. This shift is very sudden and the onset of the overload region is very clear, as seen in Fig. 4.30.

Alloy FA-129 displayed a variety of fracture modes. In the B2 ordered state at 25°C, the fracture surface of FA-129 varied with environment. Fracture surface appearance changed from a dimpled, transgranular appearance in oxygen, to a combination of transgranular tearing and cleavage faceting in air, to predominantly large, pronounced cleavage facets in hydrogen gas. The dimpled surface in oxygen is shown in Fig. 4.31. This type of fracture surface is indicative of microvoid coalescence and is often associated with ductile materials. No evidence of fatigue striations or longitudinal cracking was observed in oxygen.

Fig. 4.32a show the combination of tearing and cleavage faceting observed in B2 ordered FA-129 in air. Large, widely spaced striations were observed as well (Fig. 4.32b). These striations do not correspond to one striation per cycle. For example, the striations

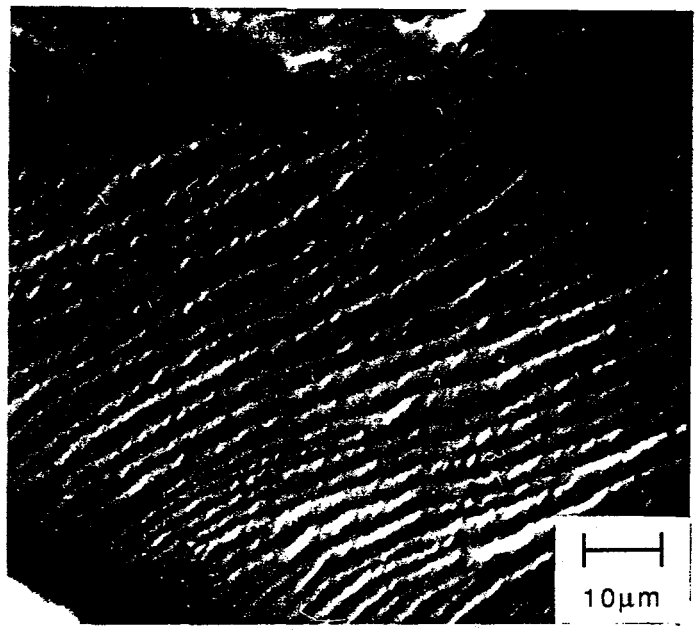

(a)

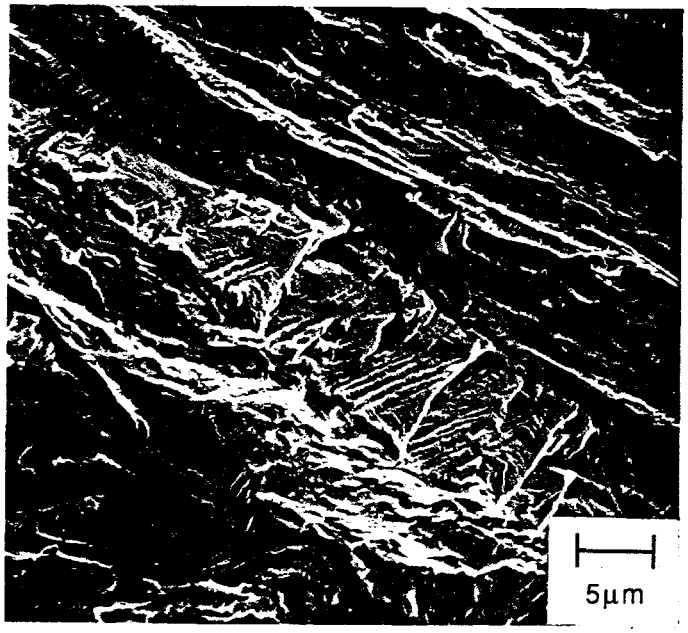

Fig. 4.29 Fracture surface of alloy FAP-Y fatigued in oxygen at 25°C showing fatigue striations at $\Delta K=11.0$ MPa$\sqrt{m}$.(a), and showing longitudinal cracks at $\Delta K=11.5$ MPa$\sqrt{m}$ (b).

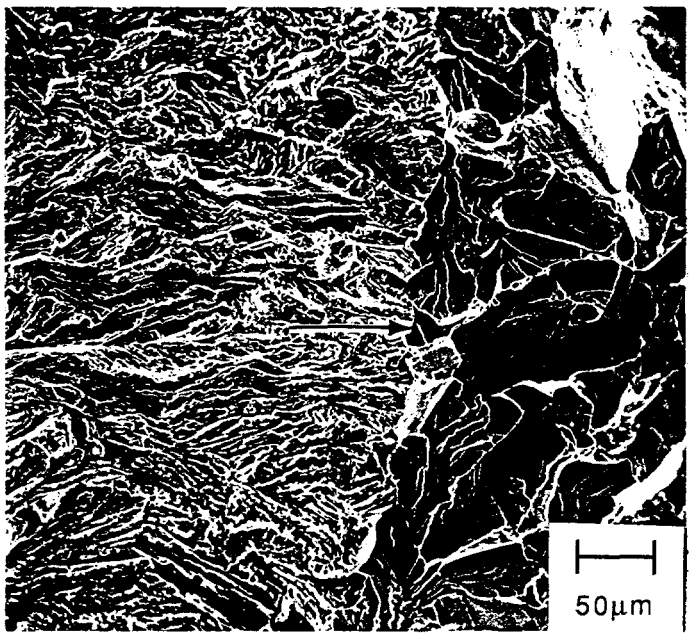

Fig. 4.30 Fracture surface of alloy FAP-Y fatigued in oxygen at 25°C, the arrow indicates the transition from stable to catastrophic crack growth at ΔK=20 MPa$\sqrt{m}$.

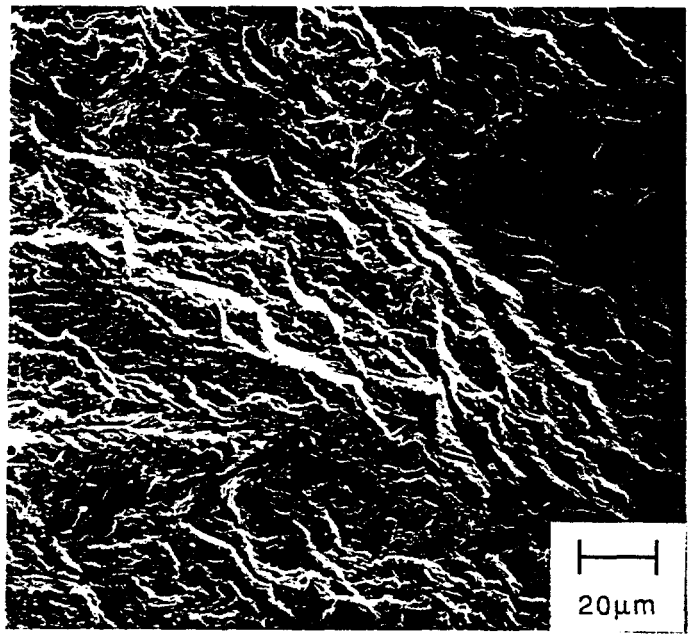

Fig. 4.31 Fracture surface of B2 ordered FA-129 fatigued in oxygen at 25°C at ΔK=25 MPa$\sqrt{m}$.

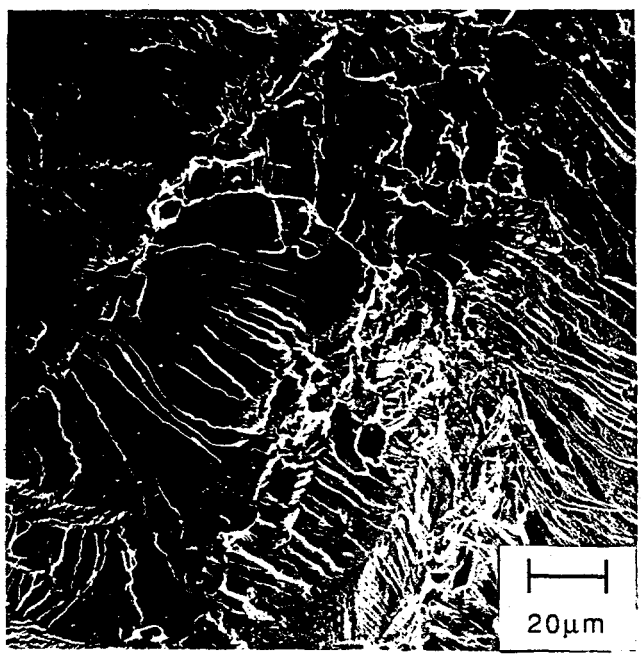

a)

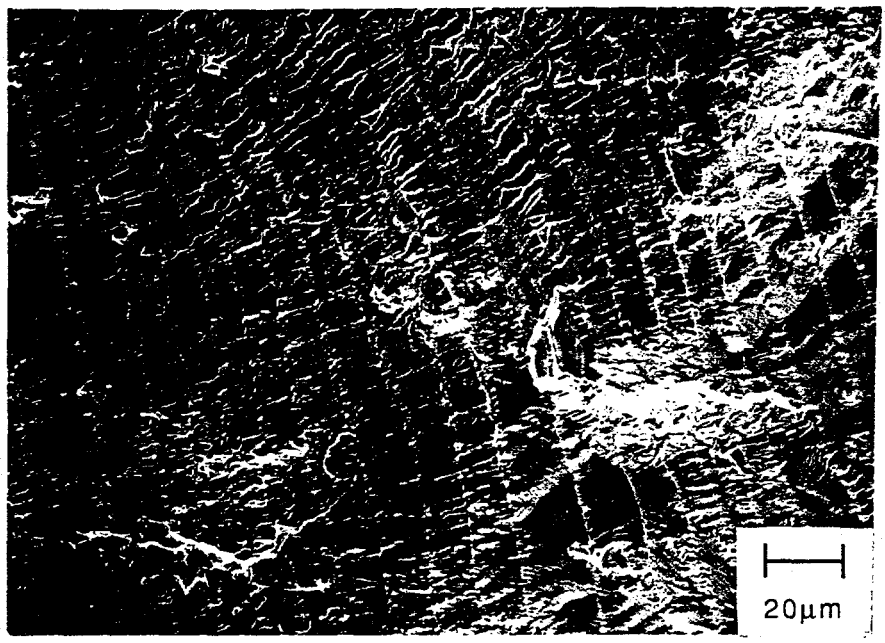

b)

Fig. 4.32 Fracture surface of B2 ordered FA-129 fatigued in air at 25°C, showing combination of tearing and cleavage at ΔK=28 MPa$\sqrt{m}$ (a), and showing striations at ΔK=30 MPa$\sqrt{m}$ (b).

seen in Fig. 4.32b are spaced 10^{-5} m apart, while the measured da/dN value was $2x10^{-8}$ m/cycle. As with the fatigue tests in oxygen, no longitudinal cracking was observed.

The fracture surface of B2 ordered FA-129 fatigued in hydrogen gas is shown in Figs. 4.33a-c. The pronounced cleavage facets and a large number of longitudinal cracks are visible in Fig. 4.33a. Widely spaced striations are observed as well (Fig. 4.33b), which are spaced much further apart than the microscopic measured da/dN value. Another large longitudinal crack can be seen in Fig. 4.33b. Occasionally, alternating tearing-like regions and cleavage failure was observed, as can be seen in Fig. 4.33c. Here, the crack advances in a transgranular cleavage manner, then suddenly switches to a tearing mode, and switches back again.

Decreasing the fatigue frequency of B2 ordered FA-129 tested in air had the effect of making the cleavage faceting more pronounced introducing a small amount of intergranular fracture. Figs. 4.34a-c show the fracture surface of these tests at 2.0, 0.2, and 0.08Hz, respectively. The fracture surface at 2.0Hz (Fig. 4.34a) shows mostly a transgranular tearing fracture mode, similar to that seen in air at 20Hz (Fig. 4.32a). At 0.2Hz, (Fig 4.34b), the fracture surface shows cleavage facets with well defined river patterns, as well as some intergranular facets. At 0.08Hz, (Fig. 4.34c), the fracture surface displays an even greater degree of transgranular cleavage faceting, and occasional intergranular facets.

When the test temperature was increased to 150°C, B2 ordered FA-129 fatigued in air exhibited a dimpled fracture surface, similar to that seen for oxygen at 25°C. However, occasional widely spaced striations, which appeared to be cleavage-like in nature were observed. The alternating transgranular dimples and cleavage-like striations are seen in Fig. 4.35. There was no evidence of longitudinal cracking at 150°.

DO_3 ordered FA-129 also shows a shift in fracture mode at 25°C with varying environment. In oxygen, DO_3 ordered FA-129 failed in a transgranular manner, while in

air and hydrogen failure was by a combination of transgranular cleavage and intergranular failure. Figs. 4.36 shows the fracture surface of DO_3 ordered FA-129 fatigued in oxygen. A mixture of transgranular cleavage facets and transgranular tearing is seen. Some areas of the fracture surface showed widely spaced striations, but no longitudinal cracking occurred.

When fatigued in air, DO_3 ordered FA-129 showed a combination of transgranular and intergranular failure. However, the two types of fracture surface were not randomly distributed throughout. The fracture mode clearly showed a dependence on the applied stress-intensity. At low stress intensity levels (13.3-15.0MPa$\sqrt{m}$), the fracture mode was predominantly intergranular (Fig.4.37a), while at intermediate stress intensity levels (15.0-17.5MPa$\sqrt{m}$) there is a sudden change to mixed intergranular failure and cleavage facets (Fig. 4.37b). The fracture mode then becomes predominantly cleavage faceted at high stress intensity levels (17.5-19.8MPa$\sqrt{m}$). This dependence on stress intensity is consistent across the sample thickness, with the transitions occurring at only slightly longer crack lengths at the center than near the edges.

When fatigued in hydrogen gas, DO_3 ordered FA-129 failed by a combination of transgranular cleavage and intergranular fracture (Fig. 4.38a). However, there was no clear dependence of fracture mode on stress intensity level, as there was in air. The degree of intergranular failure was greater in hydrogen gas than in air. Many of the transgranular areas which were observed exhibited a step-like pattern (Fig. 4.38b). Also, a small amount of cleavage along cubic planes was observed (Fig. 4.38c), but this type of cleavage faceting is not representative of the fracture surface in general.

a)

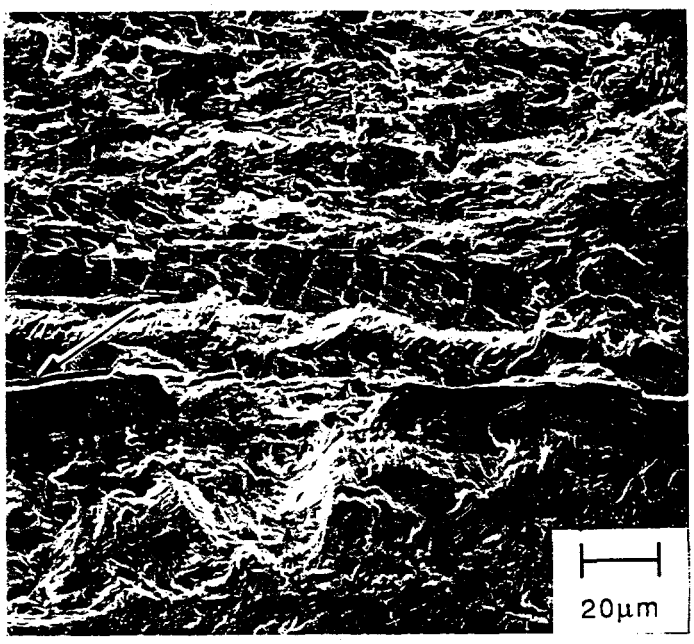

b)

Fig. 4.33 Fracture surface of B2 ordered FA-129 fatigued in hydrogen gas at 25°C, showing cleavage at $\Delta K=18$ MPa$\sqrt{m}$; arrow indicates longitudinal crack (a), and showing striations at $\Delta K=22$ MPa$\sqrt{m}$ (b).

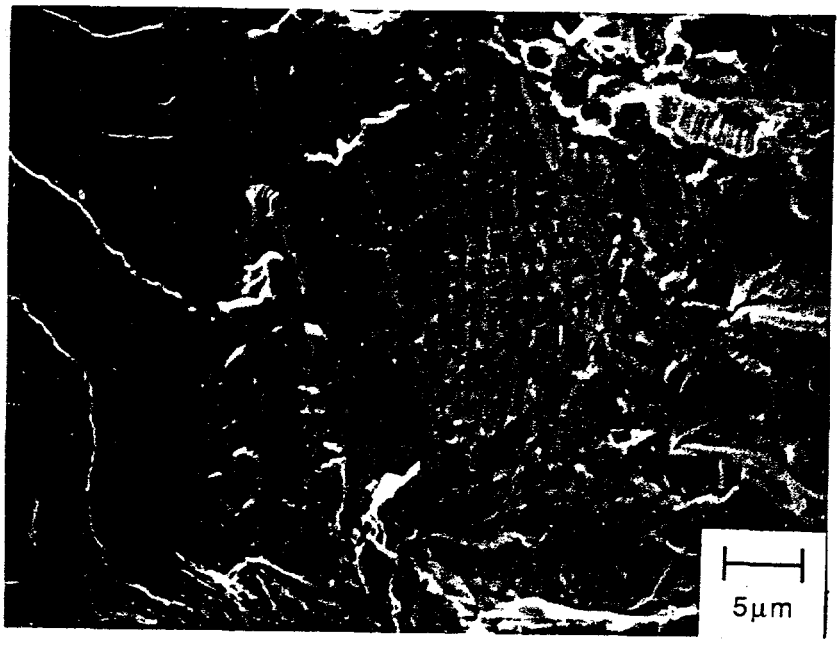

c)

Fig. 4.33 continued — Fracture surface of B2 ordered FA-129 fatigued in hydrogen gas at 25°C, showing alternating cleavage and showing striations at $\Delta K=24$ MPa$\sqrt{m}$(c).

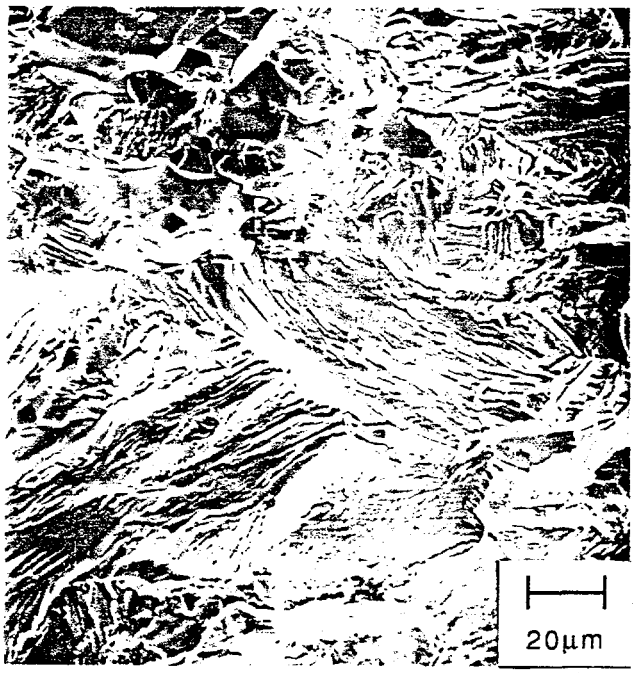

(a)

(b)

Fig. 4.34 Fracture surface of B2 ordered FA-129 fatigued in air at 25°C at frequency = 2.0 Hz, ΔK=22 MPa$\sqrt{m}$(a) and 0.2Hz, ΔK=21 MPa$\sqrt{m}$ (b).

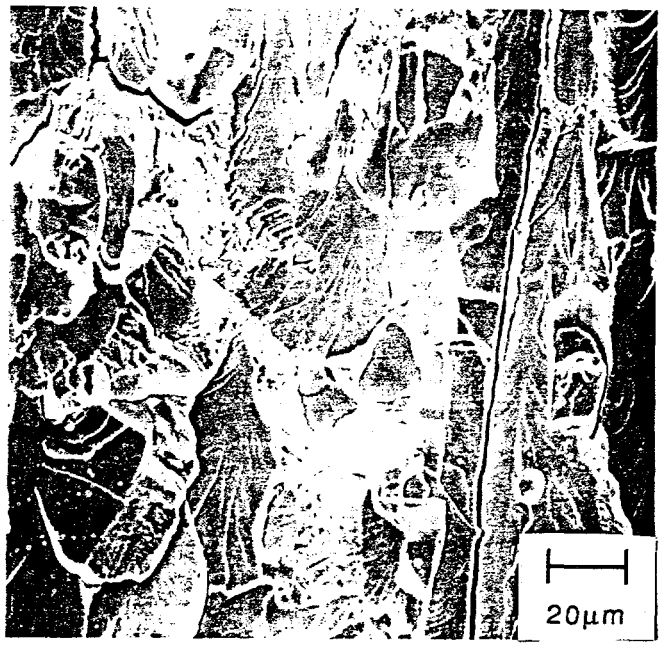

c)

Fig. 4.34 Fracture surface of B2 ordered FA-129 fatigued in air at 25°C at continued frequency =0.08Hz (c), ΔK=20 MPa$\sqrt{m}$.

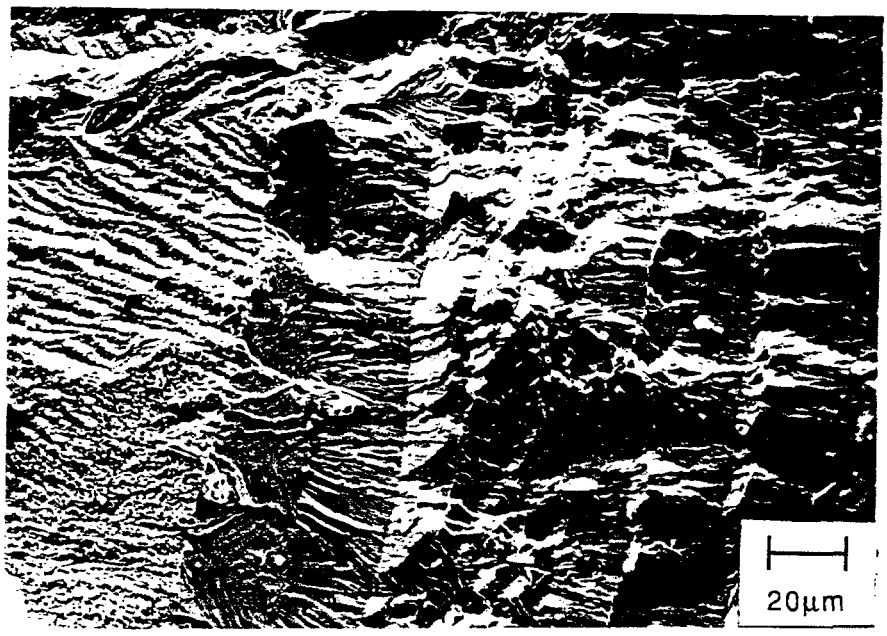

Fig. 4.35 Fracture surface of B2 ordered FA-129 fatigued in air at 150°C at ΔK=30 MPa$\sqrt{m}$.

Fig. 4.36 Fracture surface of DO_3 ordered FA-129 fatigued in oxygen at 25°C at ΔK=18 MPa$\sqrt{m}$, showing faceting.

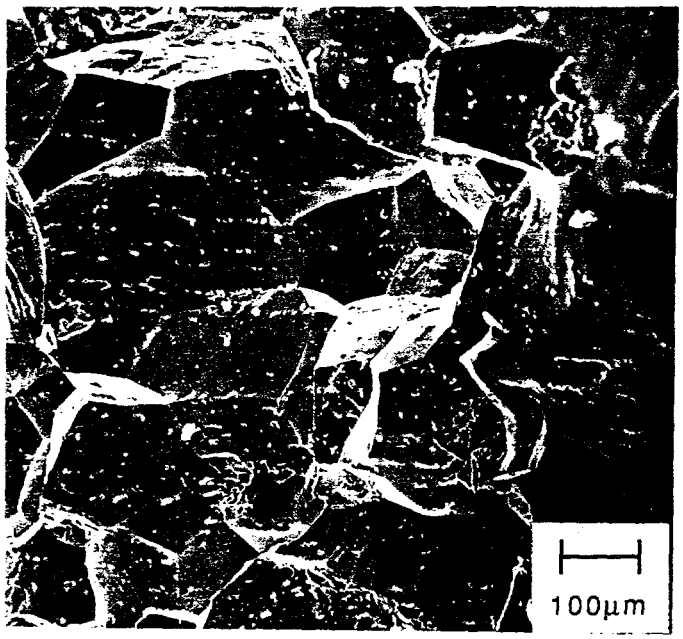

a)

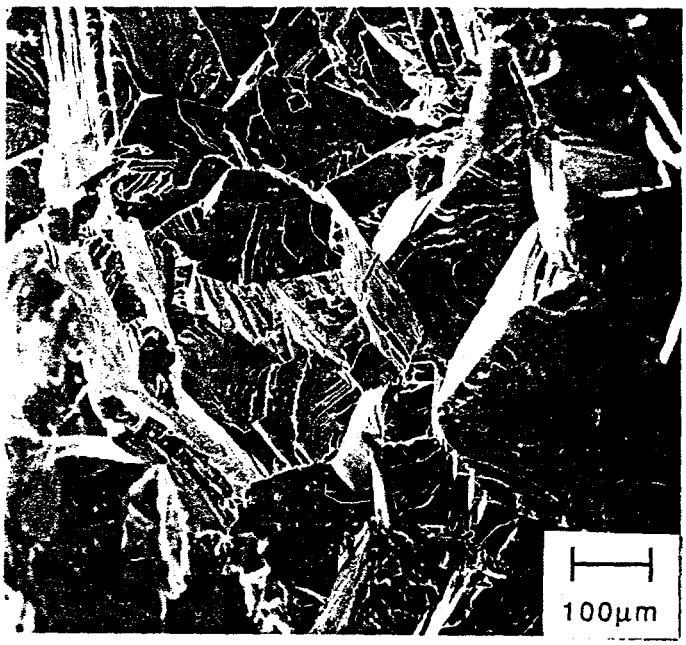

b)

Fig. 4.37 Fracture surface of DO_3 ordered FA-129 fatigued in air at 25°C, showing intergranular failure at 14.5 MPa$\sqrt{m}$ (a), and cleavage facets at 18 MPa$\sqrt{m}$ (b).

At temperatures of 150°C to 450°C in air, DO_3 ordered FA-129 exhibited a transgranular fracture surface. Widely space striations are observed which are most likely caused by cleavage alternating above and below the crack plane. The crack may begin to grow along a plane at an angle to the original crack plane. When the crack reaches some distance above or below original crack reverses and begins to grow on a plane which will bring it back to the original crack plane. Figs. 4.39a and 4.39b show these surfaces at 150°C and 450°C, respectively. Note that at 150°C (Fig. 4.39a) a small amount of intergranular fracture is observed, as well as a few longitudinal cracks. No intergranular fracture or longitudinal cracking were observed at 300°C and 450°C.

Failure of Fe-35Al was by transgranular cleavage in air and hydrogen gas. Figs. 4.40a-c shows the fracture surface of Fe-35Al fatigued in air at 25°C. The facets are very large (Fig. 4.40a) compared to those of alloy FA-129. At higher magnifications, a step-like pattern is evident (Fig. 4.40b), similar to those seen in DO_3 ordered FA-129 fatigued in hydrogen gas (Fig. 4.40b). Fatigue striations superimposed on the facets were observed throughout the specimen (Fig. 4.40c). The cleavage facets in hydrogen gas were similar in appearance to those in air, and are shown in Fig. 4.41.

When fatigued in oxygen, the fracture surface of Fe-35Al was mostly dimpled, with some regions of mixed dimpling and cleavage tongues as seen in Fig. 4.42. These cleavage tongues occur when a crack propagates in a brittle manner along a twin-matrix interface (87). Mechanical twins which were observed in the as-received Fe-35Al material (see Fig. 4.4a) were not completely removed by the heat treatment used. Occasional striations were observed as well which were spaced farther apart than the per cycle crack increment.

A summary of the fatigue crack growth fracture surface appearance is listed in Table 6.

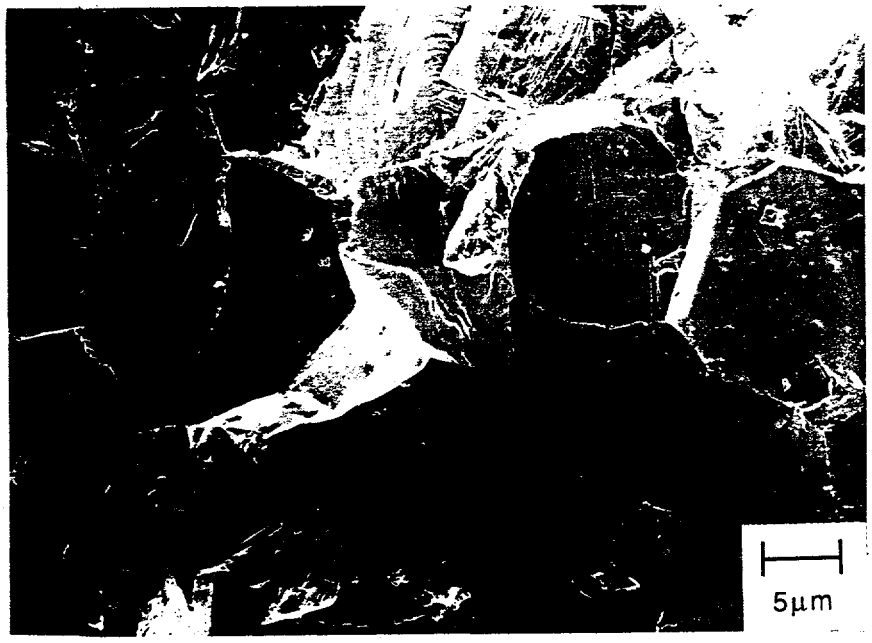

a)

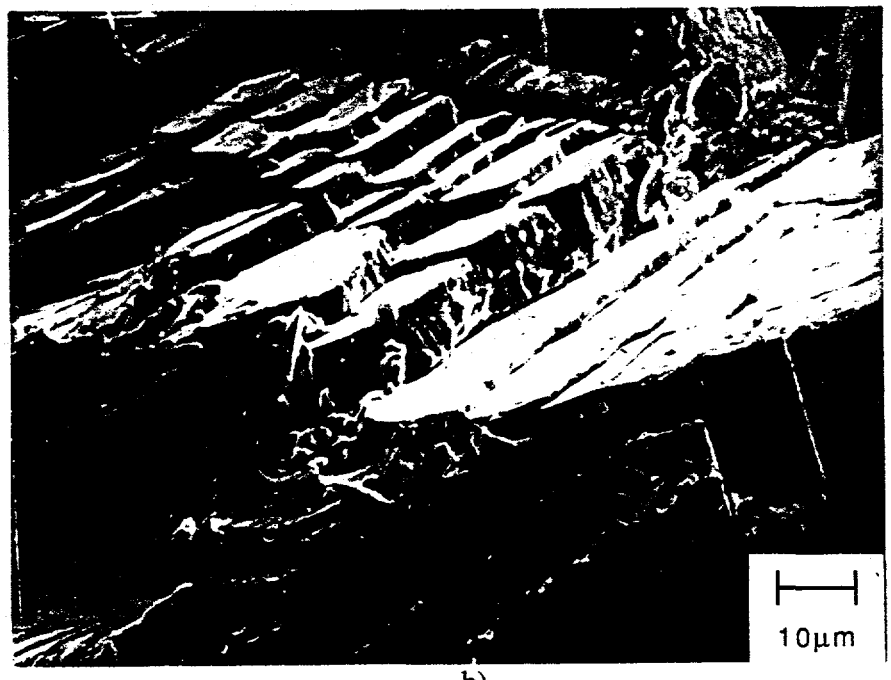

b)

Fig. 4.38 Fracture surface of DO_3 ordered FA-129 fatigued in hydrogen gas at 25°C at $\Delta K = 13$ MPa$\sqrt{m}$, showing mixed mode failure (a), and at $\Delta K = 15$ MPa$\sqrt{m}$ showing step-like cleavage faceting (b).

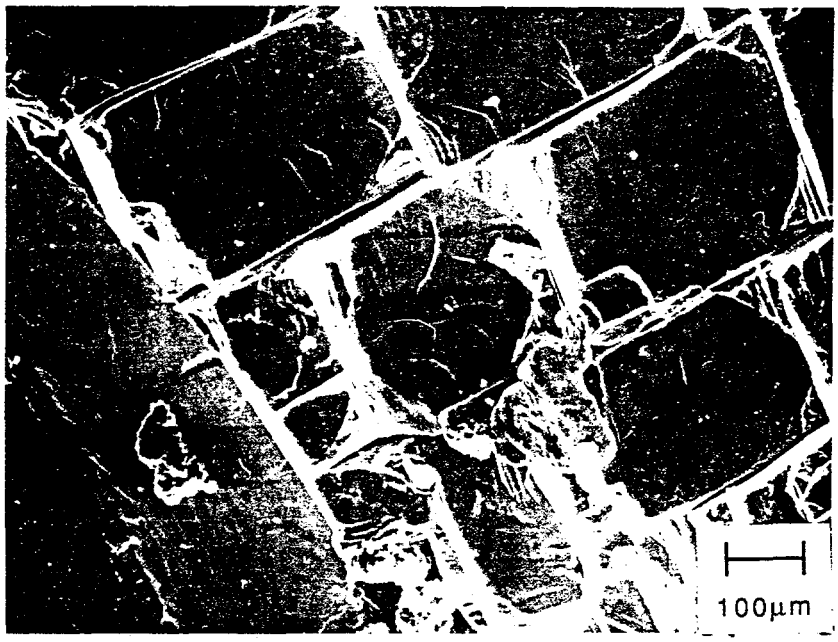

c)

Fig. 4.38 continued — Fracture surface of DO_3 ordered FA-129 fatigued in hydrogen gas at 25°C at ΔK=15 MPa$\sqrt{m}$, showing faceting on cubic planes(c).

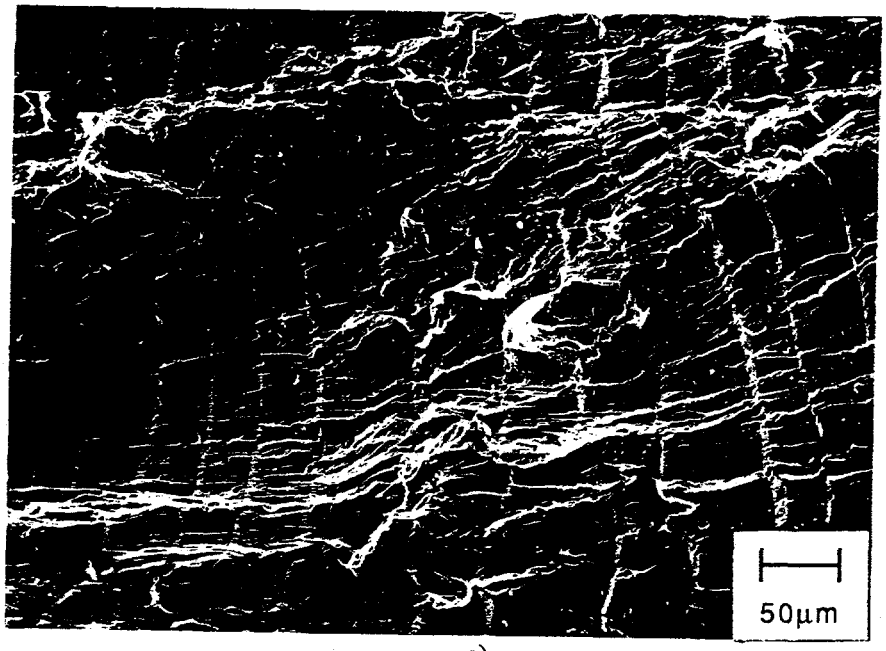

a)

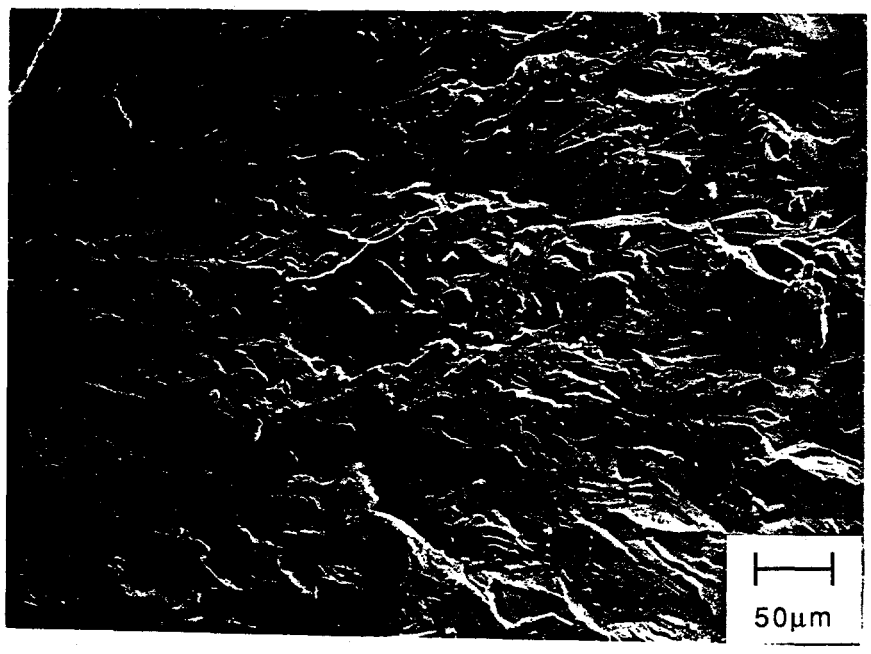

b)

Fig. 4.39 Fracture surface at ΔK=30 MPa$\sqrt{m}$ of DO_3 ordered FA-129 fatigued in air at 150°C (a), and at ΔK=20 MPa$\sqrt{m}$ at 450°C (b).

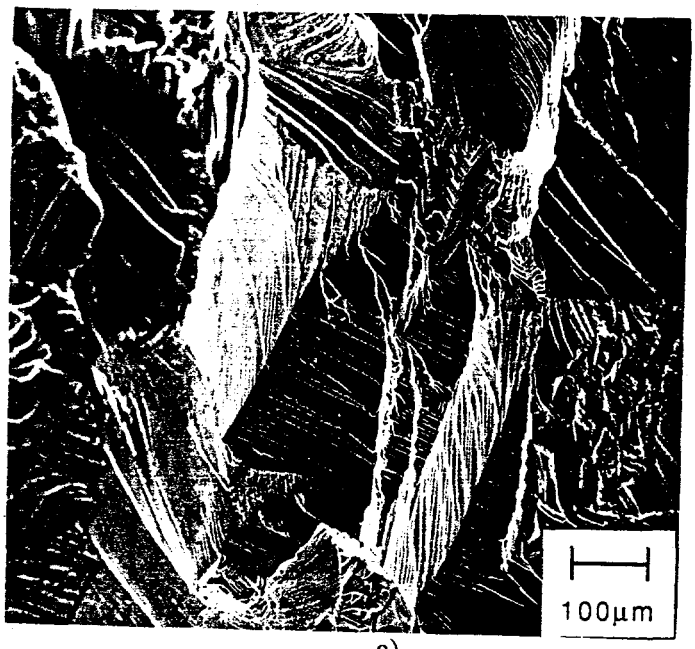

a)

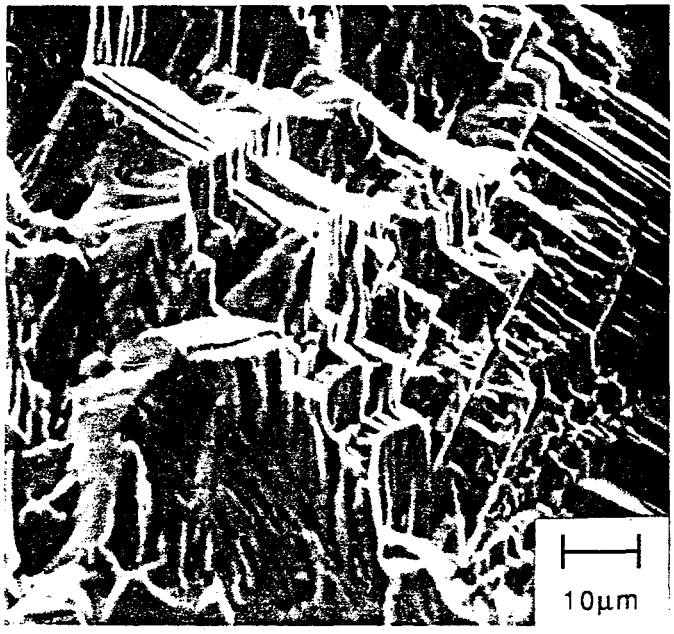

b)

Fig. 4.40 Fracture surface at ΔK=20 MPa$\sqrt{m}$ of Fe-35Al fatigued in air at 25°C, showing transgranular facets (a), and at ΔK=22 MPa$\sqrt{m}$ showing step-like patterns (b).

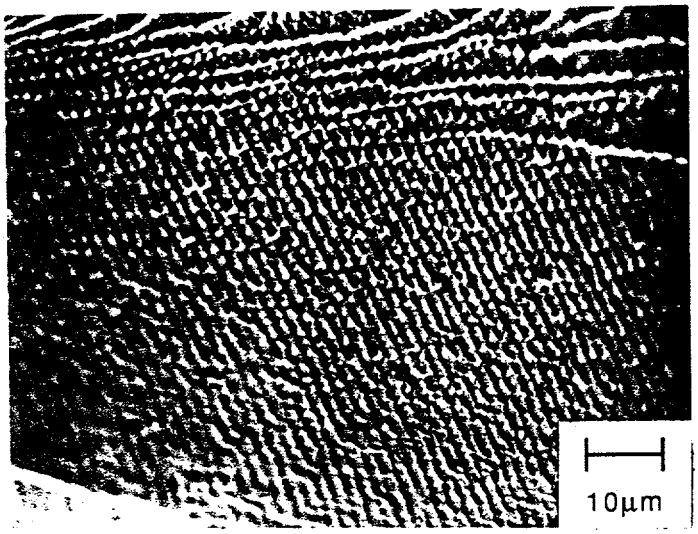

c)

Fig. 4.40 continued — Fracture surface at ΔK=23 MPa$\sqrt{m}$ of Fe-35Al fatigued in air at 25°C, showing fatigue striations (c).

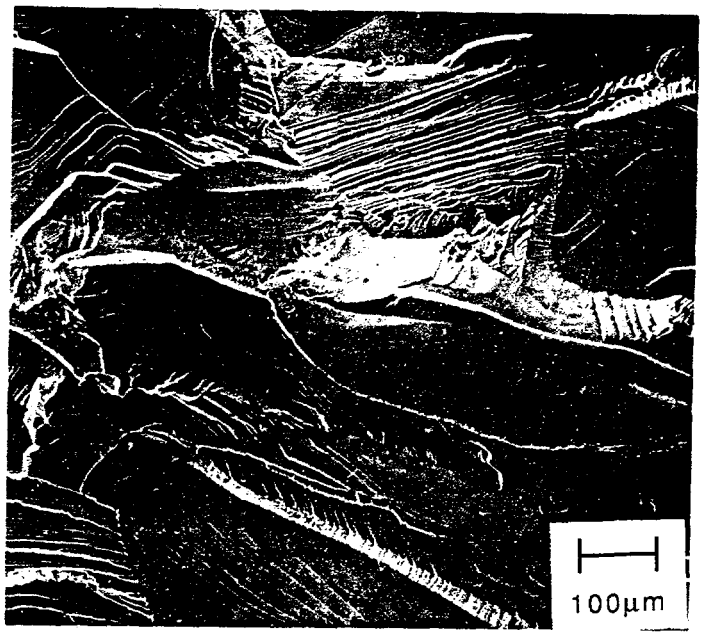

Fig. 4.41 Fracture surface at ΔK=16 MPa$\sqrt{m}$ of Fe-35Al fatigued in hydrogen gas at 25°C.

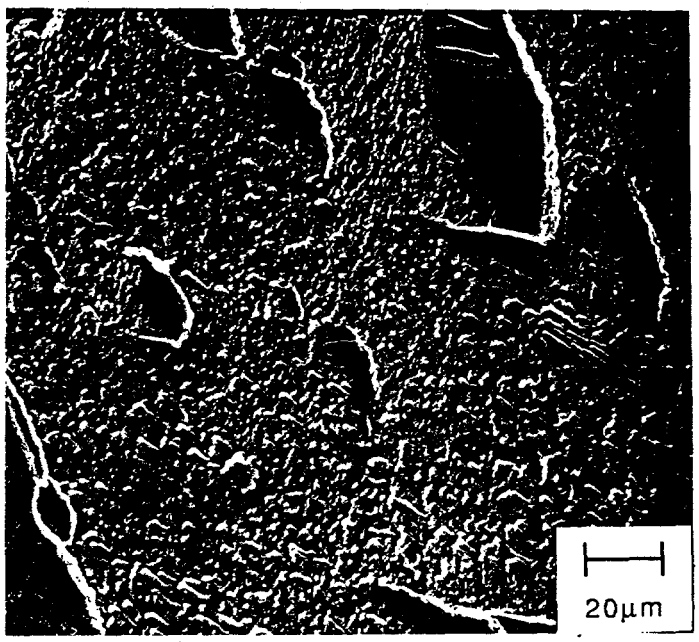

Fig. 4.42 Fracture surface at ΔK=28 MPa$\sqrt{m}$ of Fe-35Al fatigued in oxygen at 25°C.

TABLE 6
Appearance of Fracture Surface in Fatigued Iron Aluminides

Alloy	Environment	Fracture Surface
FAP-Y	O_2, 25°C	TG tearing, no striations
FAP-Y	Air, 25°C	TG tearing, no striations
FAP-Y	H_2, 25°C	TG cleavage
FA-129 (B2)	O_2, 25°C	Dimpled, few striations
FA-129 (B2)	Air, 25°C	TG, some TG cleavage, many striations
FA-129 (B2)	H_2, 25°C	Mostly TG cleavage, few striations
FA-129 (DO_3)	O_2, 25°C	Dimpled + cleavage
FA-129 (DO_3)	Air, 25°C	TG cleavage + IG at low ΔK
FA-129 (DO_3)	H_2, 25°C	TG cleavage + IG
Fe-35Al (DO_3)	O_2, 25°C	Mostly dimpled
Fe-35Al (DO_3)	Air, 25°C	TG cleavage
Fe-35Al (DO_3)	H_2, 25°C	TG cleavage
FA-129 (B2)	Air, 150°	Dimpled
FA-129 (DO_3)	Air, 150°C	TG cleavage
FA-129 (DO_3)	Air, 300°C	TG cleavage
FA-129 (DO_3)	Air, 450°C	TG cleavage

4.6 Transmission Electron Microscopy of FCG Specimens

TEM foils from annealed, but unfatigued, compact tension specimens were examined to determine the undeformed dislocation structure. The dislocation density of undeformed FAP-Y and FA-129 aluminides was extremely low. Fig. 4.43 shows a typical undeformed region of alloy FAP-Y, with a precipitate situated at a grain boundary triple point, but no dislocations. Undeformed B2 and DO_3 FA-129 generally had more dislocations than undeformed FAP-Y, as seen in Fig. 4.44 for DO_3 ordered FA-129, but the subgrain structure and dislocation arrays observed in the fatigued material was not present.

After being fatigued, B2 ordered FA-129 showed a duplex microstructure: predominantly unrecrystallized with a cellular subgrain structure (see Fig. 4.45a). However, some recrystallized regions were observed with a lower dislocation density, more paired dislocation, and APB's.

The DO_3 ordered FA-129 specimens exhibited few or no subgrains, a lower dislocation density than the B2 material (see Fig. 4.45b), and a uniform network of APB's, as seen in Fig. 4.46. The dislocations which were observed were also more likely to be paired than in the B2 material. The DO_3 grain boundaries tended to be free of dislocations while the B2 material often had dense dislocation networks emanating from the grain boundaries.

Heterogeneously distributed coarse precipitates (up to 5 μm diameter), which were believed to be niobium carbides, were observed. The precipitates often acted as dislocation sources, possibly as a result of mismatched thermal contraction during quenching. These precipitates are seen in the optical micrograph in Fig. 4.1d.

Diffraction patterns were obtained from all samples, and from these it was determined that the proper ordered state (B2 or DO_3) was achieved in each case.

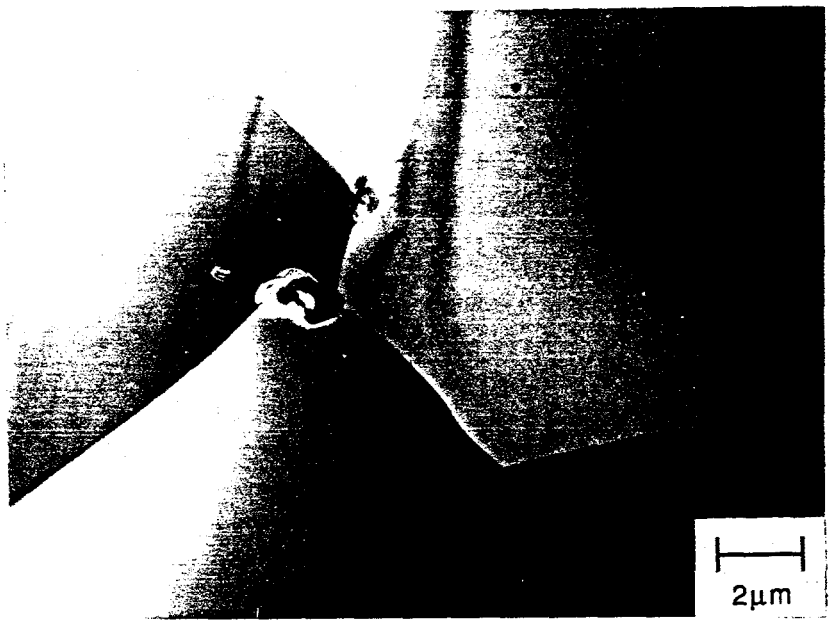

Fig. 4.43 Undeformed microstructure of FAP-Y, showing precipitate at grain boundary.

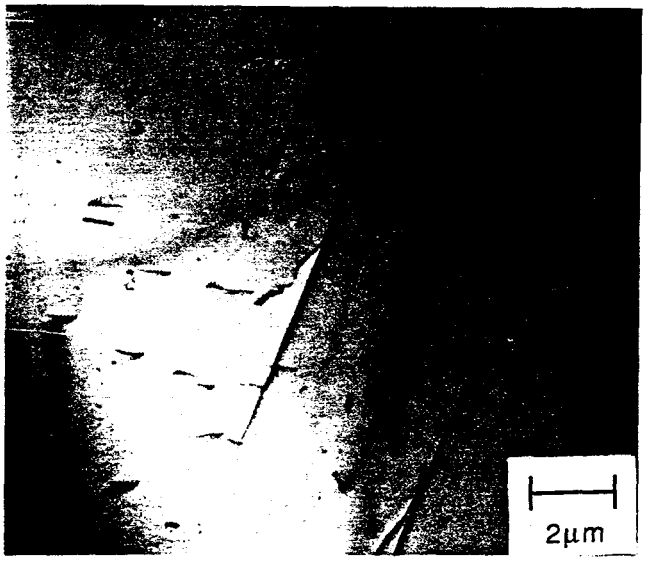

Fig. 4.44 Undeformed microstructure of B2 ordered FA-129.

Fig. 4.45 Dislocation structure in B2 ordered FA-129 fatigued in air at 25°C.

Fig. 4.46 APB's in DO_3 ordered FA-129 fatigued in hydrogen at 25°C.

Both environment and test temperature affected the dislocation density observed in FA-129. Increased numbers of dislocations in both ordered states were observed as the environment changed through hydrogen, air, and oxygen. In both ordered states, much higher dislocation densities were observed at elevated temperatures than at room temperature, and large arrays of dislocations were observed (Fig. 4.47), sometimes forming subgrains or cells. Microscopy on foils taken away from the fracture surface, and from untested material, showed extremely few dislocations. This confirms that there was no significant damage induced in the foils during the preparation process.

TEM analysis of fatigued FAP-Y indicates a much lower dislocation density than in FA-129, which is consistent with the lower fatigue crack growth resistance measured in FAP-Y. Figs. 4.48a and 4.48b show the dislocation structures of FAP-Y fatigued in air and oxygen, respectively. Note the small round structures in Fig. 4.48a which may be dislocation loops.

Alloy FAP-Y has a precipitate distribution similar to that seen in alloy FA-129. However, the precipitates are of various types, as EDAX chemical analysis shows. The predominant precipitates are zirconium rich (shown in Fig. 4.49 with the corresponding EDAX analysis), and some have elevated levels of chromium as well (shown in Fig. 4.50 with the corresponding EDAX analysis).

Fig. 4.47 Dislocation array in DO_3 ordered FA-129 fatigued in air at 450°C.

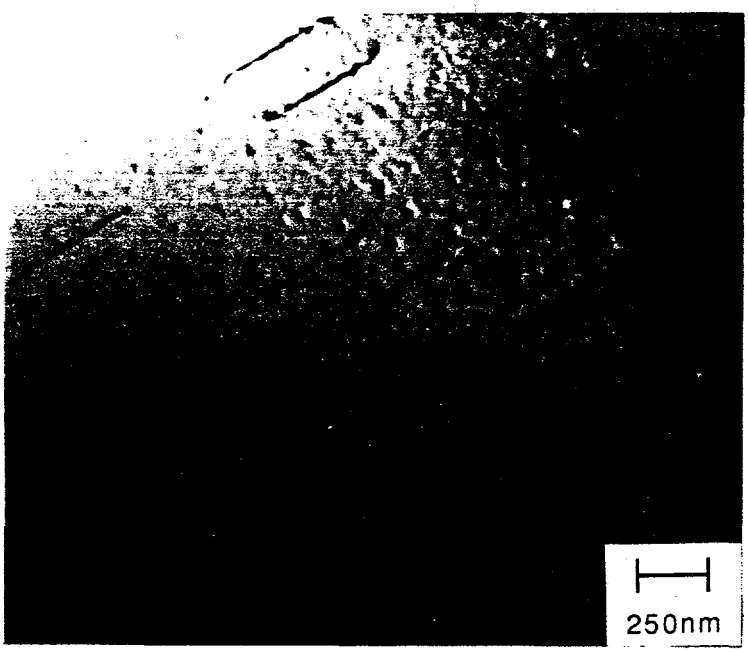

(a)

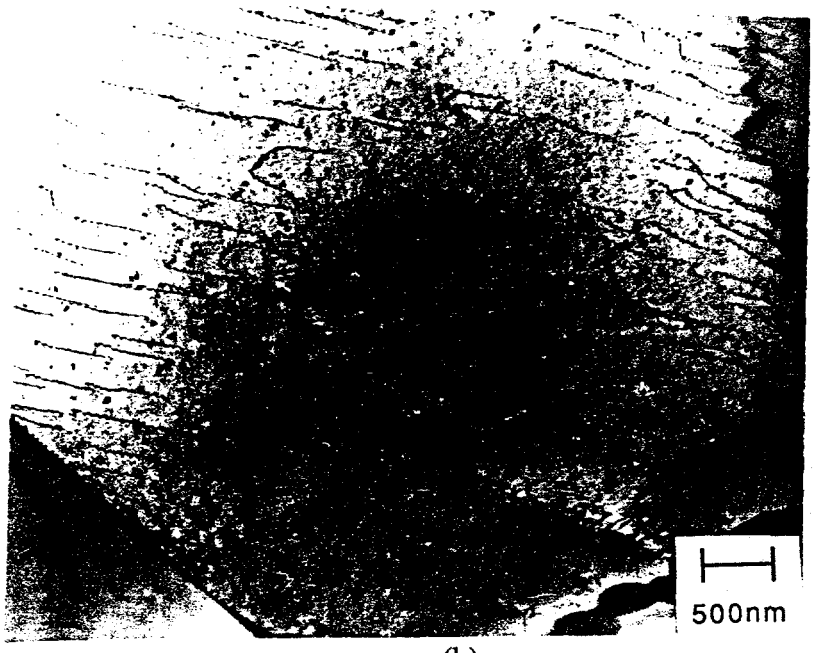

(b)

Fig. 4.48 Dislocation structure of FAP-Y fatigued in air (a) and oxygen (b) at 25°C.

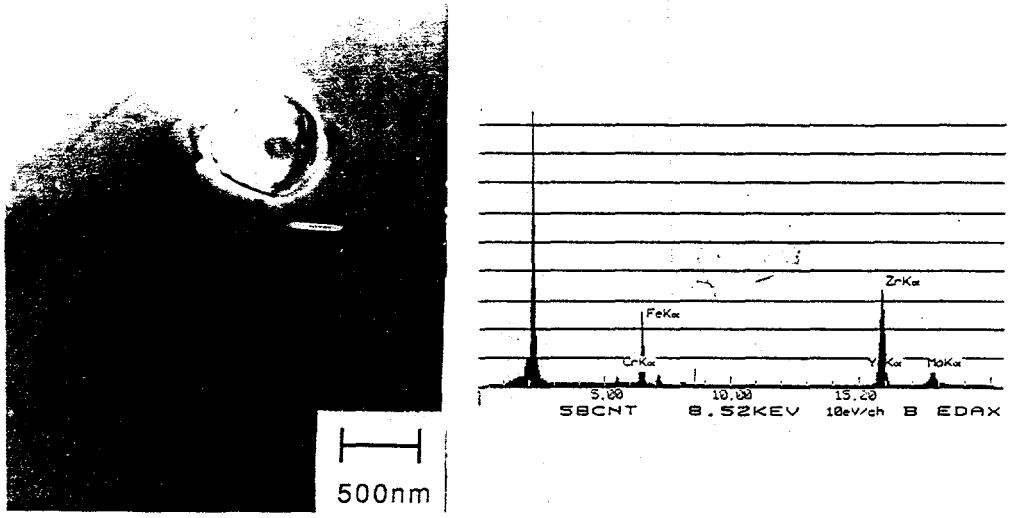

Fig. 4.49 Zr - rich precipitates in FAP-Y fatigued in air at 25°C, with corresponding EDAX pattern.

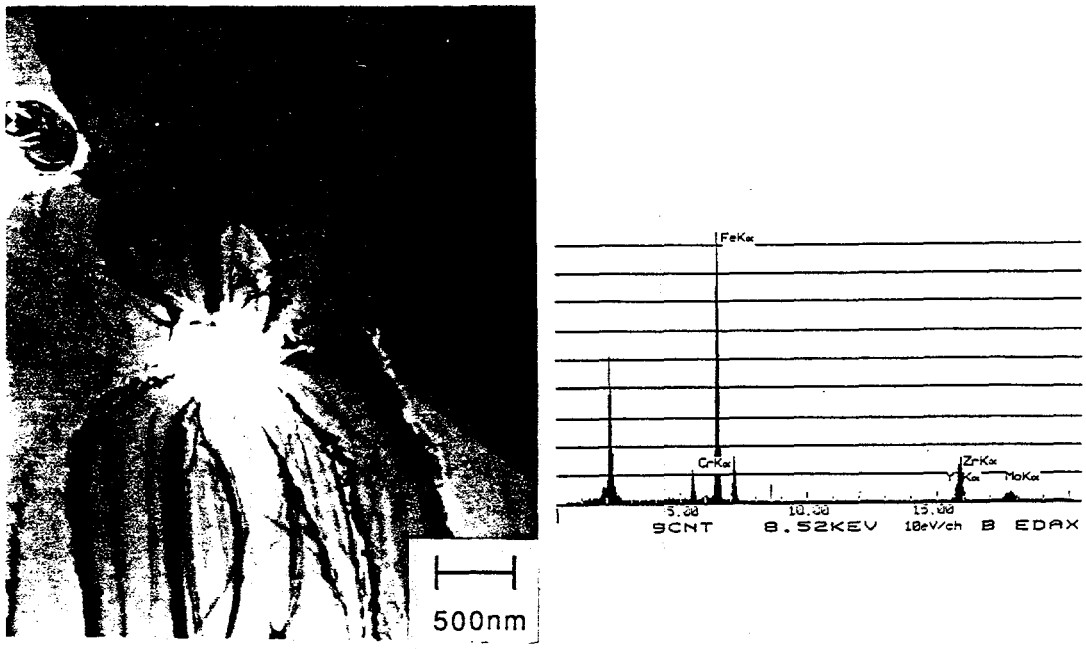

Fig. 4.50 Zr and Cr - rich precipitates in FAP-Y fatigued in air at 25°C, with corresponding EDAX pattern.

5 DISCUSSION

5.1 Plasticity Effects on Crack Growth

The plastic zone radius, R_y, ahead of a fatigue crack under plane-strain conditions has been expressed by Irwin (88) as:

$$R_y = \frac{1}{6\pi}\left(\frac{K_{max}}{\sigma'_{YS}}\right)^2 \qquad \text{Eq. 8}$$

where σ'_{YS} is the cyclic yield stress and is approximated by twice the monotonic yield stress. When measuring fracture toughness, the test specimen dimensions should be large enough that the material is in a state of plane strain, otherwise plasticity effects may alter the measured toughness. ASTM fracture testing standards specify that the thickness of a compact tension specimen, B, should be 50 times the plastic zone radius expected in plane strain, to ensure that the specimen is in predominantly a plane strain condition and that plasticity effects can be neglected. This condition can be expressed as:

$$R_y/B < 0.02 \text{ to satisfy plane strain conditions.} \qquad \text{Eq.9}$$

The plastic zone size and the R_y/B ratio of the fatigued iron-aluminum specimens in air and oxygen were calculated for various values of da/dN and are listed in Table 7. The only alloy which met the plane-strain condition in all cases was FAP-Y. DO_3 ordered FA-129 tested in air at room temperature was in plane-strain as well, but in oxygen or at elevated

TABLE 7
Plastic Zone Calculations

B2 Ordered FA-129

		da/dN=10^{-9} m/cycle			da/dN=10^{-7} m/cycle			da/dN=10^{-6} m/cycle		
Environment	σ'_{YS}	K_{max}	R_y	R_y/B	K_{max}	R_y	R_y/B	K_{max}	R_y	R_y/B
25°C in Air	818	29.0	66	0.012	48.6	187	0.036	59.8	282	0.054
25°C in O_2	880	-	-	-	47.6	154	0.029	71.8	351	0.067
150°C in Air	738	41.4	166	0.031	71.6	497	0.097	-	-	-

DO_3 Ordered FA-129

		da/dN=10^{-9} m/cycle			da/dN=10^{-7} m/cycle			da/dN=10^{-6} m/cycle		
Environment	σ'_{YS}	K_{max}	R_y	R_y/B	K_{max}	R_y	R_y/B	K_{max}	R_y	R_y/B
25°C in Air	990	24.6	32	0.005	34.4	63	0.011	38.6	80	0.014
25°C in O_2	1160	-	-	-	32.0	40	0.006	44.8	78	0.014
150°C in Air	830	37.8	109	0.021	67.2	345	0.067	69.8	373	0.073
450°C in Air	738	29.4	83	0.015	47.8	215	0.042	64.4	401	0.078

FAP-Y

		da/dN=10^{-9} m/cycle			da/dN=10^{-7} m/cycle			da/dN=10^{-6} m/cycle		
Environment	σ'_{YS}	K_{max}	R_y	R_y/B	K_{max}	R_y	R_y/B	K_{max}	R_y	R_y/B
25°C in Air	974	20.0	21	0.004	21.8	25	0.005	23.4	29	0.005
25°C in O_2	996	19.8	20	0.003	22.2	25	0.005	25.6	34	0.006

Fe-35Al

		da/dN=10^{-9} m/cycle			da/dN=10^{-7} m/cycle			da/dN=10^{-6} m/cycle		
Environment	σ'_{YS}	ΔK	R_y	R_y/B	ΔK	R_y	R_y/B	ΔK	R_y	R_y/B
25°C in Air	694*	32.6	115	0.022	49	263	0.050	-	-	-
25°C in O_2	690*	36.8	150	0.029	61.2	416	0.079	65.4	474	0.093

$\sigma'_{YS} = 2\sigma_{YS}$; in MPa

K_{max} in MPa$\sqrt{m}$

$$R_y = \frac{1}{6\pi}\left(\frac{K_{max}}{\sigma'_{YS}}\right)^2; \text{ in } \mu m$$

* From (73)

temperatures, the condition was not met. The tougher B2 ordered FA-129 and Fe-35Al did not meet the plane-strain condition in any condition. In general the plastic-zone size and R_y/B ratio decreases significantly in an air environment versus an oxygen environment, and increases with increasing temperature.

As a result of the failure to meet the ASTM criteria for plane-strain, the crack growth rates and fracture toughness values measured in these tests cannot be precisely compared to those for other alloys in a quantitative manner. However, the degree of plane stress and effect on the fatigue data in this study is presumed to be small because no plasticity was observed in the COD measurements and microhardness measurements did not indicate gross work hardening. In addition, the ASTM criterion is conservative when predicting the onset of plane stress, and increases in the yield stress due to strain hardening were not considered in this analysis. Therefore, it is presumed that the data from fatigue tests at room temperature can be compared among themselves without a large influence of plane stress.

5.2 Effect of Environment

The threshold (stage I) and Paris (stage II) regimes of fatigue crack growth often are affected by environment. An aggressive environment can dramatically decrease the threshold stress intensity and enhance crack nucleation during stage I crack growth. In stage II, an aggressive environment, coupled with the appropriate frequency or mean stress, can influence growth rates and the stage II slope, m, of the Paris equation (Eq. 7). In contrast, it is often noted that there is little influence of environment on Stage III crack propagation rates and the critical stress intensity, K_C. Fatigue crack resistance in stage III is more often found to vary with microstructure, mean stress, and thickness effects.

However, the iron aluminides examined in this study, particularly the ordered FA-129 and Fe-35Al, exhibit a decreased critical stress intensity when fatigued in hydrogen gas and air, compared to that measured in oxygen. In B2 and DO_3 ordered FA-129, the measured K_C was found to decrease by 28% and 31%, respectively, when the environment was changed from oxygen to hydrogen, and a decrease of 20% was noted for alloy Fe-35Al.

While this finding is at odds with data reported for many structural steels, nickel-base superalloys, and aluminum alloys, there have been several studies of environmentally enhanced crack growth in ordered alloys in which the stage III crack growth rates and K_C values are influenced by environment. Kuruvilla (6) found that for an ordered Fe-Ni-V alloy, K_C, as well ΔK_{TH}, increased by almost 100% when the environment was changed from hydrogen to oxygen. An even more pronounced effect was seen in an ordered FeCo-V alloy in hydrogen gas and vacuum environments. Pao et. al. (39) found a similar result for ordered Ni_2Cr fatigued in air and aqueous NaCl environments, where NaCl reduced both K_{TH} and K_C. Several non-ordered high-alloy steels also have been observed to suffer a reduction in K_C in embrittling environments. For example, Brazill et. al. (89) found that in a 2.25Cr-1.0Mo steel (alloy A542) K_C was decreased by 15% between vacuum and hydrogen gas environments. The crack growth rates were also 3 times higher for equivalent stress intensities in hydrogen gas in the high ΔK regime of the fatigue curve.

Fig. 5.1a shows the typical effect of environment on threshold, but not critical crack growth in two non-ordered iron-base alloys: a low alloy austenitic steel in argon and hydrogen (90), and a 4135 steel in air and vacuum (90). Fig. 5.1b shows the effect of environment on both threshold and critical crack growth for the following alloys: Ni_2Cr in an NaCl solution and in air (39), an ordered FeCo-V alloy in hydrogen and vacuum (6), and a 2 1/4 - 1Mo steel in hydrogen and vacuum (89).

The fracture surface appearance of the fatigued test specimens (Table 6) gives a great deal of information regarding the mechanism of hydrogen embrittlement. Both ordered

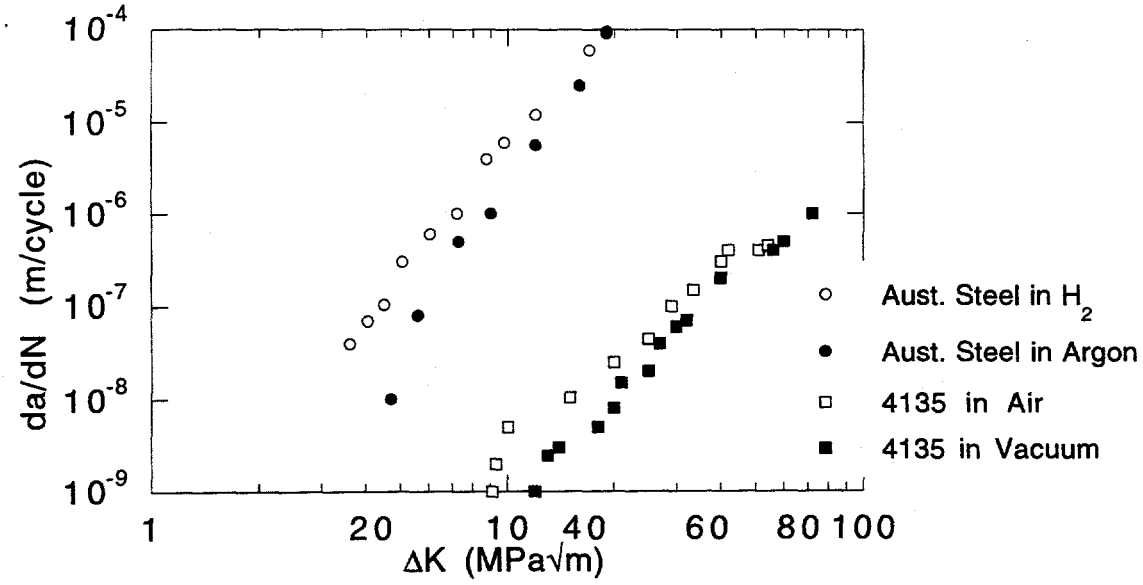

(a)

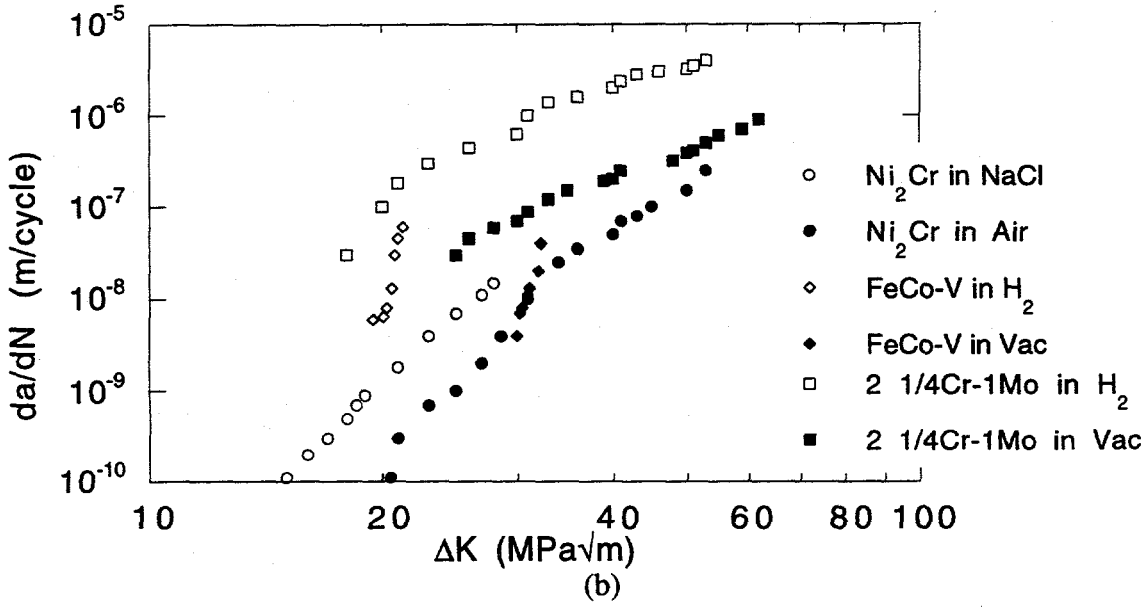

(b)

Fig. 5.1 FCG data which show environmental effect on ΔK_{TH} only (a) and environmental effect on both ΔK_{TH} and ΔK_C (b)

materials (FA-129 and Fe-35Al) exhibited a dimpled transgranular surface when fatigued in oxygen, as is typical for ductile materials. Only the DO_3 ordered FA-129 showed some brittle cleavage faceting in oxygen, which is not unexpected as it has the lowest toughness and RA of all the ordered materials examined.

The fracture surfaces of B2 ordered FA-129, FAP-Y and Fe-35Al remained transgranular in all fatigue tests, with increasing amounts of brittle cleavage as the environment became more aggressive. The shift in fracture surface is especially dramatic for alloy FAP-Y in hydrogen gas (Fig. 4.26) and air (Fig. 4.27). DO_3 ordered FA-129 demonstrated the same trend of increasing degree of cleavage failure with increasing aggressiveness of environment, although some intergranular failure was noted along with the cleavage facets. The effect of hydrogen on cleavage planes is clear: cleavage planes are weakened when exposed to a hydrogen-bearing environment and a decohesion process is likely occurring.

Fracture surfaces observed in tension for alloy FAP-Y indicate action of the hydrogen along cleavage planes as well. As with fatigue crack growth, the shift in tensile fracture surface is dramatic when the environment shifts from air (Fig. 4.7b) to hydrogen (Fig. 4.7c). The effect of hydrogen on cleavage planes is not limited by long range order, as the disordered alloy FAP-Y as well as the B2 and DO_3 ordered FA-129, are all prone to cleavage failure in the presence of hydrogen. However, the cleavage faceting in the presence of hydrogen is clearly most severe in FAP-Y.

The onset of limited intergranular failure at low stress intensities in DO_3 ordered FA-129 is interesting, as most studies of environmental embrittlement in iron aluminides under monotonic tension (See Appendix A) report no effect of hydrogen on fracture path for iron-aluminum alloys containing less than 35%Al, or, for alloys with >35%Al, a shift from intergranular failure in inert environments to transgranular cleavage in aggressive

environments. These results indicate that cleavage decohesion is not the only mechanism acting to embrittle iron aluminides, but that intergranular decohesion may also play a role in fatigue loading. The disappearance of the intergranular facets at high growth rates indicates that there is a rate effect in the embrittlement process

The intergranular decohesion mechanism is not significant in tensile loading or fatigue crack growth at high stress intensities and growth rates, possibly because it requires a minimum length of time to deliver the sufficient hydrogen to the grain boundaries to activate this mechanism. With a hydrogen dislocation-transport mechanism active, dislocations moving in a planar manner along slip planes may act to deliver high concentrations of hydrogen to the grain interiors and cleavage planes. As demonstrated by the calculations of transport distances of section 5.3, this phenomenon can occur within the time available over a single fatigue cycle. Because the bulk diffusion coefficient is very low, hydrogen may not have time to diffuse from the slip planes where it accumulates to grain boundaries in the time available for one fatigue cycle.

It is noteworthy also that intergranular failure in fatigue was seen only in DO_3 ordered FA-129 and not in B2 ordered FA-129. The only differences between these two materials caused by the differing crystal structures are the dislocation density, slip behavior, and bulk diffusion rates. One explanation may be that the greater dislocation mobility of the B2 ordered FA-129 is responsible for relieving internal stresses at grain boundaries. Such stresses in conjunction with hydrogen can cause premature failure at the grain boundaries. The TEM analysis clearly showed that when fatigued at room temperature in oxygen, air, or hydrogen gas the dislocation density was much lower in DO_3 ordered FA-129 than B2 ordered FA-129, and that the dislocations in the DO_3 state were much more likely to be paired superlattice dislocations. Several researchers (55, 58) have noted that superlattice dislocations nucleated in a DO_3 ordered lattice at room temperature require a large amount of energy to form, compared to ordinary dislocations. Plastic flow occurs by motion of

ordinary dislocations even though a higher resolved shear stress is required to move the ordinary dislocations than superlattice dislocations. This effect is discussed further in section 5.4.

One feature of the fracture surface which appears only in the hydrogen and air environments is a step-like nature to the cleavage facets seen in DO_3 ordered FA-129 and Fe-35Al (Figs. 4.38b and 4.40). These may be indicative of a dislocation-assisted hydrogen transport mechanism. In the ordered alloys, especially in the DO_3 condition, the superlattice dislocations generally are confined to their slip plane. If one of the pair of superlattice dislocations begins to cross slip onto an intersecting slip plane it will become immobile at the slip plane intersection. The same thing can happen if two superdislocations on intersecting slip plane interfere with one another at the slip plane intersection. This results in dislocation pile-ups at the slip plane intersections, and if the dislocations are transporting hydrogen, the hydrogen concentration will increase at these intersections and the latter will be weak points for fracture. The step-like facets observed in Figs. 4.38b and 4.40, and in other alloys such as Ni_2Cr (39), may be attributed to the dislocation-transport mechanism. This is likely the case for DO_3 ordered FA-129 and Fe-35Al as these step-like patterns were observed only in the embrittling air and hydrogen environments.

5.3 Frequency Effects

The increase of FCG rates in hydrogen embrittling environments over that measured in an inert environment, or the term $(da/dN)_{cf}$ in Eq. 2, is expected to be proportional to the amount of atomic hydrogen produced by chemical reactions at the freshly fractured surface each cycle. In this discussion it will be assumed that there is no stress corrosion cracking contribution, $(da/dN)_{scc}$, to the overall fatigue crack growth rate of iron aluminides in air at

room temperature. Time dependent crack growth under a static load has not been reported in the literature in these, or similar, Fe-Al alloys in air at room temperature.

The amount of hydrogen produced at the fresh fracture surface, in turn, is proportional to the new surface area produced during the previous cycle, or $2\Delta aB\alpha$, where Δa is the crack growth increment, B is the specimen thickness, and α is a constant to account for increased surface area due to roughness. In iron aluminides in moisture-bearing environments, the reaction is an oxidation reaction of the type H_2O + Al or H_2O+Fe. In hydrogen gas environments, the reaction is simply the dissociation of molecular hydrogen to atomic hydrogen. The rate at which either reaction occurs may be a limiting factor in the degree of embrittlement.

The amount of hydrogen produced at the crack tip also is dependent on the rate of transport of the embrittling species to the surface. If the transport rate to the surface is very slow, then the amount of hydrogen produced by the chemical reaction will be limited by the availability of the necessary reactants.

Wei et. al. (91) derived a set of criteria for determining whether environmentally enhanced crack growth is reaction rate or transport rate limited. This limiting effect applies only to the term $(da/dN)_{cf}$ of Eq. 2. Their calculations are based on maintaining complete surface coverage of the freshly exposed surface by the embrittling species.

In transport control the surface coverage is found to increase linearly with time available per cycle, or 1/(2xfrequency), and will be limiting at high frequencies when the surface reactions occur much more rapidly than fresh reactants can be brought to the surface. Hence, a significant number of possible sites for hydrogen generation are not utilized. In reaction control the surface coverage varies exponentially with available reaction time and reaction rate coefficient, k_c, and is rate limiting when fresh reactants are delivered much faster to the surface than can be consumed by oxidation or dissociation, and adsorption. Each of these scenarios assumes that once adsorbed, the hydrogen is quickly

transported into the plastic zone ahead of the crack. The equations derived for the corrosion fatigue term of da/dN for transport control and reaction rate control are given by Eqs. 10 a and b, respectively.

$$(da/dN)_{cf} \alpha \frac{F}{S N_o R T} \frac{p_o}{2f} (da/dN)_e \qquad \text{Eq. 10a)}$$

$$(da/dN)_{cf} \alpha \left[1 - \exp\left(\frac{-k_c p_o}{2f}\right)\right] (da/dN)_e \qquad \text{Eq. 10b)}$$

F is a flow parameter dependent on material properties and the test temperature, S is the freshly created fracture surface, N_o is the number of available reaction sites at the fracture surface, R is the gas constant, p_o is the partial pressure of the embrittling species (in this case the partial pressure of water vapor in laboratory air), and f is the test frequency.

If transport rate is rate limiting, then a plot of :

$$\frac{(da/dN)_{cf}}{(da/dN)_e} \text{ vs. } \frac{1}{2f} \qquad \text{Eq. 11}$$

should result in a straight line, as all other coefficients in Eq. 10a) are constant for a given material and test temperature. If, on the other hand, the rate of the surface chemical reaction is rate limiting, then a plot of Eq. 11 would result in a decaying exponential curve, with the decay rate given by $-k_c p_o$.

The crack growth data measured for B2 ordered FA-129 at room temperature in air has been broken down into its purely mechanical component, $(da/dN)_r$, and fatigue corrosion component, $(da/dN)_{cf}$. This was accomplished by utilizing Eq. 2, and assuming that $(da/dN)_r$ is independent of frequency and is given by the total da/dN response in the inert

oxygen environment, and by assuming that $(da/dN)_{scc}$ is zero. These data at frequencies of 0.08Hz to 20Hz are tabulated in Table 8.

Fig. 5.2 shows the plot of Eq. 11 and shows clearly that $(da/dN)_{cf}$ / $(da/dN)_e$ is not linearly related to 1/2f, and therefore transport control is not active. To determine if reaction rate control is occurring a least square fit of Eq. 10b was attempted, shown in Fig. 5.2. The fit was quite poor ($R^2 = 0.682$) and the term $-k_c\ p_o$ was found to be -26.9 $(sec)^{-1}$. The partial pressure of water vapor in laboratory air at room temperature is approximately 1000Pa, and the measured value of the reaction rate constant, k_c is 0.0269 $(Pa\text{-}sec)^{-1}$. This is a very high value for k_c compared to other systems in which reaction control is active. For example, Brazill, Simmons and Wei (89) found k_c to be $2.3x10^{-6}$ $(Pa\text{-}sec)^{-1}$ for the oxidation of steel in laboratory air at room temperature. The poor exponential curve fit and high reaction rate constant determined from the best fit of the data indicate that reaction rate control is not active.

Another explanation for the effect of frequency on embrittlement is the increased time for transport of hydrogen into the plastic zone ahead of the crack tip. Iron aluminides have been shown to be extremely sensitive to very small amounts of water vapor and hydrogen in tensile tests (35). It can be expected that the degree of embrittlement in fatigue will, therefore, be strongly affected by the hydrogen concentration in the embrittled region.

Kasul and Heldt (34) have shown that when iron aluminides are cathodically charged with hydrogen, there is a very strong dependence of ductility loss on charging time, especially for times of 10 minutes or less, see Fig. 5.3. The diffusion coefficient of hydrogen in the Fe_3Al lattice is very low, and was measured by Lynch and Heldt (64) to be $4x10^{-12}$ cm^2/sec. Such a low diffusion rate of hydrogen in the lattice compared to hydrogen in steel, in which the diffusion coefficient of hydrogen is between 10^{-5} and 10^{-6} cm^2/sec, will undoubtedly magnify the frequency and time dependence of hydrogen-enhanced fatigue crack growth, as is the case with cathodically charged Fe-35Al tested in tension.

TABLE 8
Effect of Frequency on $(da/dN)_e$ and $(da/dN)_{cf}$ in B2
Ordered FA-129 Fatigued in Air at 25°C

$\Delta K = 21$ MPa$\sqrt{m}$

	20Hz	2 Hz	0.2Hz	0.08Hz
$(da/dN)_e$	2.3×10^{-8}	5.8×10^{-8}	1.7×10^{-7}	2.6×10^{-7}
$(da/dN)_{cf}$	1.3×10^{-8}	4.8×10^{-8}	1.6×10^{-7}	2.5×10^{-7}

$\Delta K = 23$ MPa$\sqrt{m}$

	20Hz	2 Hz	0.2Hz	0.08Hz
$(da/dN)_e$	5.0×10^{-8}	1.2×10^{-7}	3.3×10^{-7}	5.3×10^{-7}
$(da/dN)_{cf}$	3×10^{-8}	9.6×10^{-8}	3.1×10^{-7}	5.1×10^{-7}

$\Delta K = 25$ MPa$\sqrt{m}$

	20Hz	2 Hz	0.2Hz	0.08Hz
$(da/dN)_e$	1.0×10^{-7}	2.7×10^{-7}	8.1×10^{-7}	1.6×10^{-6}
$(da/dN)_{cf}$	7.0×10^{-8}	2.4×10^{-7}	7.8×10^{-7}	1.3×10^{-6}

$\Delta K = 27$ MPa$\sqrt{m}$

	20Hz	2 Hz	0.2Hz	0.08Hz
$(da/dN)_e$	2.5×10^{-7}	7.4×10^{-7}	-	-
$(da/dN)_{cf}$	2.0×10^{-7}	6.9×10^{-7}	-	-

da/dN in m/cycle

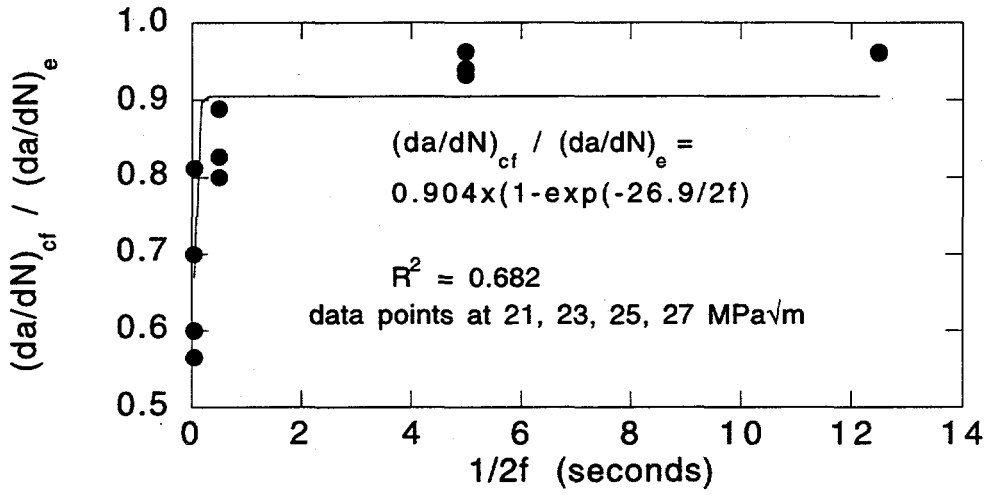

Fig. 5.2 Ratio of corrosion-fatigue component of crack growth rate to total crack growth rate as a function of frequency.

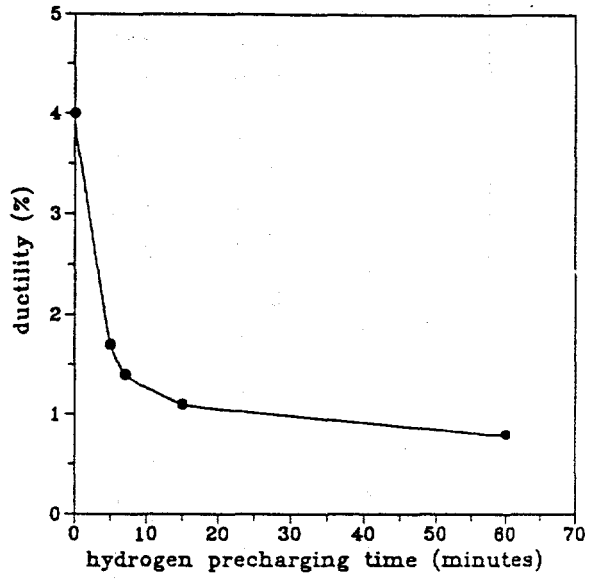

Fig. 5.3 Effect of charging time on ductility loss in Fe-24.6Al (34).

If the corrosion-fatigue crack growth rate $(da/dN)_{cf}$ truly reflects a synergistic combination of applied stress intensity and exposure to an embrittling environment, then this term should incorporate both a stress intensity term and some measure of the exposure to hydrogen. In the case of bulk-transport limited embrittlement the environmental term may involve the penetration depth of hydrogen ahead of the crack tip. Corrosion fatigue may then be expressed by Eq. 12a. The total crack growth rate in an embrittling hydrogen-bearing environment is then expressed by Eq. 12b, assuming that $(da/dN)_{scc}$ is zero. When the fatigue crack growth in the inert environment can be modeled by the Paris law, then the term $(da/dN)_r$ is expressed by $A_o\Delta K^{m_o}$, and the total crack growth rate, $(da/dN)_e$, is expressed by Eq. 12c.

$$\left(\frac{da}{dN}\right)_{cf} = A\,\Delta K^{m}\, r^{n} \qquad \text{Eq. 12a}$$

$$\left(\frac{da}{dN}\right)_{e} = \left(\frac{da}{dN}\right)_{r} + A\,\Delta K^{m}\, r^{n} \qquad \text{Eq. 12b}$$

$$\left(\frac{da}{dN}\right)_{e} = A_o\Delta K^{m_o} + A\,\Delta K^{m}\, r^{n} \qquad \text{Eq. 12c}$$

In Eqs. 12a-c, r is the penetration depth of hydrogen ahead of the crack. In the case of diffusional transport, r will be a function of the normalized hydrogen concentration, C/Co, where C is the local hydrogen concentration and Co is the hydrogen concentration at the crack tip. The term A is a constant. Eq. 12 indicates no embrittlement if either the applied stress intensity is zero or the internal hydrogen concentration is zero. Eq. 12 also reflects the frequency effect in the penetration depth term, as the penetration depth over one cycle will increase as the frequency decreases.

Assuming only bulk hydrogen diffusion, the equation describing the hydrogen concentration in the crack plane as a function of distance ahead of a propagating crack is given by (64)

$$\frac{C}{C_o} = \frac{K_o\left(\frac{Vr}{2D}\right)\exp\left(\frac{-Vr}{2D}\right)}{K_o\left(\frac{Vr_o}{2D}\right)\exp\left(\frac{-Vr_o}{2D}\right)} \qquad \text{Eq. 13}$$

where K_o is a second order hyperbolic Bessel function and r_o is the crack tip radius.

Using Eq. 13, r was calculated for at each test frequency at ΔK=21, 23, 25, and 27 MPa$\sqrt{m}$. These penetration depths are listed in Table 9. The crack tip radius was taken to be 10^{-9}m. Because embrittlement has been shown to occur at very low hydrogen and air concentrations, C/Co was chosen to be the lowest value which would still have a significant effect on the penetration depth. This corresponds to a value of 0.01 for C/Co. Taking values of concentration ratios smaller than 0.01 has negligible effect on the penetration distance. The diffusion coefficient of $4x10^{-12}$ cm^2/sec measured by Lynch and Heldt (64) was used, and the values of $(da/dN)_e$ are those listed in Table 8.

The penetration distances listed in Table 9 are extremely short compared to the plastic zone sizes calculated in Table 8, ranging from 5 to 560Å. It is very likely that an enhanced transport mechanism such as dislocation-assisted transport will provide for deeper penetration of hydrogen than random-walk diffusion, and therefore the latter type of diffusion is not likely to be the cause for the observed frequency dependence of enhanced crack growth.

TABLE 9
Penetration depth of hydrogen due to diffusion at a concentration ratio C/Co of 0.01 in B2 ordered FA-129 at room temperature

	Penetration Depth in meters			
ΔK MPa$\sqrt{m}$	20 Hz	2 Hz	0.2 Hz	0.08 Hz
21	3.2×10^{-9}	1.1×10^{-8}	4.0×10^{-8}	5.6×10^{-8}
23	1.6×10^{-9}	5.7×10^{-9}	1.9×10^{-8}	3.0×10^{-8}
25	1.0×10^{-9}	2.7×10^{-9}	8.2×10^{-9}	1.1×10^{-8}
27	5.0×10^{-10}	1.4×10^{-9}	-	-

Dislocation-assisted transport is a phenomenon which has been observed in a number of materials and is responsible for penetration of hydrogen much further than would be expected from diffusion (92, 93, 94, 95)). A hydrogen atmosphere develops about a dislocation generated near the crack tip and as the dislocation travels away from the tip, it drags the hydrogen with it through the lattice. The penetration distance of hydrogen ahead of the crack tip is equal to the dislocation velocity times the time available per cycle, or V/2f. One model, proposed by Tien and Richards (92), predicts the maximum possible dislocation velocity that can be achieved before the hydrogen atmosphere is stripped from the dislocation. The maximum dislocation velocity can be used to determine the maximum penetration distance that can be accounted for by dislocation assisted transport. Tien and Richards expressed the maximum penetration, r_{max}, as

$$r_{max} = V_{max}\, t = \frac{D}{kT}\,\frac{E}{30b}\,\frac{1}{2f} \qquad \text{Eq. 14}$$

where E is the binding energy of hydrogen to the dislocation and is approximately 0.3eV, k is the Boltzman constant, and b is the Burgers vector (3Å for B2 ordered FA-129). The maximum penetration depth due to dislocation transport calculated from Eq. 14 for B2 ordered FA-129 is tabulated in Table 10 for frequencies from 20 to 0.08 Hz. The values of

r_{max} in Table 10 are several orders of magnitude larger than the penetration depths due to diffusion calculated in Table 9, and range from 129Å to 3μm. These depths reported in Table 10 are more realistic estimates of the hydrogen penetration into the surface.

TABLE 10
Penetration depth of hydrogen due to dislocation transport in B2 ordered FA-129 at room temperature

Frequency (Hz)	r_{max} (m)
20	1.29×10^{-8}
2	1.29×10^{-7}
0.2	1.29×10^{-6}
0.08	3.24×10^{-6}

Eq. 12 can be rearranged to yield the following:

$$\mathrm{Log}\left(\frac{da}{dN}\right)_{cf} = \mathrm{Log}(A) + m\,\mathrm{Log}(\Delta K) + n\,\mathrm{Log}(r) \qquad \text{Eq. 15}$$

If Eqs. 12 and 15 are accurate representations of $(da/dN)_{cf}$, then according to Eq. 15 a plot of $\mathrm{Log}(da/dN)_{cf}$ vs. $\mathrm{Log}(r_{max})$ at a constant ΔK should yield a straight line with the intercept given by $\mathrm{Log}(A)+m\,\mathrm{Log}(\Delta K)$ and a slope of n. These plots for ΔK=21, 23, 25, and 27 MPa$\sqrt{m}$ are shown in Fig. 5.4. The correlation is excellent, and from a least squares curve fit the exponent n of Eq. 12 is found to be 0.52.

In order to find the values of A and m, Eq. 12 is manipulated into the following form:

$$\mathrm{Log}\left[\frac{\left(\frac{da}{dN}\right)_{cf}}{r_{max}^{0.52}}\right] = \mathrm{Log}(A) + m\,\mathrm{Log}(\Delta K) \qquad \text{Eq. 16}$$

Eq. 16 is plotted for all values of ΔK and frequencies in Fig. 5.5. The validity of Eq. 12 is clear as the $(da/dN)_{cf}$ vs. ΔK curves at various frequencies can be collapsed onto a single frequency-modified curve as seen in Fig. 5.5. The values of A and m of Eq. 12 are calculated from a least-square curve fit of the data in Fig. 5.5, and are $A=3.78x10^{-18}$ and $m=10.31$.

As a further check, a plot of $(da/dN)_{cf}$ vs. $(r_{max})^{0.52}$ should result in a straight line for each applied stress intensity. This plot is shown in Fig. 5.6 and again the correlation is excellent, especially for such data on a linear axis representation. The excellent correlation of the fatigue data to Eq. 12, as seen in Figs. 5.4-5.6, indicate that in B2 ordered FA-129 fatigued at room temperature, hydrogen moves into the lattice ahead of the crack tip by a dislocation-assisted transport mechanism.

The physical meaning of the exponent n in Eq. 12 must be related to the quantity of hydrogen dislocations carry into the plastic zone, and the concentration of hydrogen required to enhance the crack growth rate. For example, it is likely that the exponent n will scale with the quantity of hydrogen each dislocation is capable of dragging with it, or the density of dislocations capable of dragging hydrogen atoms, or both. With this in mind, it is therefore very significant that the exponent n was found to be a constant with respect to frequency and applied stress intensity.

Another possibility is that the exponent n describes the efficiency of the dislocation-transport process. Before the hydrogen-bearing dislocations can reach a depth of r_{max}, the hydrogen atoms may be stripped away at a trap. Also, the dislocation may become caught in a pile-up and experience a back stress which would prevent it from reaching r_{max}. Dislocations may travel out of plane also, which would reduce the depth ahead of the crack tip. The exponent n therefore will describe the distribution of penetration depths of the

hydrogen-bearing dislocations and may relate the maximum theoretical penetration depth to the average actual penetration depth.

Even though the degree of embrittlement increased dramatically with frequency, the exponent n was unchanged, signifying that embrittlement does little to change the mobility, ease of dislocation generation, or hydrogen carrying capability of dislocations. Therefore, any hydrogen-metal interaction involving a change in dislocation mobility, such as hydrogen enhanced plasticity or inhibited dislocation motion in the presence of hydrogen, can be ruled out in B2 ordered FA-129 if the preceding assumptions are valid.

TEM analysis shows a clear effect of embrittlement on dislocation density. When fatigued in hydrogen gas and air versus oxygen the dislocation density of B2 ordered FA-129 decreased. This decrease in dislocation density is, therefore, a secondary effect of premature failure due to some other hydrogen-metal interaction. Study of the fracture surfaces of this material indicates a decohesion mechanism along cleavage planes. Premature failure along cleavage planes in the vicinity of the crack tip prior to extensive plasticity away from the crack tip would account for the overall decrease in dislocation density, but is still consistent with the notion that uninhibited dislocations are transporting hydrogen to these cleavage planes. It must be stressed that distance from the foil center to the fracture surface is approximately 125μm, which is much larger than the 0.01μm - 3μm penetration depth calculated for dislocation assisted hydrogen transport. Also, this distance is completely outside the calculated plastic zone for alloys FAP-Y and DO_3 ordered FA-129 fatigued at room temperature. For the other alloys and conditions, the 125 μm distance is outside the calculated plastic zone over part of the fatigue test. The plastic zone sizes calculated in Table 7 are expected to be quite conservative, so it cannot be assumed that the foils lie within the plastic zone for any testing condition. Therefore, the TEM analysis in this study cannot distinguish between reduced dislocation density as a direct result of

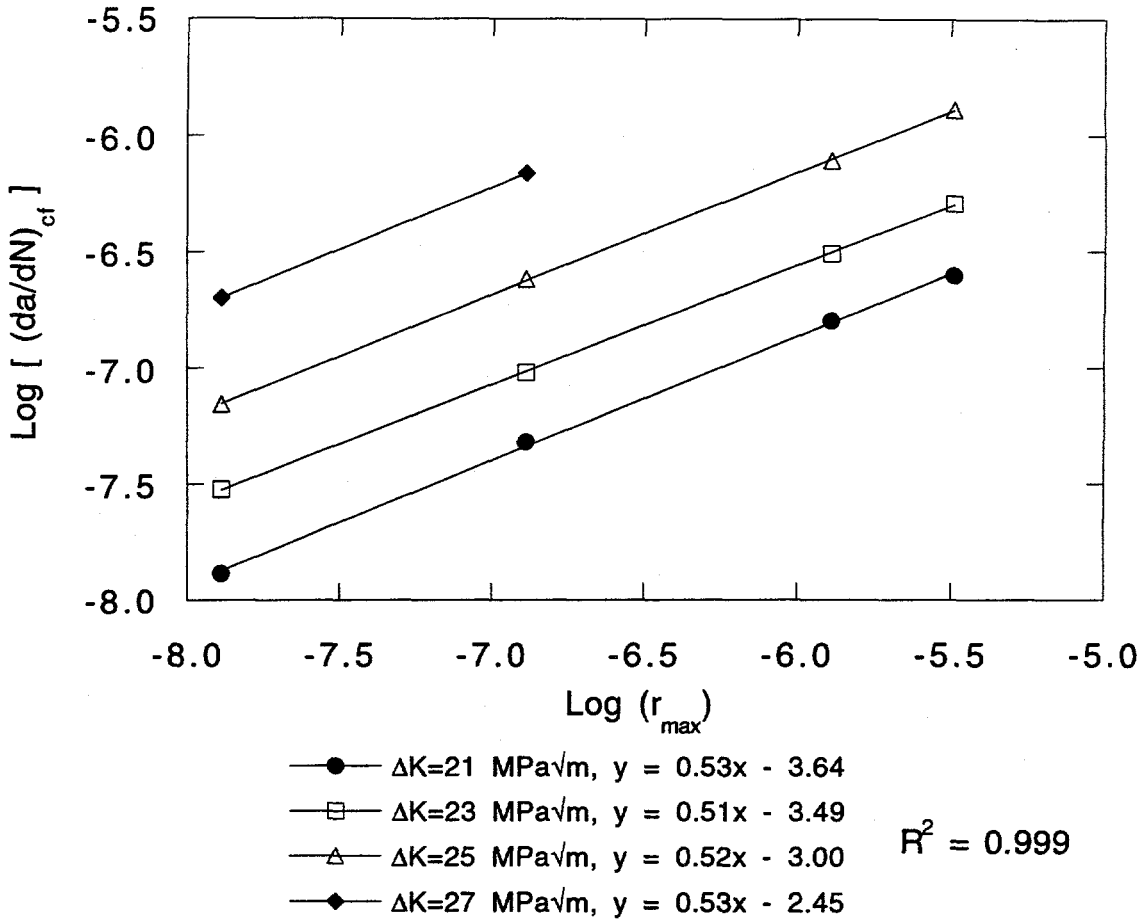

Fig. 5.4 Log - Log plot of $(da/dN)_{cf}$ vs. hydrogen penetration depth due to dislocation transport in B2 ordered FA-129 fatigued in air at 25°C.

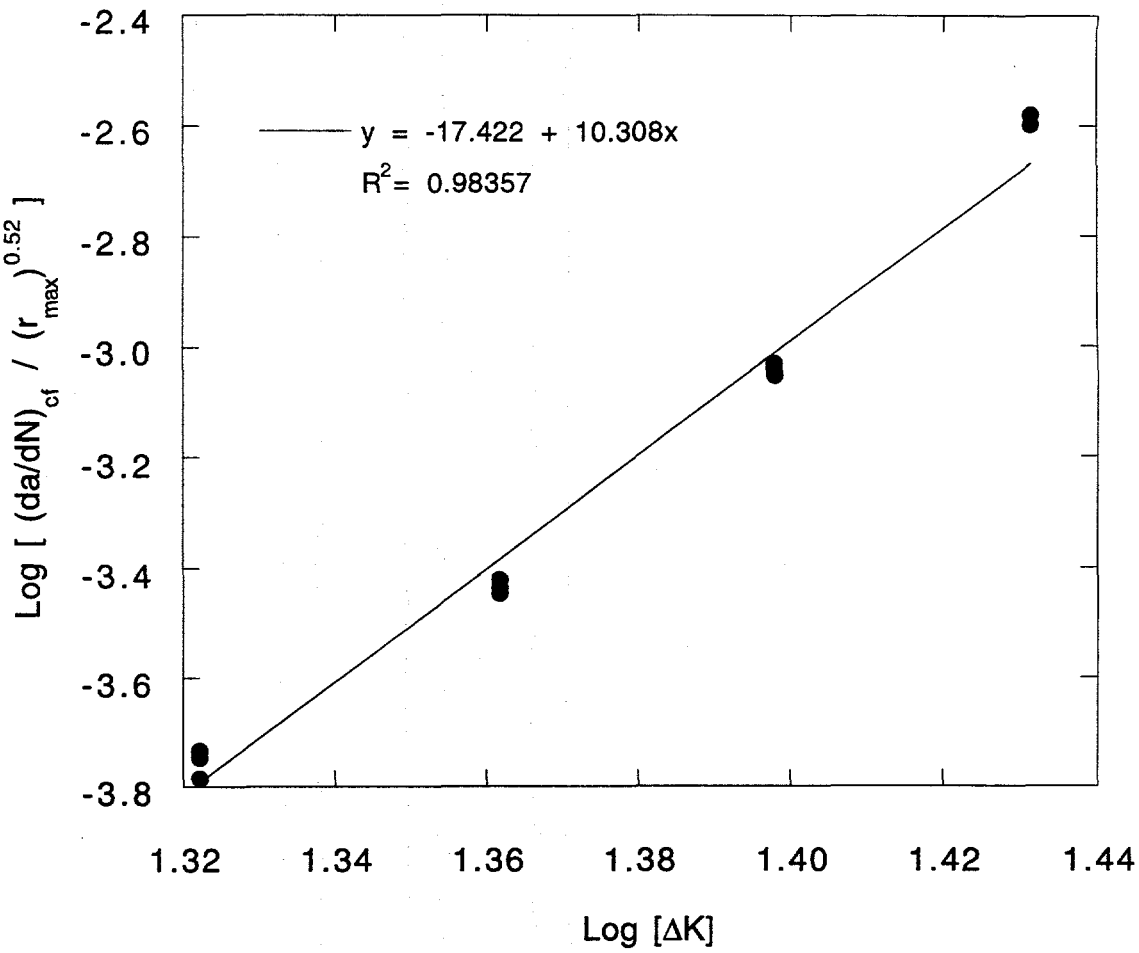

Fig. 5.5 Log - Log plot of ratio of $(da/dN)_{cf}$ to hydrogen penetration depth due to dislocation transport vs. applied stress intensity in B2 ordered FA-129 fatigued in air at 25°C.

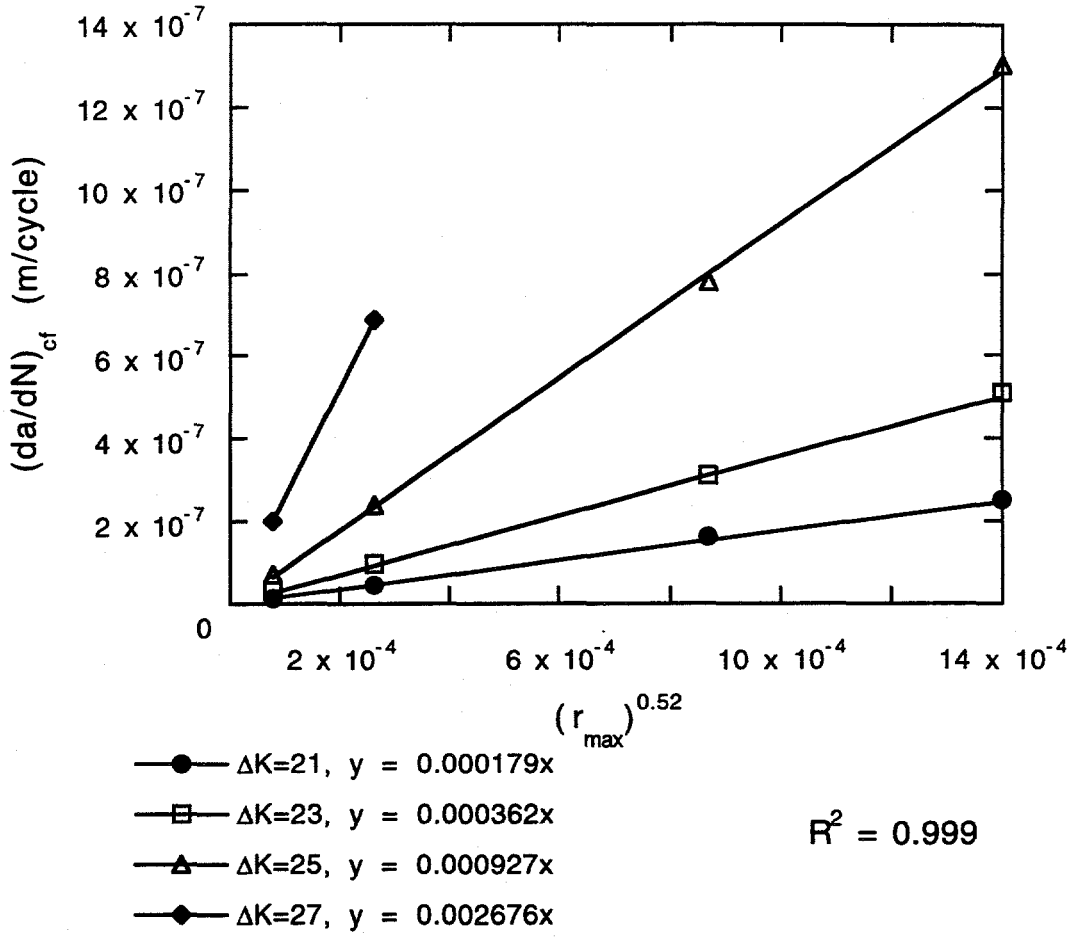

Fig. 5.6 $(da/dN)_{cf}$ vs. hydrogen penetration depth raised to the 0.52 power in B2 ordered FA-129 fatigued in air at 25°C.

hydrogen - dislocation interaction and reduced dislocation density as a secondary result of other hydrogen-metal interactions.

The theory proposed in this section on dislocation transport and frequency effects depend on the assumption that crack growth is continuous, and does not occur in a step-wise fashion. The only possible indication of discontinuous crack growth observed in this work are the occasional fatigue striations which are spaced further apart than the measured value of da/dN Figs. 4.29a and 4.32b). However, other researchers have observed similar widely-spaced striations while confirming that crack growth occurs in a continuous manner. For example, Lynch (96) observed fatigue striations in an aluminum alloy tested in argon which had a one-per-cycle spacing. When the same alloy was tested in moist air the spacing became approximately one-per-10 cycles, and the striations were very similar to those seen in Fig. 4.32b. Lynch confirmed that in both cases crack growth was continuous. As will be mentioned in the future work section of chapter 6, continuous crack growth should be confirmed for the alloys examined in this study.

5.4 Effect of Order and Composition

The susceptibility to hydrogen embrittlement by contact with H_2O-bearing air is clearly dependent on the aluminum concentration. FAP-Y suffered no loss of RA when tested in tension in air, compared to testing in oxygen. However, both ordered conditions of FA-129 were severely embrittled by the air. Even though alloy FAP-Y was not affected by moisture in tension and only somewhat affected by moisture in fatigue, it suffered extreme embrittlement in hydrogen gas under both tension and fatigue. The amount of hydrogen produced by the Al-H_2O reaction of Eq. 1 is likely to be dependent on the concentration of

aluminum at the surface of a tensile specimen, or on the freshly exposed crack tip of a fatigue specimen. Low aluminum alloys therefore produce less hydrogen in moisture-bearing environments are either not embrittled (FAP-Y under tension in air), or are only somewhat embrittled (FAP-Y fatigued in air).

The low-aluminum alloy FAP-Y exhibited by far the worst FCG resistance at room temperature in any environment of all the alloys studied. One possible explanation for the low threshold stress intensity of alloy FAP-Y compared to the high aluminum alloys may be the high degree of recrystallization compared to alloy FA-129. Increasing grain size and reducing the number of grain boundaries tends to increase ΔK_{TH} (97). However, this does not explain the K_{TH} measured in Fe-35Al which is similar to that of FA-129. Fe-35Al has a grain size much larger than either FAP-Y or FA-129.

A more likely explanation is that the disordered nature of FAP-Y allows higher dislocation densities to form. The ordered iron aluminides typically have much lower dislocation densities and the stresses required to move them are higher. While this feature makes for low ductility and RA in a tensile test, it often results in a higher cyclic threshold stress intensity for crack propagation, as an active dislocation source is required for the formation of slip bands and highly deformed regions ahead of a notch which are the precursors to a sharp, propagating crack. As seen in Fig. 5.7, the threshold stress intensities of the iron aluminides in this study are much higher than that for many other disordered structural alloys. The same can be said for a number of other intermetallic compounds, such as $(FeNi)_3V$ and FeCo-V (6).

However, this still does not explain why alloy FAP-Y behaves poorly at higher stress intensities, when the greater dislocation density and mobility become an asset in resisting FCG. Once a crack is propagating, a large degree of plastic deformation will increase the plastic zone ahead of a crack tip and thereby increase the work necessary to propagate the crack. This effect is seen Fig. 5.7 where the da/dN vs. ΔK curves for several alloys which

had low values for ΔK_{TH} intersect and then fall below the curve for B2 ordered FA-129, resulting in a higher K_C.

5.4.1 Comparison to FCG Resistance in Other Alloys

The iron-aluminides examined in this study all displayed good resistance to initiation of fatigue cracks; however, crack growth rates quickly increased and the slopes of the da/dN-ΔK curves were often much steeper than those of other structural iron-based alloys. Fatigue crack growth resistance of a number of iron alloys was surveyed, and the fatigue crack growth curves of several typical alloys are plotted, together with data from this work, in Fig. 5.7. The data shown in Fig. 5.7 were chosen with R ratios and frequencies as close as possible to those used in this work (R=0.5, frequency = 20Hz). The threshold stress intensity measured in B2 ordered FA-129 is similar to that seen in the highly resistant En 52 alloy, and much higher than that of the 9 1/4 Cr - 1Mo and low alloy ferritic steel. Even the 16%Al alloy FAP-Y, which was much less tough than FA-129 or Fe-35Al, compared favorably to most alloys at low stress intensities. However, the iron aluminides performed much worse at higher stress intensities. The da/dN-ΔK curve for B2 ordered FA-129 appeared to intersect the da/dN-ΔK curves of all of the other iron-base alloys at da/dN values of 1-5 $x10^{-8}$ m/cycle and stress intensity ranges of 17-21 MPa$\sqrt{m}$. At growth rates and stress intensities above these values, B2 ordered FA-129 performed much worse. The same is true for alloy Fe-35Al (not shown in Fig. 5.7) which had a da/dN-ΔK curve similar to that of B2 ordered FA-129. Alloy FAP-Y is also seen to exhibit moderate resistance to fatigue crack initiation. Its ΔK_{TH} of 10.0 MPa$\sqrt{m}$ is more than twice that of 9 1/4 Cr - 1Mo and low alloy ferritic steel, but the crack growth rate increases so quickly that the stress intensity range required to achieve a crack growth rate of 10^{-7}m/cycle in FAP-Y 10.5 MPa$\sqrt{m}$ compared to 25 MPa$\sqrt{m}$ in the ferritic steel, see Fig. 4.21.

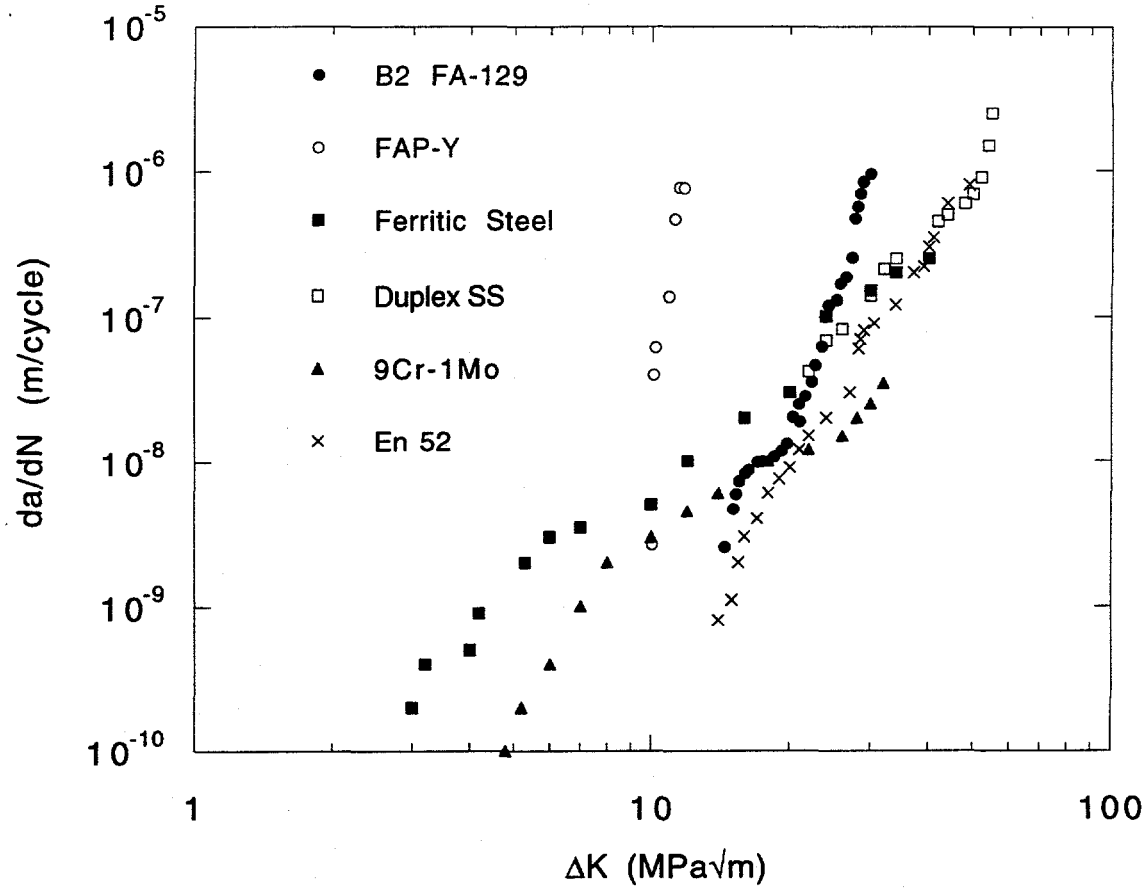

Ferritic Steel: (98)	Composition = 0.09%C, 0.38%Si, 1.46%Mn, 0.02%Cr, 0.25%Ni, 0.03%V, 0.025%Nb, balance Fe R=0.50 freq.=50Hz env.=25°C air GS= *
Duplex SS: (46)	Composition = 24.04%Cr, 6.83%Ni, 3.77%Mo, 0.77%Mn, 0.62%Cu, 0.63%W, 0.17%Si, 0.024%C, balance Fe R=0.50 freq.=5Hz env.=25°C argon GS= 40μm
9 Cr - 1Mo (99)	Composition = 0.12%C, 8.90%Cr, 1.09%Mo, 0.70%Si, 0.49%Mn, 0.17%Ni, 0.14%Cu, balance Fe R=0.50 freq.=20Hz env.=25°C air GS= 25μm
En 52 (100)	Composition = 0.42%C, 3.4%Si, 0.50%Mn, 8.15%Cr, 0.47%Ni, 0.03%V, balance Fe R=0.50 freq.=10Hz env.=25°C air GS= *

composition given in weight percent, * indicates data not given in reference

Fig. 5.7 Comparison of fatigue crack growth in FAP-Y and B2 ordered FA-129 with iron-base structural alloys.

6 CONCLUSIONS

The major conclusions of this work are:

1. Iron-aluminum alloys are susceptible to moisture-induced hydrogen embrittlement, and the susceptibility is increased as aluminum concentration is increased.

   a) H_2O-bearing air has no effect on the tensile RA of an Fe-16%Al alloy, but has a great effect on an Fe-28%Al alloy.

2. Effects of available time are significant in the embrittlement of iron-aluminides as evidenced by the following:

   a) Low aluminum alloys which would otherwise not be affected by moist air in monotonic tension are embrittled during fatigue crack growth.

   b) The degree of embrittlement in fatigue crack growth of B2 ordered FA-129 is greatly influenced by frequency, with growth rates increasing as frequency decreases.

3. Dislocation-assisted diffusion is responsible for transport of hydrogen atoms into the bulk of the material for B2 ordered FA-129, and this process is the rate limiting step in hydrogen embrittlement during fatigue crack growth.

4. The crack growth rate of B2 ordered FA-129 can be expressed as a superposition of purely mechanical fatigue and a corrosion-fatigue interaction term, as proposed by McEvily and Wei (48).

a) The term $(da/dN)_{cf}$ contains a stress intensity dependence and frequency dependence, which takes the form : $\left(\frac{da}{dN}\right)_{cf} = A\,\Delta K^m\, r^n$.

b) This model can be used to develop a frequency modified equation describing crack growth rate in an embrittling environment, which can be used to predict the effect of frequency on degree of embrittlement.

5. The most significant hydrogen-metal interaction in iron aluminides is decohesion along cleavage planes. Environmentally induced intergranular failure also is possible, but is not a significant contributor to embrittlement of Fe_3Al.

6. Hydrogen and H_2O vapor affect crack growth rates in both the near-threshold and near-critical regions. This behavior has been observed in a number of ordered alloys and high strength steels, but is rarely seen in other materials which exhibit the effects of embrittlement primarily at low stress intensities

   a) A possible explanation for this effect in the ordered iron aluminides is that embrittlement is dependent on dislocation-assisted hydrogen transport and the limiting velocity for hydrogen-carrying dislocations is independent of the applied stress once a maximum dislocation velocity is reached. This reasoning presumes that at any stress intensity applied during the FCG tests of this work, the velocities of hydrogen-carrying dislocations are limited by dragging effects, and not the stress intensity.

Additional conclusions are as follows:

7. The disordered alloy FAP-Y exhibits inferior FCG resistance in both inert and embrittling environments compared to the ordered, high aluminum FA-129 and Fe-35Al.

   a) The low ΔK_{TH} may be due to the disordered structure which allows for easier dislocation nucleation.

   b) Poor FCG resistance may also be due to the appearance of Zr and Cr rich precipitates in the microstructure of alloy FAP-Y which may provide paths for rapidly propagating sharp cracks.

Suggested Future Work

- Examine frequency effects on iron aluminides of different composition and order
- Use dislocation transport model to predict a critical strain rate for embrittlement in monotonic tensile tests, and compare to test data.
- Confirm that crack growth occurs continuously

7 REFERENCES

1. R. J. Lynch, L. A. Heldt and W. W. Milligan, Scripta Metall., vol. 25, pp. 2147-2151 (1991).

2. W. R. Kerr, Met. Trans. A, vol. 17A, pp. 2298-2300 (1986).

3. Lynch and Heldt, Intrinsic and Extrinsic Effects on the Ductility of B2 Ordered Iron-Aluminides, in Processing, Properties, and Applications of Iron Aluminides (TMS, Warrendale PA, 1994), pp. 287-300

4. G. M. Camus, N. S. Stoloff and D. J. Duquette, Acta Metall., vol. 37, pp. 1497-1501 (1989).

5. R. E. Ricker and D. J. Duquette, Met. Trans. A, vol. 19A, pp. 1775-1783 (1988).

6. A. K. Kuruvilla, Ph.D. Thesis, Rensselaer Polytechnic Institute (1985).

7. Y. Liu, T. Takasugi, O. Izumi and T. Yamada, Acta Metall., vol. 37, pp. 507-517 (1989).

8. T. Takasugi and O. Izumi, Scripta Metall., vol. 19, pp. 903-907 (1985).

9. T. Takasugi and O. Izumi, Acta Metall., vol. 34, pp. 607-618 (1986).

10. X. J. Wan, J. H. Zhu and K. L. Jing, Scripta Metall., vol. 26, pp. 473-477 (1992).

11. X. J. Wan, J. H. Zhu and K. L. Jing, Scripta Metall., vol. 26, pp. 479-484 (1992).

12. A. K. Kuruvilla and N. S. Stoloff, Scripta Metall., vol. 19, pp. 83-87 (1985).

13. E. P. George, C. T. Liu and D. P. Pope, Scripta Metall., vol. 30, pp. 37-42 (1994).

14. M. Masahashi, T. Takasugi and O. Izumi, Met. Trans. A, vol. 19A, pp. 353-358 (1988).

15. A. K. Kuruvilla and N. S. Stoloff, Met. Trans. A, vol. 16A, pp. 815-820 (1985).

16. C. G. McKamey and C. T. Liu, Scripta Metall., vol. 24, pp. 2119-2122 (1990).

17. C. T. Liu, E. H. Lee and C. G. McKamey, Scripta Metall., vol. 23, pp. 875-880 (1989).

18. C. T. Liu, C. G. McKamey and E. H. Lee, Scripta Metall., vol. 24, pp. 385-390 (1990).

19. M. Shea, A. Castagna and N. S. Stoloff, Hydrogen Embrittlement of FeAl and Fe_3Al, L. A. Johnson, D. P. Pope, J. O. Stiegler, Eds., High Temperature Ordered Intermetallic Alloys IV (MRS Symp. Proc., Pittsburgh PA, 1991), vol. 213, pp. 609-613.

20. E. Manor and D. Eliezer, Scripta Metall., vol. 24, pp. 129-134 (1990).

21. J. Gayda, T. P. Gabb and R. L. Dreshfield, The Effect of Hydrogen on the Low Cycle Fatigue Behavior of a Single Crystal Superalloy, N. R. Moody, A. W. Thompson, Eds., Hydrogen Effects on Material Behavior (TMS, Warrendale PA, 1990), pp. 591-599.

22. P. D. Hicks and C. J. Altstetter, Hydrogen Embrittlement of Superalloys, N. R. Moody, A. W. Thompson, Eds., Hydrogen Effects on Material Behavior (TMS, Warrendale PA, 1990), pp. 613-623.

23. N. R. Moody, M. W. Perra and S. L. Robinson, Hydrogen-Induced Cracking in an Iron-Based Superalloy, N. R. Moody, A. W. Thompson, Eds., Hydrogen Effects on Material Behavior (TMS, Warrendale PA, 1990), pp. 625-635.

24. R. G. Gest and A. R. Troiano, Corrosion, vol. 30, pp. 274-279 (1974).

25. V. M. Polyanskii, Sov. Mater. Sci., vol. 21, pp. 301-309 (1985).

26. E. R. De Los Rios, Z. Y. Sun and K. J. Miller, Fatigue Fract. Eng. Mater. Struct., vol. 16, pp. 1299-1308 (1993).

27. T. Boniszewski and G. C. Smith, Acta Metall., vol. 11, pp. 165-178 (1963).

28. D. P. DeLuca and B. A. Cowles, Fatigue and Fracture of Single Crystal Nickel in High Pressure Hydrogen, N. R. Moody, A. W. Thompson, Eds., Hydrogen Effects on Material Behavior (TMS, Warrendale PA, 1990), pp. 603-611.

29. H. J. Gudladt and J. Petit, Scripta Metall., vol. 25, pp. 2507-2512 (1991).

30. G. L. Hanna, A. R. Troiano and E. A. Steigerwald, Trans. ASM, vol. 57, pp. 658-671 (1964).

31. P. J. Cotterill and J. E. King, Int. J. Fatigue, vol. 13, pp. 447-452 (1991).

32. J. D. Landes and R. P. Wei, J. Eng. Mater. Tech., vol. 93, pp. 2-9 (1973).

33. R. D. McCright, Ph.D. Thesis, Ohio State university (1971).

34. D. B. Kasul and L. A. Heldt, Scripta Metall., vol. 25, pp. 1047-1051 (1991).

35. R. J. Lynch, W. W. Milligan and L. A. Heldt, Effects of Environment on the Ductility of Iron Aluminides, S. M. Bruemmer, E. I. Meletis, R. H. Jones, W. W. Gerberich, F. P. Ford, R. W. Staehle, Eds., Parkins Symposium on Fundamental Aspects of Stress Corrosion Cracking (TMS, Warrendale PA, 1992), pp. 117-130.

36. B. A. Graville, R. G. Baker and F. Watkinson, Brit. Weld. J., vol. 14, pp. 337-342 (1967).

37. G. Camus, D. J. Duquette and N. S. Stoloff, J. Mater. Res., vol. 5B, pp. 950 (1990).

38. G. S. Ansell and R. M. Vennet, Hydrogen Embrittlement, Contract Report # AT (30-1)-3479 (1968).

39. P. S. Pao, S. J. Gill, C. R. Feng and D. J. Michel, Mat. Sci. Eng., vol. A153, pp. 532-537 (1992).

40. J. G. Morlet, H. Johnson and A. R. Troiano, J. Iron and Steel Inst., vol. 189, pp. 37-44 (1958).

41. H. A. Wriedt and R. A. Oriani, Acta Metall., vol. 18, pp. 753-760 (1970).

42. G. E. Dieter, Mechanical Metallurgy. (McGraw-Hill, New York, 1986).

43. C. Zapfe and C. Simms, Trans. AIME, vol. 145, pp. 225 (1941).

44. H. K. Birnbaum, Mechanisms of Hydrogen related Fracture of Metals, N. R. Moody, A. W. Thompson, Eds., Hydrogen Effects on Material Behavior (TMS, Warrendale, PA, 1990), pp. 639-658.

45. H. H. Uhlig and R. W. Revie, Corrosion and Corrosion Control. (John Wiley and Sons, New york, 1985).

46. T. J. Marrow, C. A. Hippsley and J. E. King, Acta Metall., vol. 39, pp. 1367-1376 (1991).

47. J. J. Scott, M.S. Thesis, Rensselaer Polytechnic Institute (1992).

48. A. J. McEvily and R. P. Wei, Fracture Mechanics and Corrosion Fatigue, O. F. Devereux, A. J. McEvily, R. W. Staehle, Eds., Corrosion-Fatigue: Chemistry, Mechanics, and Microstructure (NACE, Houston, 1972), vol. NACE-2, pp. 381-395.

49. R. P. Wei, Eng. Fract. Mech., vol. 1, pp. 633-657 (1970).

50. R. P. Wei, Int. J. of Fract., vol. 4, pp. 159-170 (1968).

51. C. T. Simms, N. S. Stoloff and W. C. Hagel, Superalloys II. (John Wiley & Sons, Inc., New York, 1987).

52. N. S. Stoloff and R. G. Davies, Acta Metall., vol. 12, pp. 473-485 (1964).

53. G. W. Ardley, Acta Metall., vol. 3, pp. 525 (1955).

54. Y. Hayashi, N. Iwai and N. Ohtani, Z. Physik, Chemie Neue Folge, vol. 114, pp. 213-220 (1979).

55. H. J. Leamy and F. X. Kayser, Phys. Stat. Sol., vol. 34, pp. 765-780 (1969).

56. J. W. Park, I. G. Moon and J. Yu, Advanced Structural Materials, vol. , pp. 797-801 (1991).

57. H. Inouye, Effects of DO_3 Transitions on the Yield Behavior of Fe-Al Alloys, C. C. Koch, C. T. Liu, N. S. Stoloff, Eds., High Temperature Ordered Intermetallic Alloys (MRS, Pittsburgh PA, 1985), vol. 39, pp. 255-261.

58. M. G. Mendiratta, S. K. Ehlers, D. K. Chatterjee and H. A. Lipsitt, Met. Trans. A, vol. 18A, pp. 283-291 (1987).

59. C. G. McKamey, J. H. DeVan, P. F. Tortorelli and V. K. Sikka, J. Mater. Res., vol. 6, pp. 1779-1805 (1991).

60. N. S. Stoloff, M. Shea and A. Castagna, Hydrogen Embrittlement of Intermetallic Compounds and Their Composites, R. H. Jones, R. E. Ricker, Eds., Environmental Effects on Advanced Materials (TMS, Warrendale, PA, 1991), pp. 3-19.

61. C. G. McKamey, J. A. Horton and C. T. Liu, J. Mater. Res., vol. 4, pp. 1156-1162 (1989).

62. T. B. Massalski, Binary Alloy Phase Diagrams. (ASM, Metals Park, OH, 1986).

63. H. Inouye, Effects of DO3 Transitions on the Yield behavior of Fe-Al Alloys, C. C. Koch, C. T. Liu, N. S. Stoloff, Eds., High Temperature Ordered Intermetallic Alloys (MRS, Pittsburgh, PA, 1985), vol. 39, pp. 255-261.

64. D. B. Kasul and L. A. Heldt, Met. Trans. A, vol. 25A, pp. 1285-1290 (1994).

65. G. G. Hancock and H. H. Johnson, Trans. AIME, vol. 236, pp. 513-516 (1966).

66. R. J. Lynch, K. A. Gee and L. A. Heldt, Scripta Metall., vol. 30, pp. 945-950 (1994).

67. C. G. McKamey and E. H. Lee, Measurement of the Critical Level of Moisture for Initiation of Water-Vapor-Induced Environmental Embrittlemet in an Fe_3Al-Based Alloy, I. Baker, R. Darolia, J. D. Whittenberger, M. H. Yoo, Eds., High Temperature Ordered Intermetallic Alloys V (MRS, Pittsburgh PA, 1993), vol. 288, pp. 983-988.

68. J. G. Kim and R. A. Buchanan, Localized Corrosion and Stress Corrosion Cracking Characteristics of Low-Aluminum Content Iron-Aluminum Alloys, Proc. 8th Annual Conference on Fossil Energy Materials (US Department of Energy, Fossil Energy Program, Oak Ridge, TN, 1994), pp. 321-330.

69. Physical Metallurgy and Processing of Intermetallic Compounds. N. S. Stoloff, V. K. Sikka, Eds., (Chapman and Hall, Inc., 1995 (in press)).

70. R. J. Lynch and L. A. Heldt, Intrinsic and Extrinsic Effects on the Ductility of B2-Ordered Iron Aluminides, J. H. Schneibel, M. A. Crimp, Eds., Processing, Properties, and Applications of Iron Aluminides (TMS, Warrendale, PA, 1994), pp. 287-300.

71. C. G. McKamey, J. A. Horton and C. T. Liu, Scripta Metall., vol. 22, pp. 1679-1681 (1988).

72. C. T. Liu, C. L. White and J. A. Horton, Acta Metall., vol. 33, pp. 213-229 (1985).

73. C. T. Liu and E. P. George, Effect of Aluminum Concentration and Boron Dopant on Environmental Embrittlement in FeAl Aluminides, L. A. Johnson, D. P. Pope, J. O. Stiegler, Eds., High Temperature Ordered Intermetallic Alloys IV (MRS, Pittsburgh PA, 1991), vol. 213, pp. 527-532.

74. C. T. Liu and E. P. George, Scripta Metall., vol. 24, pp. 1285-1290 (1990).

75. D. J. Gaydosh and M. V. Nathal, Scripta Metall., vol. 24, pp. 1281-1284 (1990).

76. J. A. Horton, C. T. Liu and C. C. Koch, Alloying Effects and Microstructure of Iron-Aluminides, J. O. Stiegler, Ed., High Temperature Alloys: Theory and Design (TMS/AIME, Warrendale PA, 1984), pp. 309-321.

77. D. B. Kasul and L. A. Heldt, Environmetnal Effects on the Mechanical Properties of an Fe-24.6Al Alloy, (TMS/ASM, 1990),

78. C. G. McKamey and D. H. Pierce, Scripta Metall., vol. 28, pp. 1173-1176 (1993).

79. M. G. Mendiratta, S. K. Ehlers, D. M. Dimiduk, W. R. Kerr, S. Mazdiyasni and H. A. Lipsitt, A Review of Recent Developments in Iron Aluminides, N. S. Stoloff, C. C. Koch, C. T. Liu, O. Izumi, Eds., High Temperature Ordered Intermetallic Alloys II (MRS, Pittsburgh PA, 1987), vol. 81, pp. 393-404.

80. R. S. Diehm and D. E. Mikkola, Effects of Mo and Ti Additions on the high Temperature Compressive Properties of Iron Aluminides Near Fe_3Al, N. S. Stoloff, C. C. Koch, C. T. Liu, O. Izumi, Eds., High Temperature Ordered Intermetallic Alloys II (MRS, Pittsburgh PA, 1987), vol. 81, pp. 329-334.

81. C. G. McKamey, P. J. Maziasz and J. W. Jones, J. Mater. Res., vol. 7, pp. 2089-2106 (1992).

82. A. J. McEvily and R. C. Boettner, Acta Metall., vol. 11, pp. 725-743 (1963).
83. B. H. Kear, Acta Metall., vol. 12, pp. 555-569 (1964).

84. R. C. Boettner, N. S. Stoloff and R. G. Davies, Trans. AIME, vol. 236, pp. 131-133 (1966).

85. ASTM, in Annual Book of ASTM Standards: Section 3(ASTM, Philadelphia, 1987).

86. V. K. Sikka, . (Oak Ridge National Laboratory, Oak Ridge TN, 1994),

87. C. D. Beachem, in Fracture - An Advanced Treatise H. Liebowitz, Ed. (Academic Press, New York, 1968), vol. 1 - Microscopic and Macroscopic Fundamentals, pp. 597.

88. G. R. Irwin, Eng. Fract. Mech., vol. 1, pp. 241-257 (1968).

89. R. Brazill, G. W. Simmons and R. P. Wei, J. Eng. Mater. Tech., vol. 101, pp. 199-204 (1979).

90. P. Lukas, L. Kunz and J. Bartos, Mat. Sci. Eng., vol. 56, pp. 11-18 (1982).

91. R. P. Wei and G. W. Simmons, Int. J. of Fract., vol. 17, pp. 235-247 (1981).

92. J. K. Tien and R. J. Richards, Scripta Metall., vol. 9, pp. 1097-1101 (1975).

93. J. K. Tien, A. W. Thompson, I. M. Bernstein and R. J. Richards, Metall. Trans. A, vol. 7A, pp. 821-829 (1976).

94. J. Albrecht, I. M. Bernstein and A. W. Thompson, Met. Trans. A, vol. 13A, pp. 811-820 (1982).

95. M. R. Louthan, G. R. Caskey, J. A. Donovan and D. E. Rawl, Mat. Sci. Eng., vol. 10, pp. 357 (1972).

96. S. P. Lynch, A Comparative Study of Stress-Corrosion Cracking, Hydrogen Assisted Cracking and Liquid-Metal Embrittlement in Al, Ni, Ti and Fe-Based Alloys, I. M. Bernstein, A. W. Thompson, Eds., Hydrogen Effects in Metals (TMS, Warrendale PA, 1981), pp. 863-871.

97. J. Masounave and J. P. Baolon, Scripta Metall., vol. 10, pp. 165-170 (1976).

98. H. J. Roven and E. Nes, Acta Metall., vol. 39, pp. 1735-1754 (1991).

99. P. J. Cotterill and J. F. Knott, Acta Metall., vol. 40, pp. 2753-2764 (1992).

100. M. G. Hebsur, K. P. Abraham and Y. V. R. K. Prasad, Int. J. Fatigue, vol. 2, pp. 147-152 (1980).

101. G. Henaff, J. Petit and B. Bouchet, Int. J. Fatigue, vol. 14, pp. 211-218 (1992).

102. W. O. Soboyejo and J. F. Knott, Int. J. Fatigue, vol. 12, pp. 403-407 (1990).

103. K. T. V. Rao and R. O. Ritchie, Mater. Sci. Eng., vol. A153, pp. 479-485 (1992).

APPENDIX A - Survey of Literature on Ductility and Embrittlement of Iron Aluminides

Alloy	Order	Grain Size (μm)	Environment*	YS (MPa)	Ductility (%)	Fractrue Surface	Strain Rate $(sec)^{-1}$	Reference
Fe-22Al	B2	-	Air	-	2.1	TG	0.00033	(1)
Fe-22Al	B2	-	Vac, $<3x10^{-3}$Pa	-	2.5	TG	0.00033	(1)
Fe-22Al	B2	-	O_2	-	2.1	TG	0.00033	(1)
Fe-24.6Al	B2	unRX	Air	685	4.0	TG	0.00033	(3)
Fe-24.6Al-worked	B2	unRX	Air	696	6.4	TG	0.00033	(3)
Fe-24.6Al	B2	110	Air	-	4.0	TG	0.00033	(34)
Fe-24.6Al	B2	110	Air	-	4.0	TG	0.00033	(34)
Fe-24.6Al	B2	330	Air	592	2.0	TG	0.00033	(3)
Fe-24.6Al	B2	1420	Air	588	2.1	TG	0.00033	(3)
Fe-24.6Al	B2	110	Vac, $<3x10^{-3}$Pa	-	6.1	TG	0.00033	(34)
Fe-24.6Al	B2	unRX	O_2, 0.118MPA	682	9.3	TG	0.00033	(3)
Fe-24.6Al-worked	B2	unRX	O_2,0.118MPa	671	9.0	TG	0.00033	(3)
Fe-24.6Al	B2	unRX	O_2, 0.118MPA	682	9.3	TG	0.00033	(3)
Fe24.6Al worked	B2	unRX	O_2,0.118MPa	671	9.0	TG	0.00033	(3)
Fe-24.6Al	B2	110	O_2, 0.115MPa	-	6.1	-	0.00033	(34)
Fe-24.6Al	B2	330	O_2, 0.118MPa	636	6.1	TG	0.00033	(3)
Fe-24.6Al	B2	1420	O_2, 0.118MPa	569	3.1	TG	0.00033	(3)
Fe-26Al	B2	-	O_2	-	2.3	TG	0.00033	(1)
Fe-27.5Al	B2	-	Air	-	1.0	TG	0.00033	(1)
Fe-27.5Al	B2	-	Vac, $<3x10^{-3}$Pa	-	1.8	TG	0.00033	(1)
Fe-27.5Al	B2	-	O2	-	2.8	TG	0.00033	(1)
Fe-28Al	DO_3	-	H_2O	322	2.1	TG	-	(18)
Fe-28Al	DO_3	-	Ar+4% H_2	-	-	-	-	(18)
Fe-28Al	DO_3	-	Air	279	3.7	TG		(18)
Fe-28Al	DO_3	118	Air	279	3.7	TG	0.33	(61)
Fe-28Al	DO_3	-	Vac	316	12.4	TG	-	(18)

Alloy	Order	Grain Size (μm)	Environment*	YS (MPa)	Ductility (%)	Fractrue Surface	Strain Rate $(sec)^{-1}$	Reference
Fe-28Al	DO_3	-	O_2	298	11.7	TG	-	(18)
Fe-28Al	B2	-	H_2O	387	2.1	TG	-	(18)
Fe-28Al	B2	-	Ar+4% H_2	385	8.4	TG	-	(18)
Fe-28Al	B2	-	Air	387	4.0	TG	-	(18)
Fe-28Al	B2	-	Vac	387	12.8	TG	-	(1)
Fe-28Al	B2	-	Vac, $<3x10^{-3}$Pa	-	4.0	TG	0.00033	(1)
Fe-28Al	B2	-	O_2	392	12.0	TG	-	(18)
Fe-28Al	B2	-	O_2	-	6.0	TG	0.00033	(1)
Fe-30Al	B2	-	Air	-	1.3	TG	0.00033	(1)
Fe-30Al	B2	-	O_2	-	10.0	TG	0.00033	(1)
Fe-33Al	-	-	Air, 30% RH **	-	2.3	-	-	(35)
Fe-33Al	-	-	Air, 9% RH	-	3.0	-	-	(35)
Fe-33Al	B2	-	Air	-	1.5	TG+IG	0.00033	(1)
Fe-33Al	B2	-	10 vpm H_2O in O_2	-	9.0	TG+IG	0.00033	(3)
Fe-33Al	B2	-	100 vpm H_2O in O_2	-	6.0	TG+IG	0.00033	(3)
Fe-33Al	B2	-	10^4 vpm H_2O in O_2	-	2.0	TG+IG	0.00033	(3)
Fe-33Al	-	-	Vac	-	7.2	-	-	(35)
Fe-33Al	B2	-	Vac, $<3x10^{-3}$Pa	-	6.5	TG+IG	0.00033	(1)
Fe-33Al	-	-	O_2	-	9.3	-	-	(35)
Fe-33Al	B2	-	O_2	-	9.0	TG+IG	0.00033	(1)
Fe-35Al	B2	SX	Air (49°)	247	4.5	TG	0.00033	(3)
Fe-35Al	B2	SX	O_2 (40°)	230	22.7	TG	0.00033	(3)
Fe-35Al	B2	SX	Air (19°)	242	3.9	TG	0.00033	(3)

Alloy	Order	Grain Size (μm)	Environment*	YS (MPa)	Ductility (%)	Fractrue Surface	Strain Rate $(sec)^{-1}$	Reference
Fe-35Al	B2	SX	O_2 (19°)	232	18.5	TG	0.00033	(3)
Fe-35Al	B2	-	Air	347	3.4	TG	-	(3)
Fe-35Al	B2	-	Vac, $1x10^{-4}$Pa	341	7.3	TG	-	(73)
Fe-35Al	B2	-	O_2, 0.1MPa	345	18.1	TG+IG	-	(73)
Fe-35.5Al	B2	-	Air	-	2.5	TG+IG	0.00033	(1)
Fe-35.5Al	B2	-	Vac, $<3x10^{-3}$Pa	-	7.5	TG+IG	0.00033	(1)
Fe-35.5Al	B2	-	O_2	-	11.0	TG+IG	0.00033	(1)
Fe-36Al	B2	335	Air	243	3.1	-	0.00033	(3)
Fe-36Al	B2	335	O_2, 0.118MPa	243	13.2	-	0.00033	(3)
Fe-36.5Al	B2	-	H_20, 67Pa	368	2.4	TG	0.33	(17)
Fe-36.5Al	B2	-	H_2+Ar, 110Pa	378	6.1	TG	0.33	(17)
Fe-36.5Al	B2	-	H_2+Ar, 1670Pa	375	5.5	TG	0.33	(17)
Fe-36.5Al	B2	-	Air	360	2.2	TG	0.33	(17)
Fe-36.5Al	B2	-	Vac, $<10^{-4}$Pa	352	5.4	TG+IG	0.33	(17)
Fe-36.5Al	B2	-	O_2	373	11.3	IG	0.33	(17)
Fe-36.5Al	B2	-	O_2, 0.07MPa	360	17.6	IG		(74)
Fe-38Al	B2	-	Air	-	0.5	IG	0.00033	(1)
Fe-38Al	B2	-	O_2	-	2.0	IG	0.00033	(1)
Fe-40Al P/M	-	24	Air	-	0.8	-	-	(75)
Fe-40Al+.5B,P/M	-	24	Air	-	2.8	-	-	(75)
Fe-40Al	-	200	Air	390	1.2	IG	-	(74)
Fe-40Al+.12%B	-	200	Air	391	4.3	TG	-	(75)
Fe-40Al,P/M	-	24	Vac	-	5.0	-	-	(75)
Fe-40Al+.5B,P/M	-	24	Vac	-	8.0	-	-	(75)

Alloy	Order	Grain Size (μm)	Environment*	YS (MPa)	Ductility (%)	Fractrue Surface	Strain Rate $(sec)^{-1}$	Reference
Fe-40Al	-	200	O_2, 0.07MPa	402	3.2	IG	-	(74)
Fe-40Al+.12%B	--	200	O_2, 0.07MPa	392	16.8	TG	-	(74)
Fe-28Al+2Cr	DO_3	105	Air	274	9.4	TG+IG	0.33	(61)
Fe-28Al+4Cr	DO_3	112	Air	228	8.2	TG+IG	0.33	(61)
Fe-28Al-5Cr	DO_3	-	Air, 550°C Anneal	550	5.4	TG	0.0033	(78)
Fe-28Al-5Cr+ 0.1Zr+0.05B	DO_3	-	Air, 650°C Anneal	543	8.1	TG	0.0033	(78)
Fe-28Al-5Cr+ 0.1Zr+0.05B	DO_3	-	Air, 750°C Anneal	479	8	TG	0.0033	(78)
Fe-28Al-5Cr+ 0.1Zr+0.05B	DO_3	-	Air, 850°C Anneal	453	6.4	TG	0.0033	(78)
Fe-35Al-2Cr	B2	-	21vpm H2O in Ar	-	3.2	-	0.00033	(3)
Fe-35Al-2Cr	B2	-	220vpm H2O in Ar	-	1.8	-	0.00033	(3)
Fe-35Al-2Cr	B2	-	245vpm H2O in O_2	-	5.2	-	0.00033	(3)

* All tests were conducted at room temperature

** RH = Relative Humidity

APPENDIX B - Additional Data

Stress-Strain Curves

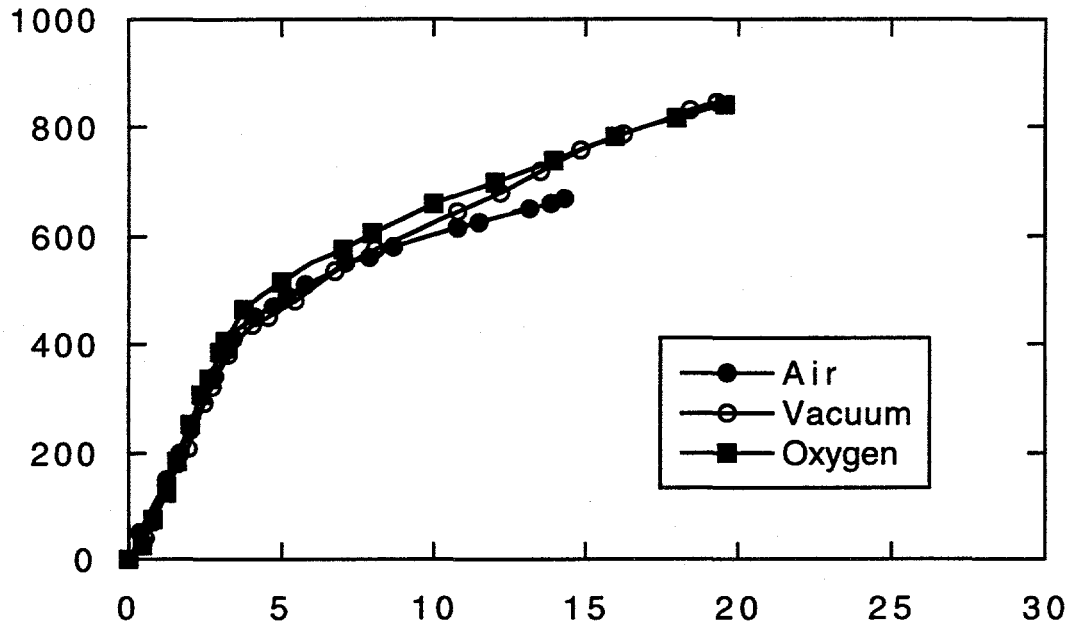

(a)

Fig. B1. Stress-strain curves for B2 ordered FA-129 at 25°C, strain rate = 3.3×10^{-4}/sec, data sets (a) and (b).

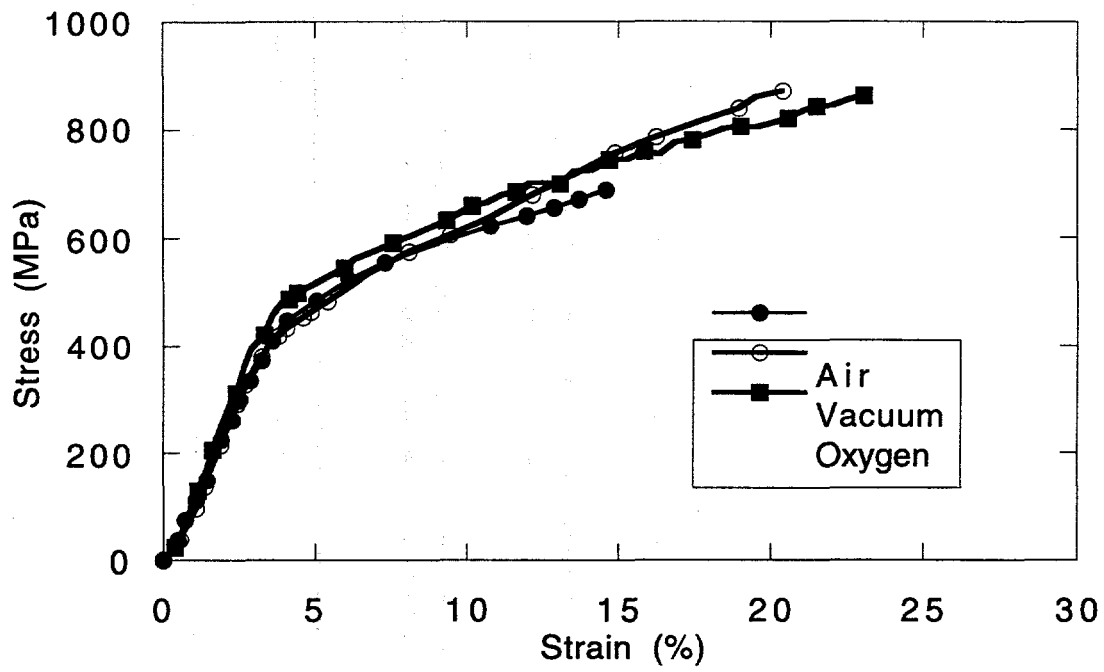

(b)

Fig. B1. (continued) Stress-strain curves for B2 ordered FA-129 at 25°C, strain rate = 3.3×10^{-4}/sec, data sets (a) and (b).

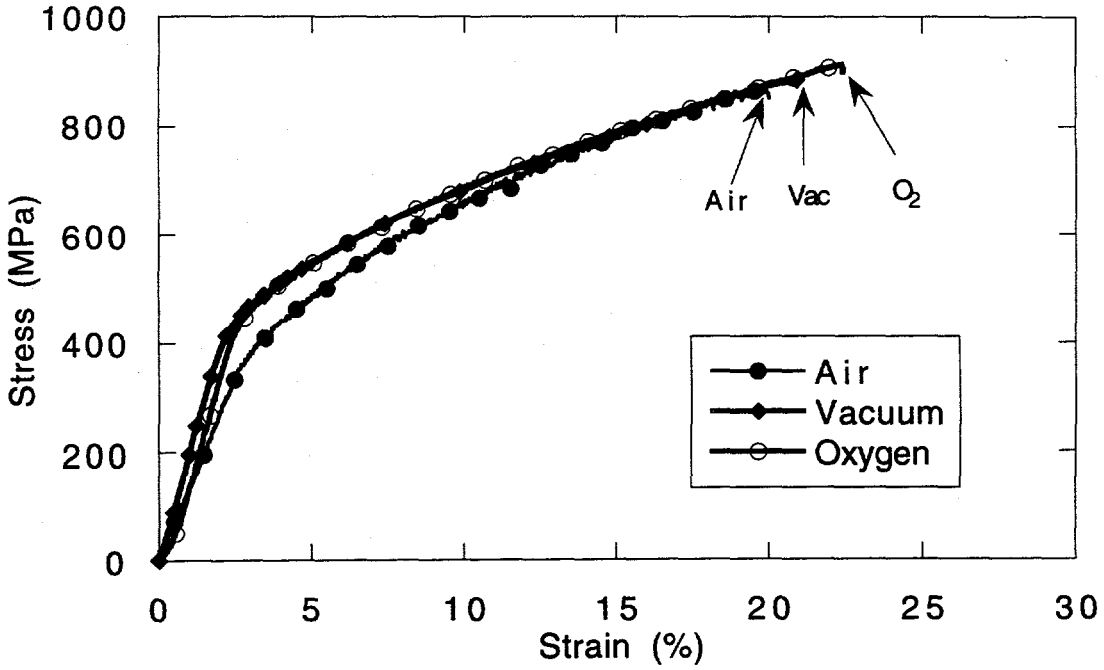

(a)

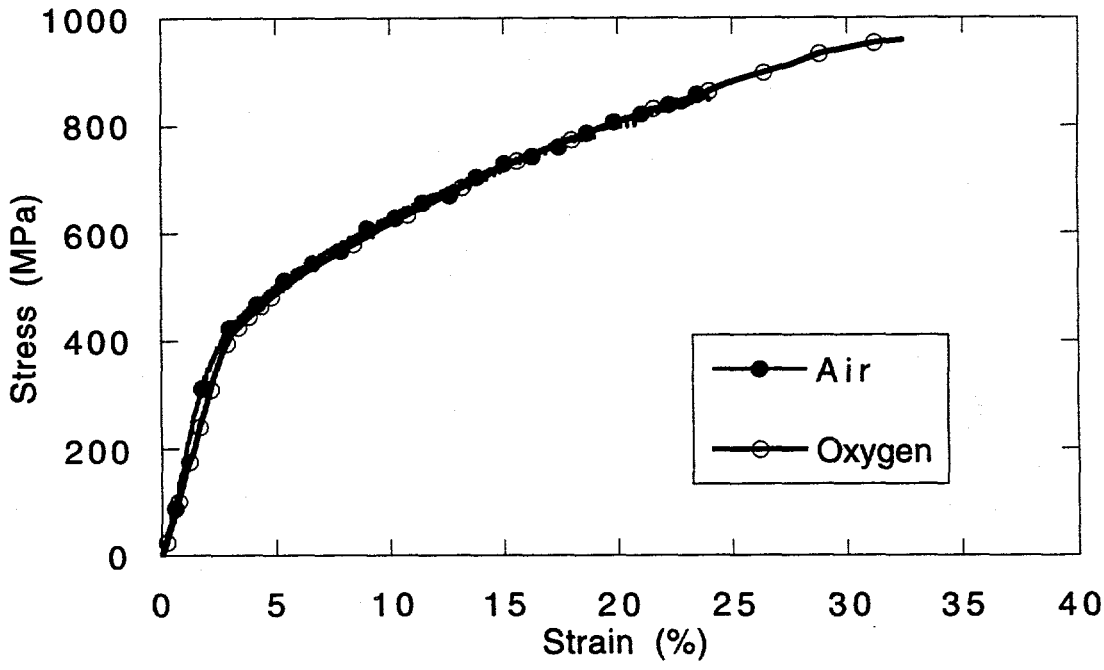

(b)

Fig. B2. Stress-strain curves for B2 ordered FA-129 at 150°C, strain rate = 3.3×10^{-4}/sec, data sets (a) and (b).

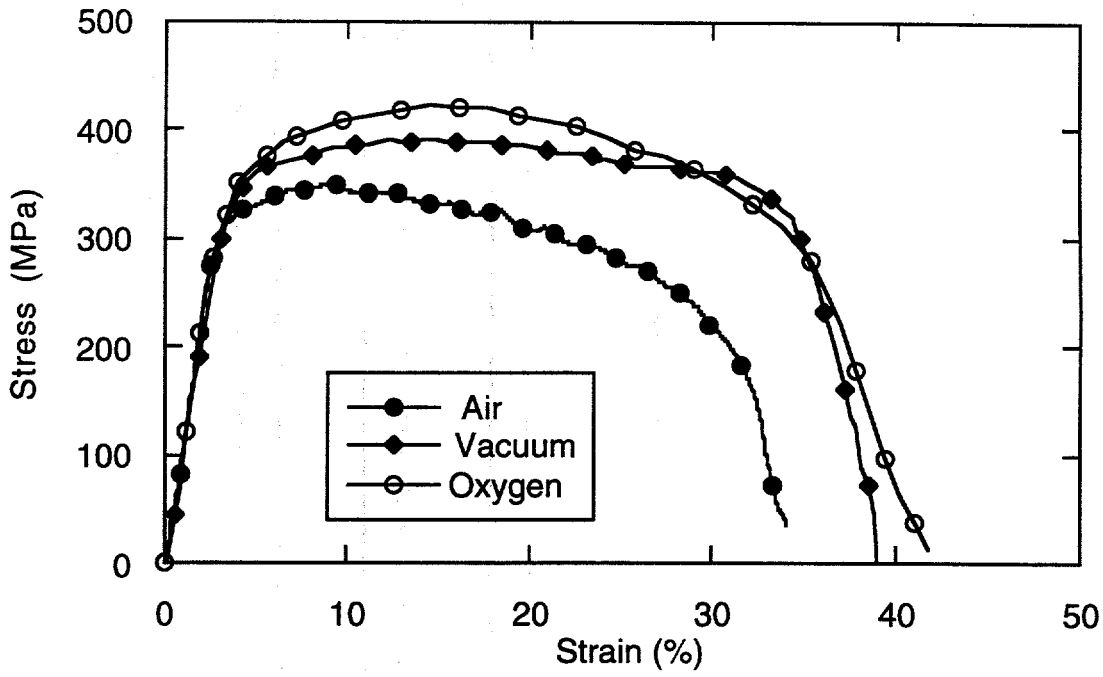

(a)

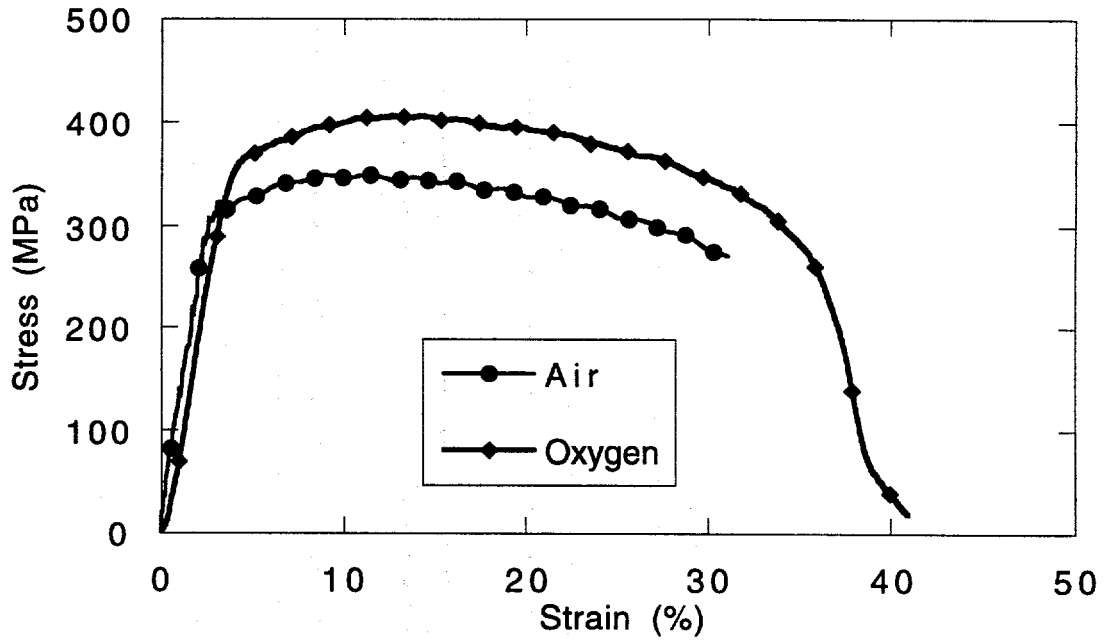

(b)

Fig. B3. Stress-strain curves for B2 ordered FA-129 at 600°C, strain rate = 3.3×10^{-4}/sec, data sets (a) and (b).

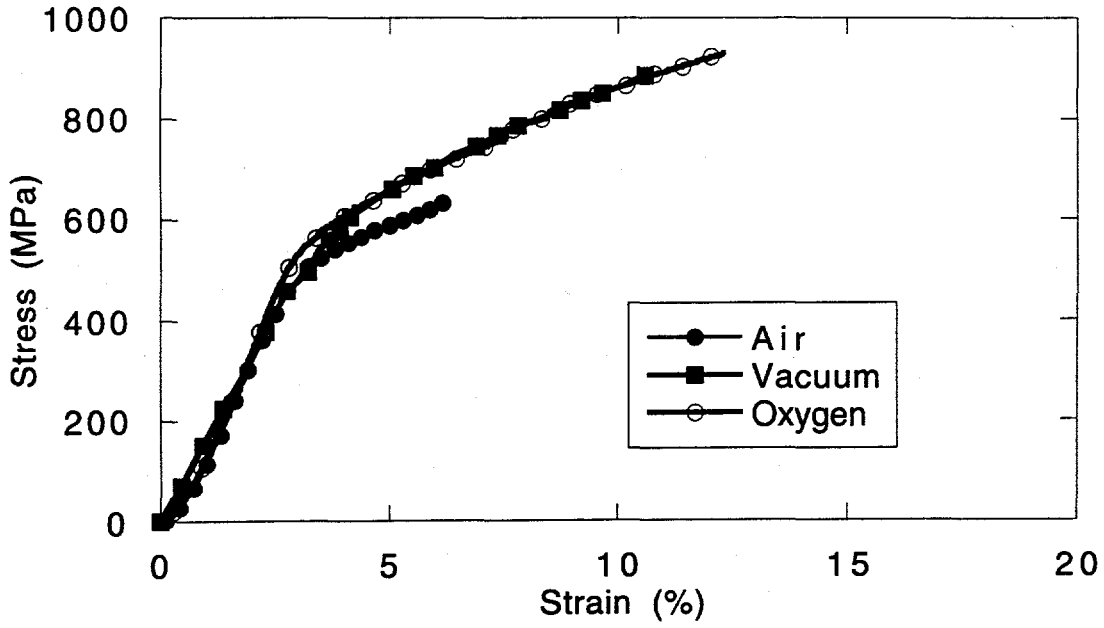

(a)

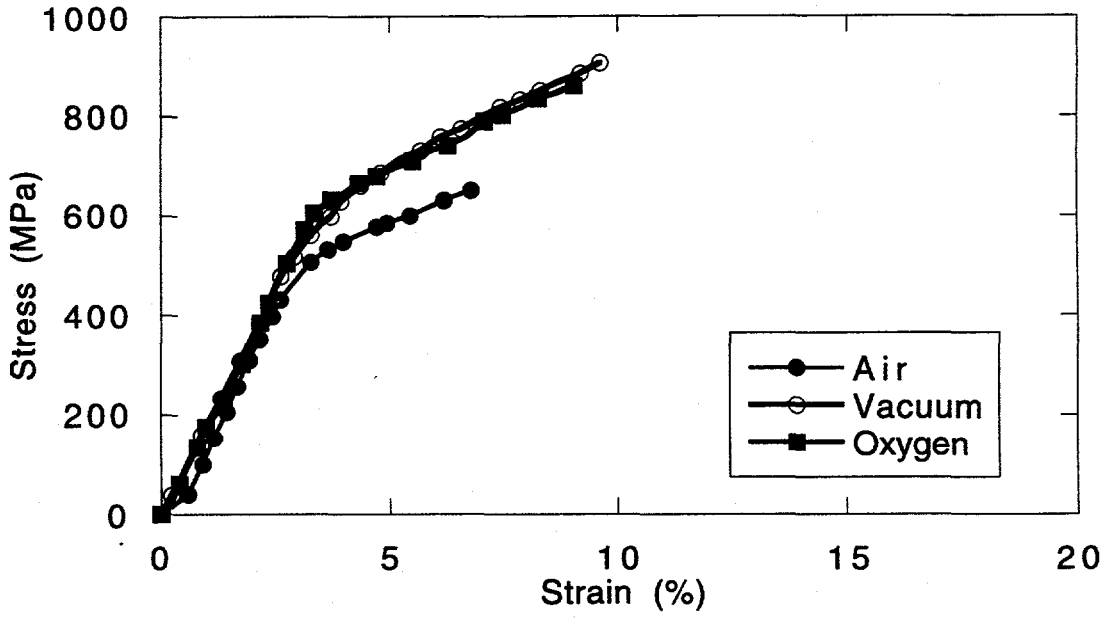

(b)

Fig. B4. Stress-strain curves for DO_3 ordered FA-129 at 25°C, strain rate = 3.3×10^{-4}/sec, data sets (a) and (b).

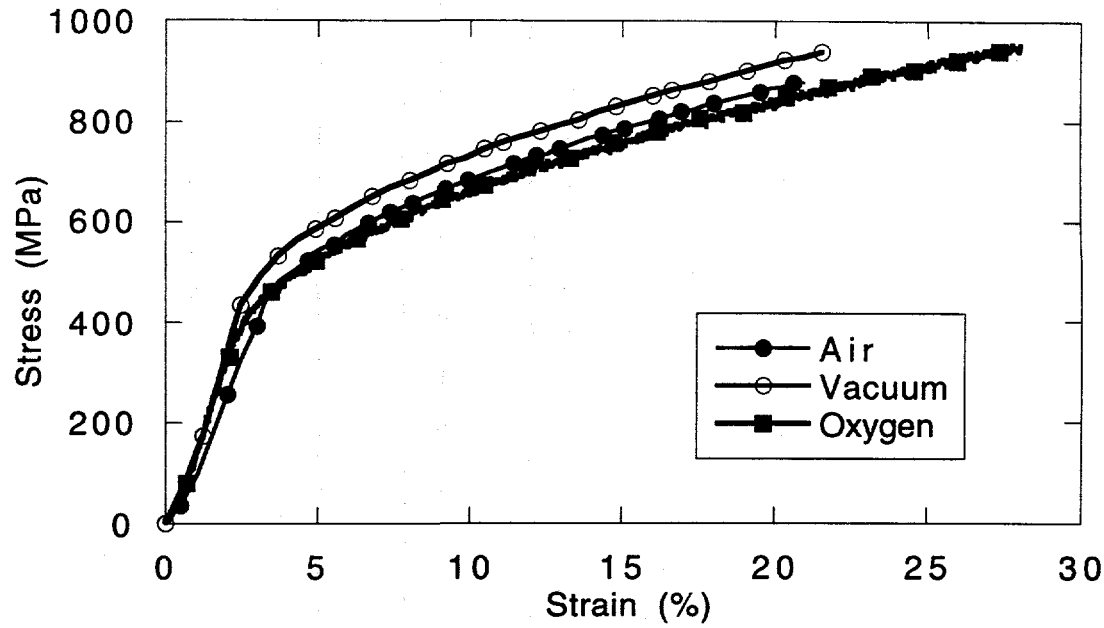

(a)

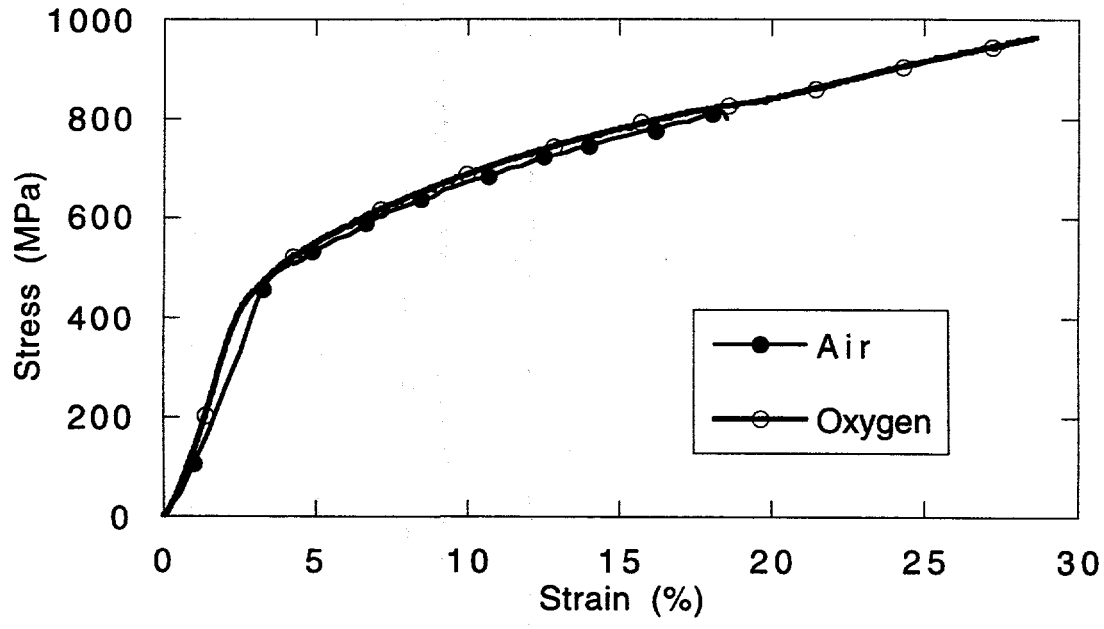

(b)

Fig. B5. Stress-strain curves for DO_3 ordered FA-129 at 150°C, strain rate = 3.3×10^{-4}/sec, data sets (a) and (b).

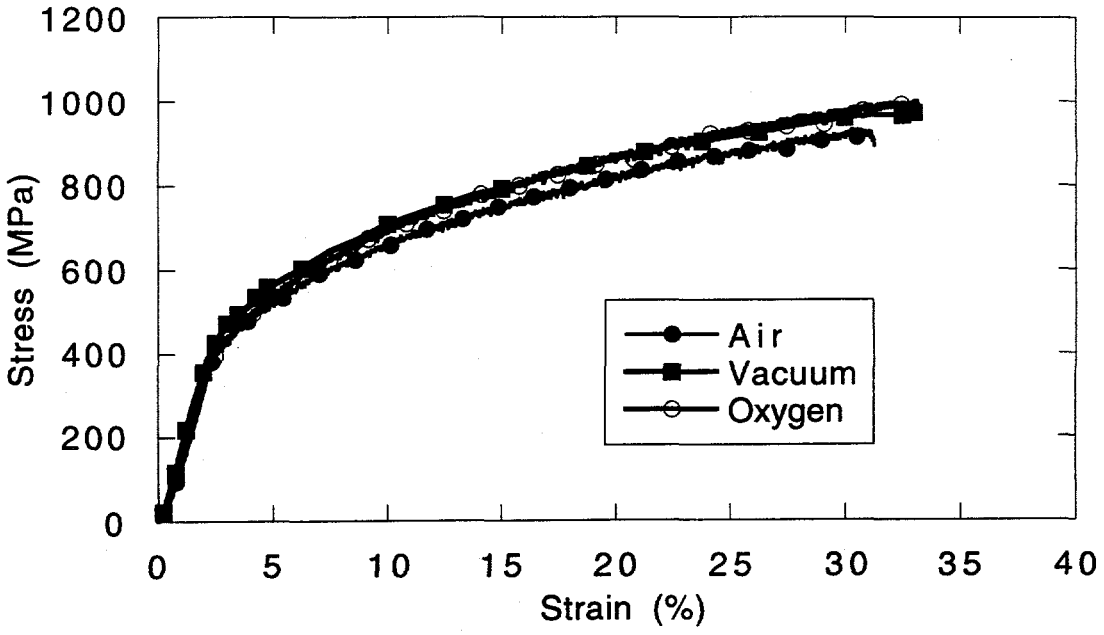

(a)

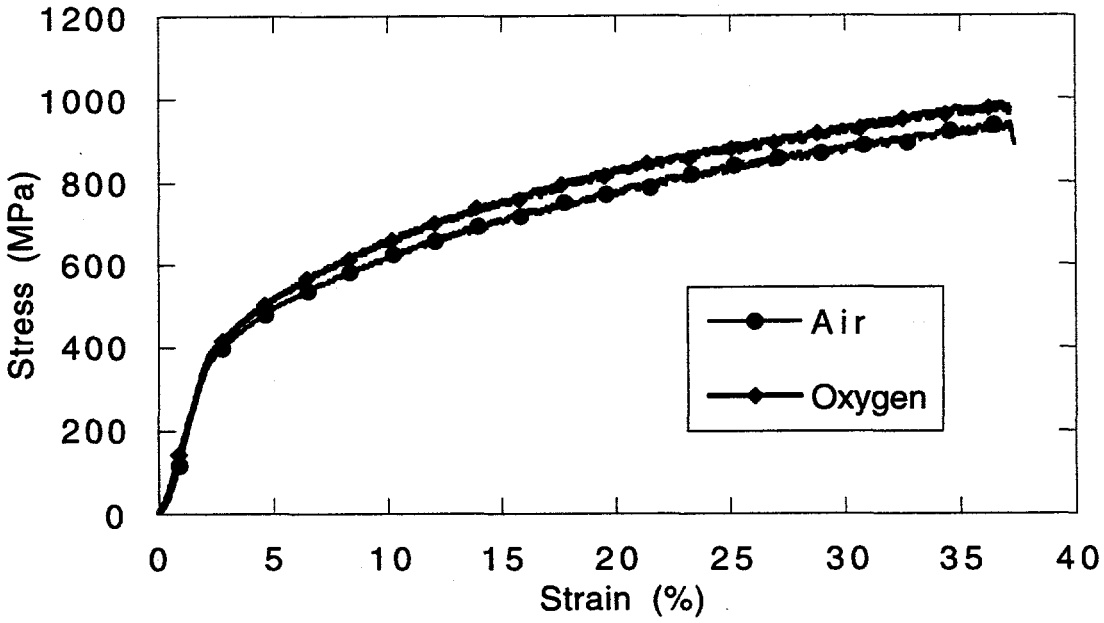

(b)

Fig. B6. Stress-strain curves for DO_3 ordered FA-129 at 300°C, strain rate = 3.3×10^{-4}/sec, data sets (a) and (b).

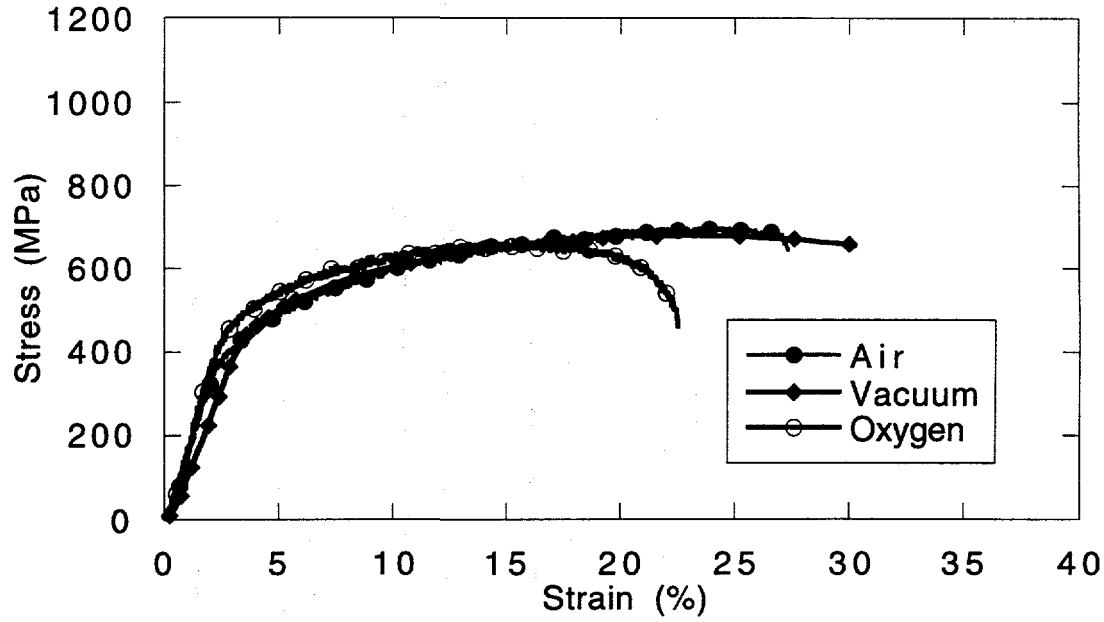

(a)

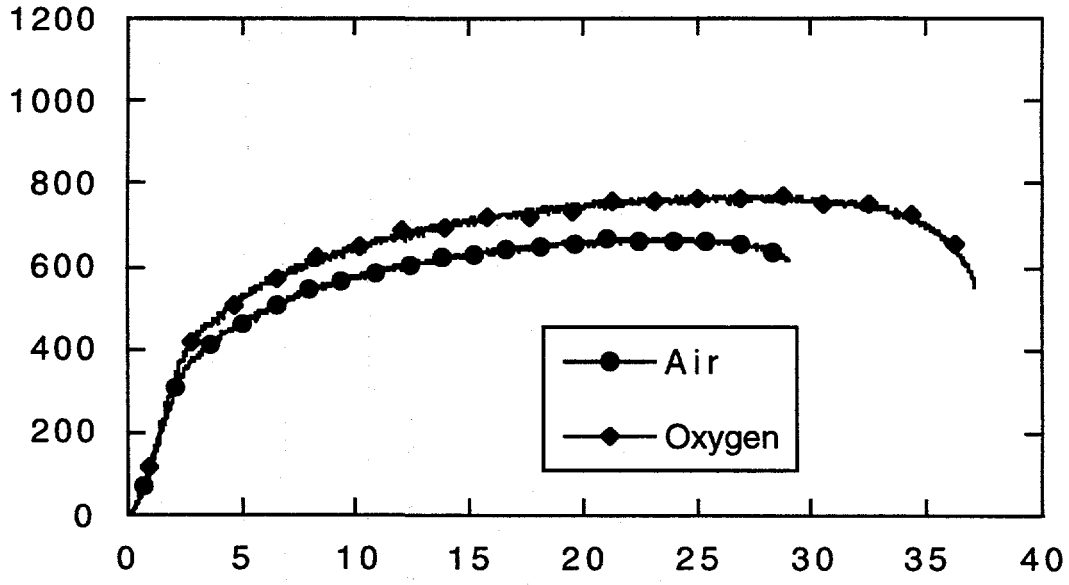

(b)

Fig. B7. Stress-strain curves for DO_3 ordered FA-129 at 450°C, strain rate = 3.3×10^{-4}/sec, data sets (a) and (b).

Liquid Metal Embrittlement

The tensile properties of B2 ordered FA-129 tested in oxygen with and without mercury are shown in Fig. B1. The ductility and UTS are severely reduced by exposure to mercury. Ductility decreases from 9.0% without mercury to 1.6% with mercury, and the UTS is decreased from 694 MPa to 459 MPa. In mercury, as in hydrogen gas, the YS is not significantly affected by embrittlement.

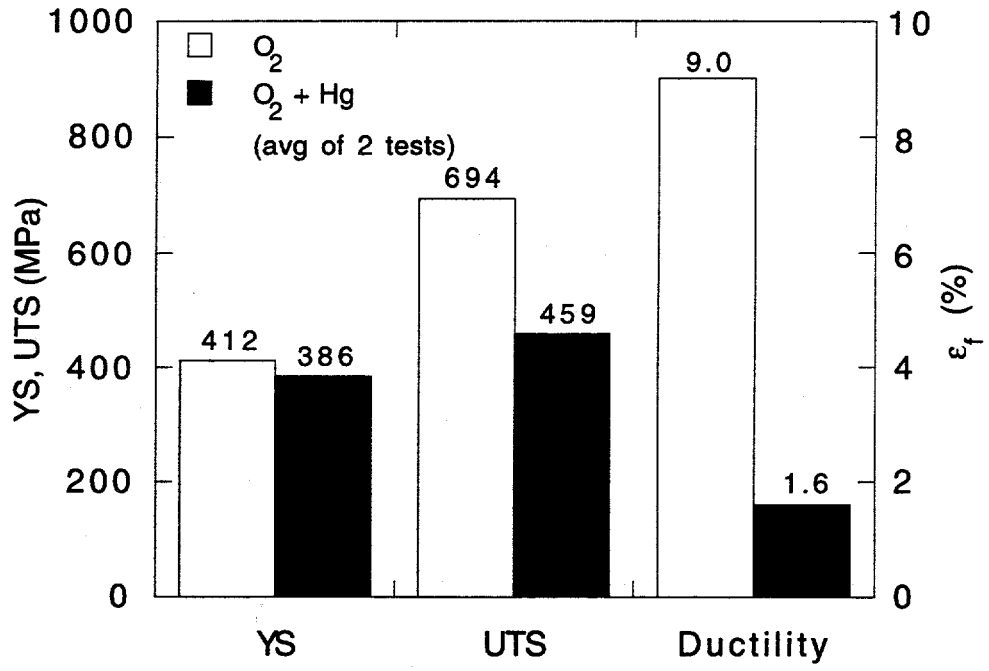

Fig. B8 Summary of mercury embrittlement tensile data for FA-129 at 25°C.

Additional Alloy Comparisons

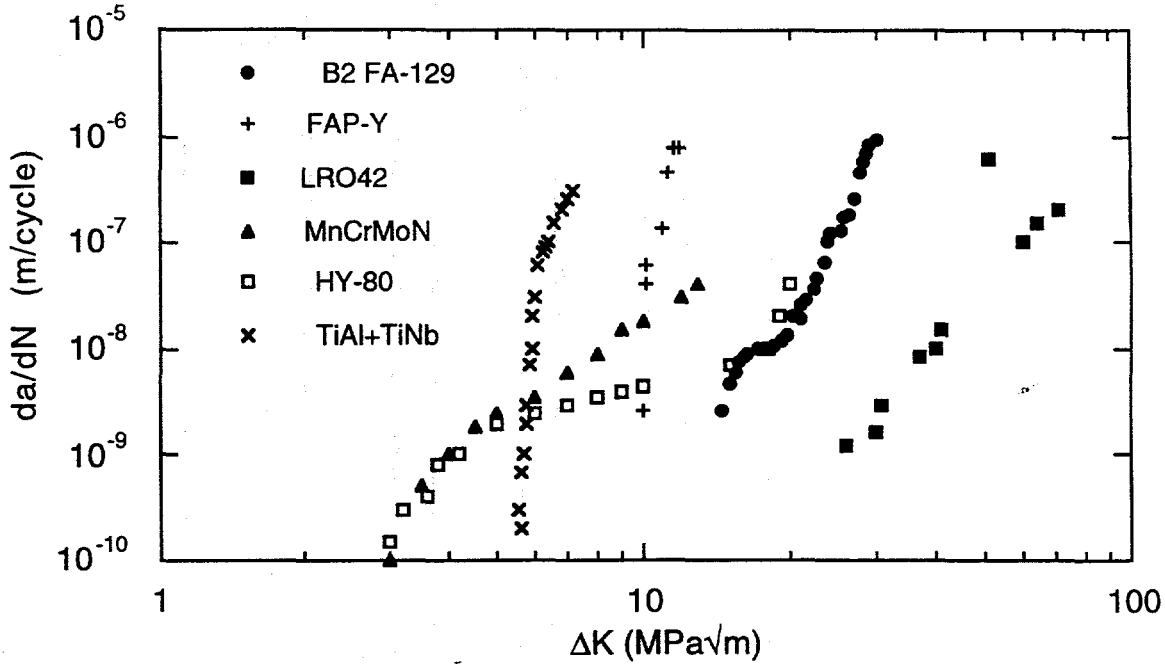

LRO42: Composition = 39.5%Ni, 37%Fe, 22.4%V, 0.4%Ti
(6) R=0.17 freq.=20Hz env.=25°C air GS=30μm

MnCrMoN: Composition = 0.3%C, 0.36%Si, 0.45%Mn, 3.4%N,
(101) 1.3w%Cr, 0.4w%Mo, bal Fe
R=0.70 freq.=35Hz env.=25°C air GS= *

HY-80 Composition = 2.5%Ni, 1.5%Cr, 0.5%Mo, 0.18%C, bal Fe
(102) R=0.50 freq.=40Hz env.=25°C air GS= *

TiAl + Composition = 50a%Ti, 50a%Al + 5vol% Ti-33Nb
TiNb R=0.1 freq.=50Hz env.=25°C air GS= 50μm
(103)

composition in w% unless otherwise noted
* indicates data not given in reference

Fig. B9 Comparison of fatigue crack growth in FAP-Y and B2 ordered FA-129 with iron-base structural alloys.

DISTRIBUTION

AIR PRODUCTS AND CHEMICALS
P.O. Box 538
Allentown, PA 18105
S. W. Dean

ALBERTA RESEARCH COUNCIL
Oil Sands Research Department
P.O. Box 8330, Postal Station F
Edmonton, Alberta
Canada T6H5X2
L. G. S. Gray

ALLISON GAS TURBINE DIVISION
P.O. Box 420
Indianapolis, IN 46206-0420
P. Khandelwal (Speed Code W-5)
R. A. Wenglarz (Speed Code W-16)

AMAX R&D CENTER
5950 McIntyre Street
Golden, CO 80403
T. B. Cox

ARGONNE NATIONAL LABORATORY
9700 S. Cass Avenue
Argonne, IL 60439
W. A. Ellingson
K. Natesan

ARGONNE NATIONAL
LABORATORY-WEST
P.O. Box 2528
Idaho Falls, ID 83403-2528
S. P. Henslee

AVCO RESEARCH LABORATORY
2385 Revere Beach Parkway
Everett, MA 02149
R. J. Pollina

BABCOCK & WILCOX
1562 Beeson St.
Alliance, OH 44601
T. I. Johnson

BABCOCK & WILCOX
Domestic Fossil Operations
20 South Van Buren Avenue
Barberton, OH 44023
M. Gold

BETHLEHEM STEEL CORPORATION
Homer Research Laboratory
Bethlehem, PA 18016
B. L. Bramfitt
J. M. Chilton

BRITISH COAL CORPORATION
Coal Research Establishment
Stoke Orchard, Cheltenham
Gloucestershire, England GL52 4RZ
J. Oakey

CANADA CENTER FOR MINERAL &
ENERGY TECHNOLOGY
568 Booth Street
Ottawa, Ontario
Canada K1A OG1
R. Winston Revie
Mahi Sahoo

COLORADO SCHOOL OF MINES
Department of Metallurgical Engineering
Golden, CO 80401
G. R. Edwards

DOE
DOE OAK RIDGE OPERATIONS
P. O. Box 2008
Building 4500N, MS 6269
Oak Ridge, TN 37831
E. E. Hoffman

DOE
DOE OAK RIDGE OPERATIONS
P. O. Box 2001
Oak Ridge, TN 37831
Assistant Manager for
Energy Research and Development

DOE
IDAHO OPERATIONS OFFICE
P. O. Box 1625
Idaho Falls, ID 83415
R. B. Loop

DOE
MORGANTOWN ENERGY TECHNOLOGY CENTER
P.O. Box 880
Morgantown, WV 26505
R. C. Bedick
D. C. Cicero
F. W. Crouse, Jr.
N. T. Holcombe
W. J. Huber
J. E. Notestein

DOE
OFFICE OF FOSSIL ENERGY
FE-72
19901 Germantown Road
Germantown, MD 20874-1290
J. P. Carr

DOE
OFFICE OF BASIC ENERGY SCIENCES
Materials Sciences Division
ER-131 GTN
Washington, DC 20545
J. B. Darby

DOE
OFFICE OF SCIENTIFIC AND TECHNICAL INFORMATION
P. O. Box 62
Oak Ridge, TN 37831
For distribution by microfiche as shown in DOE/TIC-4500, Distribution Category: UC-114 (Coal Based Materials and Components)

DOE
PITTSBURGH ENERGY TECHNOLOGY CENTER
P.O. Box 10940
Pittsburgh, PA 15236
A. L. Baldwin
G. V. McGurl
R. Santore
T. M. Torkos

EC TECHNOLOGIES INC.
3614 Highpoint Drive
San Antonio, TX 78217
D. J. Kenton

ELECTRIC POWER RESEARCH INSTITUTE
P.O. Box 10412
3412 Hillview Avenue
Palo Alto, CA 94303
W. T. Bakker
J. Stringer
H. Wolk

EUROPEAN COMMUNITIES JOINT RESEARCH CENTRE
Petten Establishment
P.O. Box 2
1755 ZG Petten
The Netherlands
M. Van de Voorde

FOSTER WHEELER DEVELOPMENT CORPORATION
Materials Technology Department
John Blizard Research Center
12 Peach Tree Hill Road
Livingston, NJ 07039
J. L. Blough

IDAHO NATIONAL ENGINEERING LABORATORY
P.O. Box 1625
Idaho Falls, ID 83415
A. B. Denison
R. N. Wright

LAWRENCE LIVERMORE LABORATORY
P.O. Box 808, L-325
Livermore, CA 94550
W. A. Steele

NATIONAL MATERIALS ADVISORY BOARD
National Research Council
2101 Constitution Avenue
Washington, DC 20418
K. M. Zwilsky

NEW ENERGY AND INDUSTRIAL TECHNOLOGY DEVELOPMENT ORGANIZATION
Sunshine 60 Bldg.
P.O. Box 1151, 1-1
Higashi-Ikebukuro 3-chrome
Toshima-Ku, Tokyo, 170
Japan
H. Narita
S. Ueda

OAK RIDGE NATIONAL LABORATORY
P.O. Box 2008
Oak Ridge, TN 37831
P. T. Carlson
N. C. Cole
R. R. Judkins
C. T. Liu
R. A. Lawson **(8 copies)**
C. G. McKamey
V. K. Sikka
R. W. Swindeman
P. T. Thornton
I. G. Wright

PACIFIC NORTHWEST LABORATORY
P. O. Box 999, K3-59
Battelle Boulevard
Richland, WA 99352
R. N. Johnson

RESEARCH TRIANGLE INSTITUTE
P.O. Box 12194
Research Triangle Park, NC 27709
T. W. Sigmon

SHELL DEVELOPMENT COMPANY
P. O. Box 1380
Houston, TX 77251-1380
L. W. R. Dicks

THE JOHNS HOPKINS UNIVERSITY
Materials Science & Engineering
Maryland Hall
Baltimore, MD 21218
R. E. Green, Jr.

THE MATERIALS PROPERTIES COUNCIL, INC.
United Engineering Center
345 E. Forty-Seventh Street
New York, NY 10017
M. Prager

THE TORRINGTON COMPANY
Advanced Technology Center
59 Field Street
Torrington, CT 06790
W. J. Chmura

UNION CARBIDE CORPORATION
Linde Division
P.O. Box 44
175 East Park Drive
Tonawanda, NY 14151-0044
Harry Cheung

UNIVERSITY OF WASHINGTON
Department of Materials Science
and Engineering
101 Wilson, FB-10
Seattle, WA 98195
T. G. Stoebe

UNIVERSITY OF TENNESSEE SPACE
INSTITUTE
Tullahoma, TN 37388
J. W. Muehlhauser

UNIVERSITY OF TENNESSEE AT
KNOXVILLE
Materials Science and Engineering
Department
Knoxville, TN 37996
P. Liaw
C. D. Lundin

WESTERN RESEARCH INSTITUTE
365 N. 9th Street
P.O. Box 3395
University Station
Laramie, WY 82071
V. K. Sethi

WESTINGHOUSE ELECTRIC
CORPORATION
Research and Development Center
1310 Beulah Road
Pittsburgh, PA 15235
S. C. Singhal